This is to certify that the
dissertation entitled

JOSEPHSON JUNCTIONS USING A STRONG FERROMAGNETIC INTERLAYER AND SPIN TRIPLET SUPERCONDUCTIVITY

presented by

MAZIN ALAYA KHASAWNEH

has been accepted towards fulfillment
of the requirements for the

Ph.D degree in PHYSICS

Norman O. Birge

Major Professor's Signature

12/3/2010

Date

DATE DUE	DATE DUE	DATE DUE

JOSEPHSON JUNCTIONS USING A STRONG FERROMAGNETIC INTERLAYER AND SPIN TRIPLET SUPERCONDUCTIVITY

By

Mazin Alaya Khasawneh

A DISSERTATION

Submitted to
Michigan State University
in partial fulfillment of the requirements
for the degree of

DOCTOR OF PHILOSOPHY

Physics

2010

ABSTRACT

JOSEPHSON JUNCTIONS USING A STRONG FERROMAGNETIC INTERLAYER AND SPIN TRIPLET SUPERCONDUCTIVITY

By

Mazin Alaya Khasawneh

Superconductivity and ferromagnetism are two competing phenomena: a superconductor expels a magnetic field, which in turn tries to weaken the superconductivity. However, the coexistence of conventional spin singlet (two electrons of opposite spin) superconductivity, and ferromagnetism (electron spins are aligned parallel) may be achieved by fabricating superconductor/ferromagnet (S/F) hybrid structures. The interplay between conventional superconductivity and magnetism in S/F systems leads to a fast decay of the order parameter in the F-layer as the two electrons from the spin-singlet Cooper pair enter different spin bands and rapidly lose phase coherence. It has been predicted that spin triplet pair correlations can be created near the S/F interface in the presence of certain kinds of magnetic inhomogeneity. If the spin triplet correlations are present at the SF interface, then the spin triplet proximity effect persists over much longer distances in the ferromagnet. These correlations exhibit a new type of symmetry: they are odd in frequency or time. The essence of this project was a systematic approach to observe these correlations in Co-based Josephson junctions. Since our early data didn't show any sign of long-range spin triplet correlations, we decided to split the observation process into two stages: generation and propagation. Generation of spin triplet correlations at the SF interface is provided by a thin layer of $Cu_{0.48}Ni_{0.52}$ alloy placed next to the Nb electrodes. For the propagation, we used a Synthetic Antiferromagnet, SAF configuration consisting of Co(x)/Ru(0.6 nm)/Co(x) as thick as $2x = 39$ nm. We observed a large enhancement in the supercurrent compared to junctions without the CuNi alloy. These experimental observations provide strong evidence for the long triplet nature of these correlations.

DEDICATION

To my parents, my wife and kids and my brothers and sisters.

ACKNOWLEDGMENT

First and foremost, I thank Allah the Almighty. It was Allah's help and guidance that enlightened the way for me during these years at Michigan State University. As our beloved prophet Mohammad peace and blessing from Allah be upon him said: He (She) who doesn't thank people who do him (her) a favor, doesn't thank Allah. So it is a duty upon me to thank my thesis adviser, Professor Norman O. Birge for his professional guidance, criticism and support during the years of this project. Norman, your kindness and patience will never be forgotten. I would like also to thank you for your financial support. I also would like to thank Professor William P. Pratt Jr. for his great ideas and valuable discussions. Also his experimental abilities are extraordinary, which I respect and appreciate very much. Also, I would like to thank my other committee members, professors Banu Mahanti, Wayne Repko, and Bernard Pope, for honoring me by being committee members.

Very special thanks go to Dr. Reza Loloee, the man behind any success in the Condensed Matter Group. What is remarkable about Reza is his willingness to help with always a smile on his face, no matter how my questions sometimes look stupid. Also his down-to-earth character deserves respect. Another man behind the curtain is Dr. Baoking Bi, the manager of the cleanroom facility, who also deserves a big thank you.

A very heartly thank you goes to all my family members: my beloved father and mother, whom their continuous praying and support gave me the ability to finish this work, my brothers and sisters, also thank you very much.

Now a very special thank to the woman I share my life with, my lovely wife Manar Abu-Qamer. You were with me step by step in this journey, and I think without you, I wouldn't be where I am now. Your patience, support and optimism helped me a lot to overcome many of the difficulties I faced, so thank you very much. I would like also to thank my lovely kids, Leen and Mohammad for making my life more enjoyable. I

would like also to thank my in-laws for their support.

Next I would like to thank our graduate secretary Debbie Barratt and CMP secretary Cathy Cords for their kindness and help. Also I would like to the thank Tom Palazzolo and Jim Muns from the machine shop for helping me to learn the basics of machining and for the nice discussions we had over different subjects. My friends in the group also deserve thank you as well. Trupti Khaire, Yixing Wang who wrote a Labview program that helped me analyze my Fraunhoffer patterns, Eric Gingrich, William Martinez and Kurt Boden.

Finally, I would like to thank my bigger family here in East Lansing: the brothers and sisters of the Islamic Society of Greater lansing. The years I spent with you shaped my life to the end, thank you very much.

TABLE OF CONTENTS

LIST OF TABLES

LIST OF FIGURES

Chapter 1

Preface

This chapter presents a road map to the thesis so that the reader can have some basic idea(s) about what this project is about. It gives some key aspects of both superconductivity and ferromagnetism, and their interplay as well as the motivation behind this study.

1.1 Brief introduction

Superconductivity and ferromagnetism are two antagonistic phenomena as they have competing order parameters. The exchange interaction in ferromagnets results in aligning the spins of the electrons in one direction, while conventional superconductivity prefers a spin-antiparallel alignment (Spin-singlet) through the formation of Cooper pairs. The coexistence of superconductivity and ferromagnetism in bulk materials is very unlikely, but the interplay between them in artificially layered structures leads to a very rich and interesting physics through the proximity effect. Superconductivity (S) and ferromagnetism (F) can interact and influence each other in the vicinity of the interface. This is called the proximity effect, where Cooper pairs may leak from the S-side to the F(N)-side of the SF(N) structure. In the case of SN

structures, the pair correlations decay in the normal metal over the length scale ξ_N known as the normal metal coherence length, which could be as large as 1 μ m. If the normal metal is replaced by a ferromagnet, then it is a different story. Since the two electrons making the Cooper pair enter two different spin bands, they acquire a center of mass momentum, and as a result the order parameter oscillates and decays exponentially over the length scale ξ_F known as the ferromagnetic metal coherence length that depends on the exchange energy of the ferromagnet. ξ_F could be a few nm if a weak ferromagnet is used, but it is very small ($\sim$ 1nm) if a strong ferromagnet is used.

1.2 Motivation

A few years ago, it was predicted that the proximity effect in a ferromagnet can survive over much longer distances, of order the normal metal coherence length ξ_N, if the superconducting order parameter has triplet (S=1) symmetry rather than the traditional BCS singlet (S=0). This is because the two electrons enter the same spin band when they leak into the ferromagnet. What is remarkable is that spin-triplet pairs can appear even if we use a conventional spin-singlet superconductor (s-wave) with the total spin $S = 1$. But there is a pre-condition, which is, there should be some sort of magnetic inhomogeneity at the SF interface. This new type of symmetry is known as Long Range Triplet Correlation (LRTC). Our approach to observe this new type of symmetry was to fabricate SFS Josephson junctions with the thickness of the ferromagnetic layer (d_F) systematically increased. Then we measure the Josephson critical current I_c, and plot it vs. d_F. At small thicknesses I_c oscillates and decays rapidly over the short length scale $\xi_F^{Singlet}$. At large values of d_F and in the presence of magnetic inhomogeneity, the LRTC takes over and Ic decays over a much longer length scale $\xi_F^{Triplet} \approx \xi_N$.

1.3 Thesis structure

The thesis is organized as follows: In chapter 2, I give an introduction to the main aspects of superconductivity and ferromagnetism. In chapter 3, I discuss the theory of the Josephson effect. That includes Feynman's derivation of the Josephson equations, their I-V characteristics and their response to the applied magnetic field. In chapter 4, I discuss the Josephson junctions with a ferromagnetic interlayer. The proximity effect in SN and SF hybrid systems is discussed. Also a complete description of the LRTC, and the mechanisms to generate and observe it are presented. In chapter 5, I discuss the details of the sample fabrication process. In chapter 6, I present what I call the short-range correlation data. First the data of single Co layer Josephson junctions are presented. The distorted diffraction patterns led us to the use of synthetic antiferromagnets (SAF). The data for SAF with Ru and Cu are presented. Finally the theory of SFFS Josephson junctions is explained and possible explanation for the absence of LRTC is given. In chapter 7, I present the most important finding in this thesis, the observation of spin-triplet superconducting correlations in Co-based Josephson junctions of the form $SF'[SAF]F'S$, with SAF being Co/Ru/Co, and F' is the weak ferromagnetic alloy CuNi. Data for Co-platelets, and CuPt as the F' layers are also presented. Possible mechanisms for the generation of the spin-triplet correlations are presented as well. Finally in chapter 8, a conclusion and future directions are discussed.

Chapter 2

Introduction and preliminaries

In this chapter I will briefly explain both phenomena. I should say that it is not the aim of this chapter to explain all aspects of superconductivity and ferromagnetism, rather giving a brief but sufficient taste of the key aspects of both phenomena relevant to our study. For a detailed description of superconductivity, the reader is directed to some of the many excellent text books written about superconductivity [1, 2], and ferromagnetism [3, 4].

2.1 Superconductivity

A new chapter in low temperature physics was opened on July, 10, 1908. On that day, and for the first time ever, the Dutch physicist Heike Kamerlingh Onnes succeeded in liquefying helium. Three years later, in 1911, he found that the resistivity of mercury Hg, suddenly dropped to zero at 4.2 K [5], as shown in Figure 2.1. Kamerlingh Onnes nicknamed this zero resistance behavior, Superconductivity. For this discovery, and the liquefication of helium, Onnes won the 1913 Nobel prize in physics. At the early stages of superconductivity, most superconductors were elemental metals like mercury, lead, and bismuth. They become superconductors at very low tem-

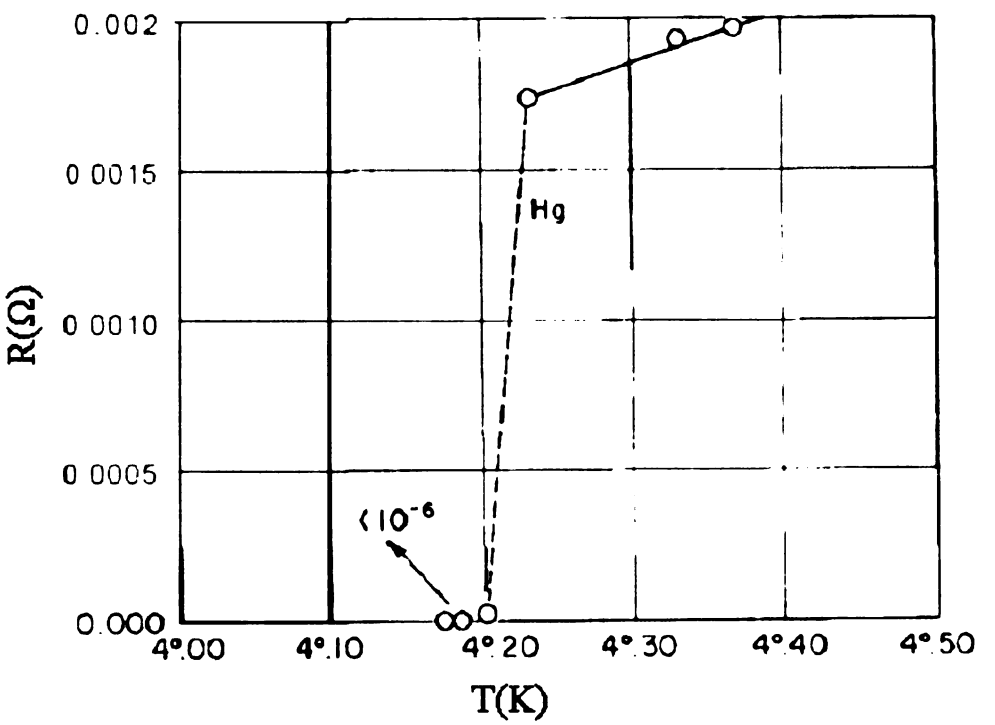

Figure 2.1: Resistance in Ohms, of a piece of Hg vs. absolute temperature. This plot by Onnes marked the birth of superconductivity [5].

peratures. A material becomes superconducting below a characteristic temperature known as the superconducting transition temperature, T_c. Over time, various alloys were found to superconduct at somewhat higher temperatures, but the highest temperature remained at a plateau of about 23 K. Thus liquid helium was the only convenient coolant that could be used with these superconductors. The year 1986 was a revolution in superconductivity. In that year, (West) German physicist Georg Bednorz and Swiss physicist Alex Müeller, working at IBM in Zurich Switzerland, were experimenting with a particular class of metal oxide ceramics called perovskites. They surveyed hundreds of different oxide compounds. Working with ceramics of lanthanum, barium, copper, and oxygen they found indications of superconductivity at 35 K, a startling 12 K above the old record for a superconductor [6]. In February of 1987, a perovskite ceramic material was found to superconduct at 90 K. Alex Müeller, and Georg Bednorz, won the Nobel Prize in Physics in 1987 for their discovery of high-temperature superconductivity in a new class of materials. This discovery was very significant because now it became possible to use liquid nitrogen (77K) as a coolant. Because these materials superconduct at significantly higher temperatures they are referred to as High Temperature Superconductors. The following table shows the critical temperatures, Tc of various superconductors.

Material		T_c (K)
Zinc	metal	0.88
Aluminum	metal	1.19
Tin	metal	3.72
Mercury	metal	4.72
Niobium	metal	9.2
$YBa_2Cu_3O_7$	ceramic	90
TiBaCaCuO	ceramic	125

Table 2.1: Critical temperatures, Tc of various superconductors.

Another hallmark property of superconductors besides the zero electrical resistance is the Meissner effect (or should be Meissner-Oschenfeld) [7]. When the su-

perconducting material is cooled down below its transition temperature, T_c in the presence of a magnetic field, the field is completely expelled from the bulk of the superconductor. The superconductor will not allow a magnetic field to penetrate its interior. The magnetic field is screened from the interior of the superconductor by currents flowing along the surface, which means that the magnetic field is only allowed to enter the superconductor up to a characteristic length known as the London penetration depth, λ_L (section 2.3).

Since the discovery of superconductivity, many great theoretical physicists have devoted the time and effort to understand its nature. The frustration they encountered was so remarkable to the extent that Felix Bloch is said to have invented (not published) a theorem that a theory of superconductivity is impossible. But it took almost half a century to reach a microscopic theory that can explain this remarkable behavior. This theory was proposed by John Bardeen, Leon Cooper, and John Schrieffer (BCS) in 1957. In their theory they showed that the zero resistant behavior came as a result of condensation of coupled electrons into Cooper pairs. The coupling is provided by the lattice vibrations known as phonons. This correlated electron motion (the system functions as a single entity) extends over thousands of atomic lattice spacing. For their theory of superconductivity which became known as "BCS theory", Bardeen, Cooper, and Schrieffer won the 1972 Nobel Prize in physics (we will revisit the BCS theory in more detail in section 2.4).

2.2 Normal state vs. Superconducting state

In this section I will talk about the origin of the electrical resistivity in normal metals and contrast it with the zero electrical resistance in superconductors.

2.2.1 The normal state behavior

A metal in the normal state can be thought of a regular lattice of positive ions with non-interacting conduction electrons filling the space between the ions. When traveling through a perfect crystal lattice, electrons suffer no scattering. But since metals have some imperfections like missing atoms, and interstitial atoms, then electrons suffer frequent collisions with these imperfections and get scattered. Another source of electron scattering comes from the thermal vibrations of the lattice (phonons). The thermal motion of the lattice increases with temperature. Between collisions, electrons move freely for a mean free time, τ, over the characteristic length, l_e, called the electron mean free path, which is the average distance an electron moves ($l_e = v_f \tau$), where v_f is the fermi velocity. According to the Drude model, the resistivity is given by:

$$\rho = \frac{m v_f}{n e^2 l_e} \tag{2.1}$$

Equation (2.1) shows that electrical resistivity of metals is inversely proportional to the electron mean free path.

2.2.2 Early picture of the superconducting state behavior

As we said earlier, superconductivity is characterized by the disappearance of electrical resistance when the material is cooled below T_c, so how to understand this puzzling behavior? An important advance in the understanding of superconductivity occurred in 1934, when C. J. Gorter and H. B. G. Casimir [8] proposed a two fluid model to account for this new behavior. This model assumes that the electron liquid in a superconductor can be separated into two liquids: normal fluid (free electrons) of density n_n, and superfluid electrons of density n_s. The normal component is identical to that of the electron system in a normal metal, and the superfluid component is primarily responsible for the remarkable properties of superconductors. The fraction

n_s/n_n grows steadily from zero at T_c to unity at T = 0, where all of the electrons are in the superfluid condensate. The temperature dependent densities of the normal and superconducting electrons, n_n, and n_s add up to the total density of the conduction electrons,

$$n_n(T) + n_s(T) = n \tag{2.2}$$

The super current and the normal current flow in parallel, but the supercurrent carries the entire current and short circuits current arising from the flow of normal electrons, causing the measured resistance to vanish.

2.3 London Theory

In 1935, the London brothers, Fritz and Heinz, proposed a simple theory to explain the Meissner effect (discovered two years earlier). They treat the electrons as accelerating under the influence of an electric field [9]. They derived two equations, now known as the London equations. The first one reads:

$$\vec{E} = \frac{\partial(\Lambda \vec{J_c})}{\partial t} \tag{2.3}$$

and the second one reads:

$$\vec{H} = -\Lambda(\vec{\nabla} \times \vec{J_c}) \tag{2.4}$$

where

$$\Lambda = \frac{m}{n_s e^2} \tag{2.5}$$

with m and e denoting the electronic mass and charge, respectively. n_s is the number density of superconducting electrons, and J_c is the current density carried by the superelectrons. The first equation predicts the perfect conductivity and the second predicts the existence of the Meissner state. If we consider a uniform magnetic field

applied parallel to the surface of the superconductor, then the field at distance x inside the superconductor is given by:

$$H = H_0 exp(\frac{-x}{\lambda_L}) \tag{2.6}$$

where H_0 is the magnetic field at the surface of the superconductor. The magnetic field decays exponentially to zero inside the superconductor over the length scale λ_L known as the London penetration depth, which is a measure of the extent of the penetration of the magnetic field inside the superconductor and is given by:

$$\lambda_L = \sqrt{\frac{m}{\mu_0 n_s e^2}} \tag{2.7}$$

2.4 BCS theory of superconductivity

The first microscopic theory superconductivity was formulated in 1957 by John Bardeen, Leon Cooper, and Robert Schrieffer [10] based on the idea of pairing of electrons (Cooper pairs) due to an attractive potential. The nature of this interaction is as follows. An electron moving in a metal distorts the lattice by means of electric forces. The distortion of the lattice caused in this way affects the state of the other incoming electron, since the latter now finds itself in a positively charged region with somewhat altered structure. This results in an effective attractive force between the electrons. The BCS ground state of a Cooper pair is given by:

$$\Psi_{BCS} = \prod_k (u_k + v_k a^\dagger_{k,\uparrow} a^\dagger_{k,\downarrow}) |\phi_0\rangle \tag{2.8}$$

where $a^\dagger_{k,\uparrow}$ and $a^\dagger_{k,\downarrow}$ are the electron creation operators which operate on the vacuum state (state of no electrons) $|\phi_0\rangle$. The product $a^\dagger_{k,\uparrow} a^\dagger_{k,\downarrow}$ creates a Cooper pair which consists of two electrons with opposite spins and opposite wave vectors. At low tem-

peratures, in many materials, this inter-electron attraction overcomes the Coulomb repulsion between the electrons. In the BCS ground state, the electron system is treated as a single bound unit (not individual electrons), and a finite amount of energy must be spent in order to excite it. The excited state of the system is separated from the ground state by an energy gap, Δ. At T=0, all the Cooper pairs are in the ground state with energy gap given by:

$$\Delta(0) = 1.76 k_B T_c \tag{2.9}$$

The temperature-dependent energy gap, $\Delta(T)$ near the critical temperature is given by:

$$\frac{\Delta(T)}{\Delta(0)} = 1.74\sqrt{1 - (\frac{T}{T_c})} \tag{2.10}$$

At nonzero temperature, thermal chaotic motion excites the electron system, and some of the Cooper pairs break and quasiparticles are generated. With increasing the temperature, the quasiparticles are excited across the gap and therefore fewer Cooper pairs are in the superconducting ground state. According to equation (2.10), $\Delta(T)$ goes to zero at T=T_c, and the number of Cooper pairs reduces to zero, and the material returns to its normal state.

2.4.1 BCS Coherence length

Cooper pairs are characterized by the BCS coherence length (size of Cooper pair), ξ_0 which is given by:

$$\xi_0 = \frac{\hbar v_f}{\pi \Delta} \tag{2.11}$$

the quantity ξ_0 characterizes the scale of spatial correlation in a superconductor in the clean limit ($l_e > \xi_0$). Substituting typical values for v_f and Δ [11], we find that ξ_0 is the order of 10^{-4} cm. Recall that the period of a crystal lattice (lattice spacing)

is approximately 10^{-8} cm. Thus the electrons forming the Cooper pair extend over a huge distance of 10^4 lattice spacings. This is a crucial part of the superconducting state: one should think of the pairs as coupled particles, and not as independent ones. However, high T_c superconductors have extremely short coherence lengths on the order of 10^{-7} cm.

2.4.2 Types of superconductors

Superconductors can be classified according to their response to an applied external magnetic field, using the Ginzburg-Landau theory. The Ginzburg-Landau parameter, κ is given by:

$$\kappa = \frac{\lambda}{\xi_0} \tag{2.12}$$

Depending on the value of κ, we can define two types of superconductors:

1. Type I superconductors, where $\kappa < \frac{1}{\sqrt{2}}$, for which the coherence length is larger than the penetration depth. Any applied magnetic field up to a critical magnetic field H_c, won't destroy the coherence of the Cooper pairs (superconducting effect). Once the applied field exceeds H_c, Cooper pairs lose their coherence and thus superconductivity is destroyed, and the material returns to its normal state.

2. Type II superconductors, where $\kappa > \frac{1}{\sqrt{2}}$, for which the coherence length is smaller than the penetration depth. In this case there are two critical fields. H_{c1}, which is called the lower critical magnetic field, and H_{c2} which is called the upper critical magnetic field. For an applied magnetic field up to H_{c1}, type II superconductors behave like a type I superconductor. Above H_{c1}, the flux partially penetrates into the material until the upper critical field H_{c2} is reached. Above H_{c2}, the material returns to the normal state. Between H_{c1} and H_{c2}, the superconductor is in the mixed state. In 1957 Abrikosov analyzed

this state based on the Ginzburg-Landau theory [12, 13, 14]. When the lower critical field H_{c1} is reached, the field begins partially to penetrate into the bulk of the superconductor. Under the influence of the Lorentz force, a fraction of the electrons begin to move in a circle. This leads to the appearance of vortices in the superconductor. The superconducting electrons circulate around the vortex line. The closer the electron is to the vortex axis, the faster the electron circulates. At some distance from the axis, the speed exceeds the critical value, and superconductivity is lost. Thus, the vortex consists of a normal core, in which the magnetic field is large, surrounded by a superconducting region in which the persistent current flows. The diameter of the vortex in conventional superconductors is typically 100 nm. Every vortex carries one flux quantum, Φ_0. As the applied magnetic field increases, the number of vortices increases, and they get closer to each other. When the upper critical field H_{c2} is reached, superconductivity is destroyed and the material returns to its normal state. Some type II superconductors survive magnetic fields (H_{c2}) up to 60 Tesla, or even 150 Tesla in high Tc superconductors.

2.5 Magnetism

Magnetism is a phenomenon known for many centuries. There is a story told from around 900 BC of a Greek shepherd called Magnus. As he walked across a field of black stones, somewhere in Asia Minor, he noticed that the nails on the soles of his shoes adhered to the ore. This region soon after became known as Magnesia. The effect would have been due to large deposits of naturally occurring magnetic iron ore or magnetite that is commonly found in that area. The word magnet comes from the Greek "magnitis lithos", ($\mu\alpha\gamma\nu\eta\tau\eta\varsigma\lambda\iota\theta\varsigma$) which means "magnesian stone". Magnetite then later came to be called loadstone (or lodestone) by the Greeks. Since

it has the ability to align itself in certain directions if allowed to rotate freely, it is being used to indicate the north and south. Another property of lodestone is that two pieces of it can attract or repel each other. So we can describe magnetism as a phenomenon by which some materials attract or repel other materials. Magnetism is associated with electric currents, i.e. the motion of electric charges. There are two types of electron motion. Electrons move in orbits around the nucleus. Therefore, there is a magnetic moment associated with each orbiting electron. Another source of magnetic moment is the spin of the electron. We can think of the electron as spinning about itself, which gives spin moment. The net magnetic moment of an atom is the sum of magnetic moments of each of the constituent electrons, including both orbital and spin contributions. Magnetism can be classified as paramagnetism, diamagnetism, and ferromagnetism. We will be concerned with ferromagnetism only. A good review about magnetism can be found in [3, 4].

2.5.1 Magnetic units

We need units to describe for example how strong magnetic fields are. Units have caused a lot of confusion in electromagnetism. I should say, it does not matter very much which units are chosen as basic units, as long as they are treated in a systematically consistent way. There are two different systems of units. One is called the CGS, which stands for Centimeter-Gram-Second. The other was originally known as the mks system, which stood for Meter-Kilogram-Second, which was later revised into another system, called rmks, standing for Rationalized Meter-Kilogram-Second. This ended up being adopted as an international standard and renamed SI (Systeme International). With this in mind, let us give some basic definitions in magnetism. The first one is the magnetic field, $\mathbf{H}$, which describes the field generated by a free current only. The second one is the magnetic induction, $\mathbf{B}$, in which one should include not only the field generated by the current, but also the magnetization, $\mathbf{M}$

(magnetic moment per unit volume) of the material itself. In SI units, magnetic induction, **B**, is given by:

$$\mathbf{B} = \mu_0(\mathbf{M} + \mathbf{H}) \tag{2.13}$$

The unit of **B** is the Tesla (T). The constant $\mu_0 = 4\pi \times 10^{-7}$ is the permeability of free space and has the units of $\frac{Henry}{m}$. In the CGS system, μ_0 equals one, and **B** is given by:

$$\mathbf{B} = \mathbf{H} + 4\pi\mathbf{M} \tag{2.14}$$

therefore the units of **B**, **H**, and **M** can be used interchangeably. In free space (**M**=0), **B** and **H** are numerically equal to one another, whereas in the SI system, they have different numerical values. To show the confusion, consider for example the earth's magnetic field. In CGS system, it is 0.5 Gauss or 0.5 Oe, however in SI system it is given by (conversion factors are given in table 2.2):

$$0.5G = 50\mu T \quad \text{i.e } \mathbf{B}\text{-field} \tag{2.15}$$

$$0.5Oe = 39.8\frac{A}{m} \quad \text{i.e } \mathbf{H}\text{-field} \tag{2.16}$$

It is obvious that converting G to T is much easier than converting Oe to $\frac{Henry}{m}$. Table 2.2 shows some of the magnetics parameters and their unit conversion factors.

Magnetic term	Symbol	SI unit	CGS unit	Conversion factor
Magnetic induction	**B**	Tesla (T)	Gauss (G)	1 T = 10^4 G
Magnetic field	**H**	Am^{-1}	Oersted (Oe)	1 Am^{-1} = $4\pi\times10^{-3}$ Oe
Magnetization	**M**	Am^{-1}	emu g^{-1}	1 Am^{-1} = 10^{-3} emu cm^{-3}

Table 2.2: Some magnetic properties and their conversion factors in the SI and CGS unit systems.

2.5.2 Ferromagnetism

It was found that certain substances like iron, cobalt, nickel, etc., when cooled below a certain temperature T_C (called the Curie temperature) developed a spontaneous magnetization, even in the absence of an external magnetic field. These materials are called Ferromagnetic materials in which they exhibit parallel alignment of the magnetic moments resulting in large net magnetization, even in the absence of an applied magnetic field. This phenomenon results from the interaction between electron spins known as the exchange interaction. A model of magnetism based on the exchange interaction was proposed by Heisenberg [15] with the following Hamiltonian:

$$H_{Heis} = -2\sum_{i>j} J_{ij}\mathbf{S}_i \cdot \mathbf{S}_j \tag{2.17}$$

where J_{ij} is the exchange integral linking the i^{th} atom with spin $\mathbf{S}_i$ to the j^{th} atom with spin $\mathbf{S}_j$. The ground state of the system is described as ferromagnetic when J_{ij} is positive. In this state all the spins are parallel and oriented in the same direction. Elemental ferromagnets, like Co, Ni, and Fe, are typical ferromagnets with exchange energy (energy required to rotate one atomic spin with response to its neighbors) of the order of an eV. When the temperature increases, thermal motion competes with the exchange forces. Above a critical temperature called the Curie temperature, T_C ($T_C(Co) = 1338K$) the material can no longer maintain its spontaneous magnetization, and hence it loses its ferromagnetic ordering. In 1907, Weiss [16] suggested that ferromagnets below T_C are subdivided into small volume regions called domains. The magnetization is uniform within each domain, but different domains have different magnetization directions, so that the average magnetization of a specimen could be small or even zero. The very simple reason why ferromagnetic materials prefer to be subdivided into domains is that a material always prefers to be in a state in which its energy is a minimum. There are five types of energies associated with ferromagnetic

materials:

1. Exchange energy which tends to keep adjacent magnetic moments parallel to each other.

2. Magnetocrystalline anisotropy which describes the preference of the magnetization to be oriented along certain crystallographic directions.

3. Magnetostatic energy which is a form of anisotropy due to the shape of the ferromagnetic material.

4. Magnetoelastic energy which is part of the magnetocrystalline anisotropy that is proportional to strain.

5. Zeeman energy which is the potential energy of a magnetic moment when an external field is applied.

Competition between these energies gives the overall magnetic structure. The shape and thickness of the ferromagnetic material, as well as growth conditions and substrate materials determine the contribution of each of these energies to the minimum energy of the system. To explain domain formation, consider a magnetized material consisting of a single domain as shown of Figure 2.2a. In this case, it behaves as a block magnet. The magnetocrystalline energy is minimum as all the magnetic moments are parallel to the easy axis, and the exchange energy is minimum as well, because all magnetic moments are in the same direction. Since the material is magnetized, then magnetic poles will appear on both ends, and themselves will be a source of magnetic field. There will be energy associated with this configuration; this energy is called the magnetostatic energy, which is the volume integral of the field over all space. The magnetostatic energy can be reduced by a factor of roughly one half its value [17] by breaking up the magnetization into two domains pointing in opposite directions as illustrated in Figure 2.2b. This brings the poles closer to each other,

thus decreasing the spatial extent of the field outside the crystal. To reduce the magnetostatic energy further, one needs the magnetic pattern shown in Figure 2.2c, in which we have closure domains. Adjacent domains are separated by domain walls in which the magnetization has different directions. Within the domain wall itself, the magnetization must change direction from that in one domain to that in the other domain. Domain wall formation is associated with energy which is proportional to its area. The change in magnetization direction within the wall can be gradual as in Figure 2.3a (resulting in a wide domain wall), or abrupt as in Figure 2.3b (resulting in a thin domain wall). In Figure 2.3a, the dipole moments of the atoms within the domain wall are not pointing along the easy axis of magnetization. This produces large magnetocrystalline anisotropy compared to that of Figure 2.3b. Also we can see from Figure 2.3a that the magnetic moments are gradually rotating by 180^0, and that keeps the exchange energy to a minimum, in contrast to the abrupt rotation shown in Figure 2.3b. Therefore, the domain wall energy is an intrinsic property of the magnetic material, and it depends on the competition between the magnetocrystalline anisotropy (which tends to make the wall as thin as possible) and the strength of the exchange interaction between neighboring atoms (which tends to make the wall as wide as possible). As a result of this competition, the domain wall has a finite width (on the order of 100 nm). The behavior of a magnetic material in an external magnetic field is represented graphically by the magnetization curve (M vs. H) or hysteresis loop, as shown in Figure 2.4. Hysteresis loop can be used to characterize magnetic materials and infer many important parameters about that material. Initially at the origin (point o), the material is at the virgin state, where the magnetization directions of domains are random, so the net magnetization of the material is zero. By applying an external magnetic field in the positive direction, the magnetization is increased and more domains are aligned with the applied field until the magnetization reaches a constant value and the material is saturated (point

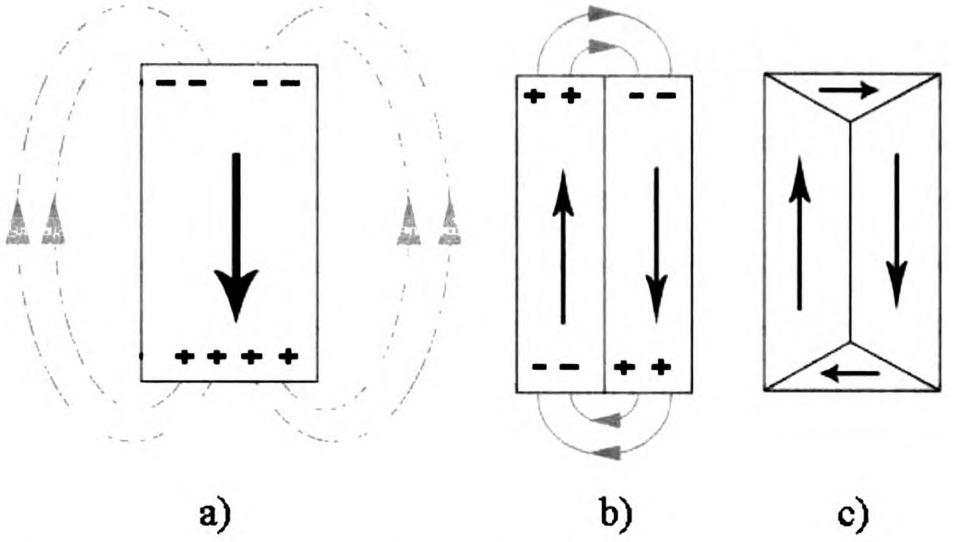

Figure 2.2: Lowering of magnetic field energy by the break up of magnetization into domains. a) single domain. b) two domains. and c) closure domains, adopted from [17].

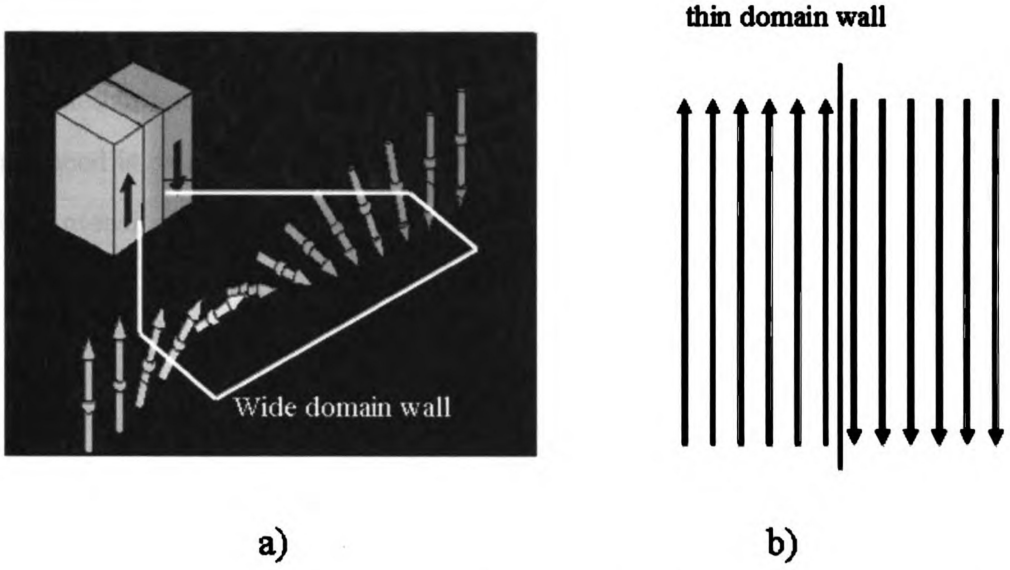

Figure 2.3: Schematic representation of a 180^0 domain wall formation. a) gradual change in magnetization direction. b) abrupt change in magnetization direction.

b). The maximum magnetization of the material is known as the saturation magnetization, M_{sat}. At M_{sat}, the material has a single domain that is aligned with the applied field. The resultant M vs. H curve (o-a-b) is called the initial magnetization curve. If the field is reduced, the magnetization doesn't retrace its original path,o-a-b, instead it decreases more slowly until the applied field reaches zero (point c), then magnetization begins to decrease as a result of domains beginning to align with the negative field. The net magnetization at zero field is known as the remnant (residual) magnetization-M_r, it indicates that the material remains magnetized even in the absence of the external field. Continuing to increase the applied field in the negative direction ultimately brings the magnetization back to zero (point d). The reverse field needed to reduce the magnetization to zero is known as the coercive field, H_c or coercivity. It is a measure of the difficulty or ease to magnetize a material (its value tells how the material is hard or soft). When the reversed field is increased further, the magnetization begins to increase in the same direction. Eventually, it reaches the saturation field M_{sat} in the reversed direction (point e), where the material has a single domain that is aligned with the applied field. By reversing the field again, the magnetization will retrace the loop b-c-d-e-f-g-b. The "S"-shaped curve that has been traced is called the hysteresis curve of a ferromagnetic material for a given set of field intensity extremes (-H and +H).

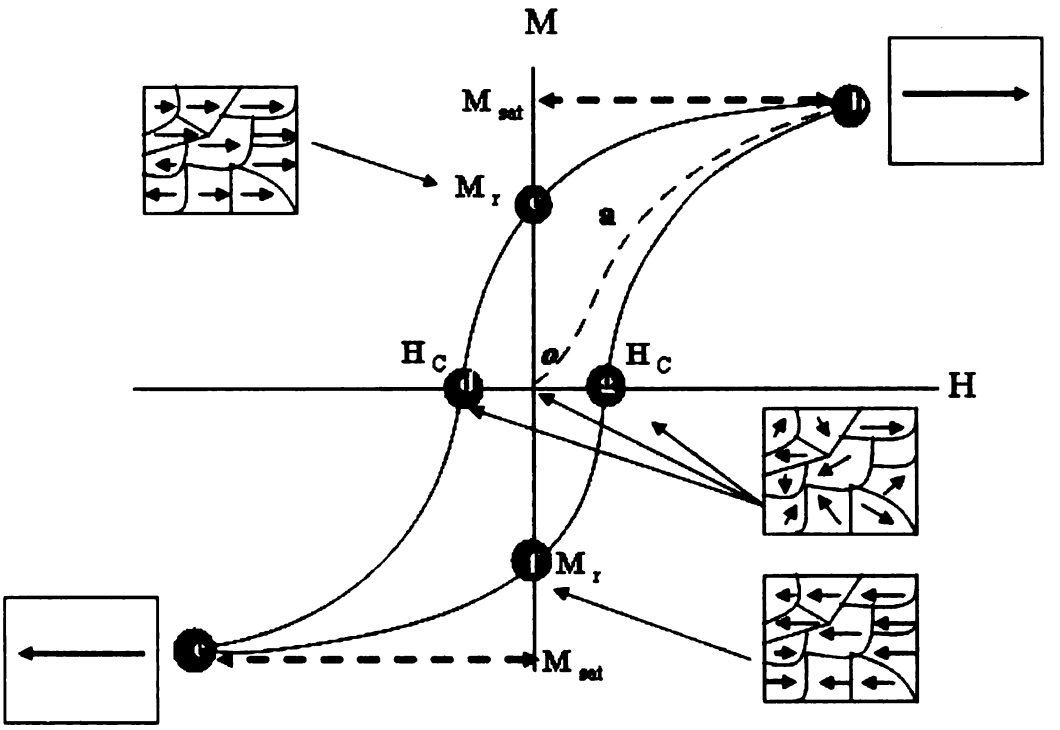

Figure 2.4: The ferromagnetic hysteresis M-H loop showing the effect of the magnetic field on magnetization. In its virgin state the net magnetization is zero (point o). Applying a magnetic field quickly reaches the saturation magnetization, M_{sat}, further increasing the field will not increase the net magnetization (point b). Reducing the field to zero leaves a remnant magnetization, M_r which may be lower than M_{sat} (point c). After switching direction at the coercive field, $-H_C$ (point d), the magnetization reaches $-M_{sat}$ (point e). Reducing the field to zero gives $-M_r$ (point f). Further sweeping the field follows steps (b)-(f). Adopted from [18].

Chapter 3

Theory of the Josephson Effect

In this chapter we discuss the physics of Josephson junctions. In section 3.1, we introduce the Josephson effect, then in section 3.2 we derive the Josephson equations, and in section 3.3, we explain how to characterize Josephson junctions.

3.1 The Josephson effect

Imagine that two superconductors are separated by a thin non-superconducting barrier (insulator in this case) as shown in Figure 3.1. If the insulating barrier is thick, the electron pairs can not get through; but if the barrier is thin enough then there is a probability for Cooper pairs to tunnel through the barrier. This was predicted theoretically in 1962 by Brian Josephson [19, 20], and verified experimentally soon afterwards [21]. This effect is known as the "Josephson effect". Besides displaying a broad range of interesting macroscopic quantum mechanical properties, Josephson junctions offer a vast array of possible applications in analog and digital electronics, such as Superconducting Quantum Interference Devices (SQUID) and detectors. Due to the tunneling of the Cooper pairs, the two superconductors are coupled to each other, and a supercurrent can flow across the barrier. Although the Josephson

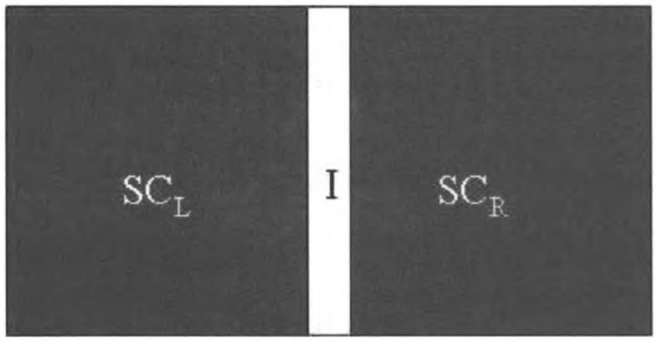

Figure 3.1: Geometry of two superconductors separated from each other by a thin barrier to form Josephson junction.

effect was originally described for a thin insulating barrier, SIS, it is a more general effect, and different Josephson junctions can be identified depending on the material of the barrier such as: a) normal metal (SNS), b) ferromagnetic metal (SFS) and c) semiconductor.

3.2 Feynman's derivation of the Josephson equations

In this section we will derive the basic equations governing the supercurrent passing through a Josephson junction using Feynman's method [22]. Consider an insulator of thickness d_x separating two identical superconductors as shown in Figure 3.1. Through out all the derivation, 1 refers to the superconductor on the left, and 2 refers to the superconductor on the right of the barrier. Let $\Psi_1(\Psi_2)$ be the wave function describing the macroscopic Cooper pair condensate of superconductor 1 (2), respectively. If the width of the barrier, d_x is large, then the two superconductors do not interact with each other, and the time-dependent Schrödinger equations of motion in each superconductor are uncoupled, and the temporal evolution of both

wave functions are:

$$\imath\hbar\frac{\partial\Psi_1}{\partial t} = H_1\Psi_1 \tag{3.1}$$

$$\imath\hbar\frac{\partial\Psi_2}{\partial t} = H_2\Psi_2 \tag{3.2}$$

with

$$H_i\Psi_i = E_i\Psi_i \tag{3.3}$$

where E_i are the energies of the superconducting condensates.

Now, if we bring the two superconductors closer to each other, i.e the width, d_x is very small, then the temporal change of Ψ_1 will be affected by Ψ_2 and vice versa, and as a result Josephson tunneling can occur. The new evolution equations are given by:

$$\imath\hbar\frac{\partial\Psi_1}{\partial t} = E_1\Psi_1 + K\Psi_2 \tag{3.4}$$

$$\imath\hbar\frac{\partial\Psi_2}{\partial t} = E_2\Psi_2 + K\Psi_1 \tag{3.5}$$

where K is the coupling strength (energy).

If we compare the two weakly coupled superconductors with other two-state mechanical systems, then Ψ_1 and Ψ_2 are describing macroscopic states occupied by a large number of particles. So we can write Ψ_1 and Ψ_2 in terms of the particle density n_s of the Cooper pairs as follows:

$$\Psi_1 = \sqrt{n_1}exp(\imath\phi_1) \tag{3.6}$$

$$\Psi_2 = \sqrt{n_2}exp(\imath\phi_2) \tag{3.7}$$

where ϕ_1 and ϕ_2 are the phases of the wave functions Ψ_1 and Ψ_2, respectively.

Substituting Eq's. (3.6) and (3.7) in Eq's. (3.4) and (3.5), we obtain:

$$\imath\hbar[\imath\sqrt{n_1}exp(\imath\phi_1)\dot{\phi_1} + \frac{\dot{n_1}}{2\sqrt{n_1}}exp(\imath\phi_1)] = E_1\sqrt{n_1}exp(\imath\phi_1) + K\sqrt{n_2}exp(\imath\phi_2) \quad (3.8)$$

$$\imath\hbar[\imath\sqrt{n_2}exp(\imath\phi_2)\dot{\phi_2} + \frac{\dot{n_2}}{2\sqrt{n_2}}exp(\imath\phi_2)] = E_2\sqrt{n_2}exp(\imath\phi_2) + K\sqrt{n_1}exp(\imath\phi_1) \quad (3.9)$$

Rewriting Eqn. (3.8) leads to:

$$exp(\imath\phi_1)[\frac{\dot{n_1}}{2\sqrt{n_1}} + \imath\sqrt{n_1}\dot{\phi_1}] = -\frac{\imath}{\hbar}[E_1\sqrt{n_1}exp(\imath\phi_1) + K\sqrt{n_2}exp(\imath\phi_2)] \quad (3.10)$$

Separating real and imaginary parts in Eqn. (3.10)

$$\cos\phi_1\frac{\dot{n_1}}{2\sqrt{n_1}} - \sin\phi_1\sqrt{n_1}\dot{\phi_1} = \frac{1}{\hbar}[E_1\sqrt{n_1}\sin\phi_1 + K\sqrt{n_2}\sin\phi_2] \quad (3.11)$$

$$\sin\phi_1\sqrt{n_1}\dot{\phi_1} + \cos\phi_1\sqrt{n_1}\dot{\phi_1} = -\frac{1}{\hbar}[E_1\sqrt{n_1}\cos\phi_1 + K\sqrt{n_2}\cos\phi_2] \quad (3.12)$$

multiplying Eqn. (3.11) by $\cos\phi_1$ and Eqn. (3.12) by $\sin\phi_1$, and adding them together yield,

$$\frac{\dot{n_1}}{2\sqrt{n_1}} = \frac{K}{\hbar}\sqrt{n_2}\sin(\phi_2 - \phi_1) \quad (3.13)$$

On the other hand, multiplying Eqn. (3.11) by $\sin\phi_1$ and Eqn. (3.12) by $\cos\phi_1$, and adding them together yield,

$$\hbar\sqrt{n_1}\dot{\phi_1} = -[E_1\sqrt{n_1} + K\sqrt{n_2}\cos(\phi_2 - \phi_1)] \quad (3.14)$$

Similarly

$$\frac{\dot{n_2}}{2\sqrt{n_2}} = -\frac{K}{\hbar}\sqrt{n_1}\sin(\phi_1 - \phi_2) \quad (3.15)$$

$$\hbar\sqrt{n_2}\dot{\phi_2} = -[E_2\sqrt{n_2} + K\sqrt{n_1}\cos(\phi_2 - \phi_1)] \quad (3.16)$$

The coupling between the two superconductors means that Cooper pairs can be ex-

changed between them, so $\dot{n_1} = -\dot{n_2}$. Also for simplicity, assume that the two superconductors are identical ($n_1 = n_2$) then using Eqn. (3.13) and Eqn. (3.15), we have

$$\dot{n_1} = \frac{K}{\hbar} n_1 \sin(\phi_2 - \phi_1) \tag{3.17}$$

The current density is given by

$$J = 2e\frac{\partial n_1}{\partial t} \tag{3.18}$$

$$J(\phi) = 2e\frac{K}{\hbar} n_1 \sin\phi \tag{3.19}$$

$$J(\phi) = J_c \sin\phi \tag{3.20}$$

where $\phi = \phi_2 - \phi_1$ is the phase difference between the two superconductors, and J_c is the maximum possible density of supercurrent that can flow through the junction. This is the first Josephson equation. If we subtract Eqn. (3.16) from Eqn. (3.14), we get

$$\frac{\partial \phi}{\partial t} = -\frac{1}{\hbar}\Delta E \tag{3.21}$$

If a voltage source is connected to the two superconductors, then a difference of energy $e^*(V_2 - V_1) = e^*V = \Delta E$ appears between the two sides of the junction. Since we are talking about Cooper pairs, then e^* = -2e, then we can rewrite Eqn. (3.21)

$$\frac{\partial \phi}{\partial t} = \frac{2e}{\hbar} V \tag{3.22}$$

this the second Josephson equation describing the temporal evolution of the phase difference.

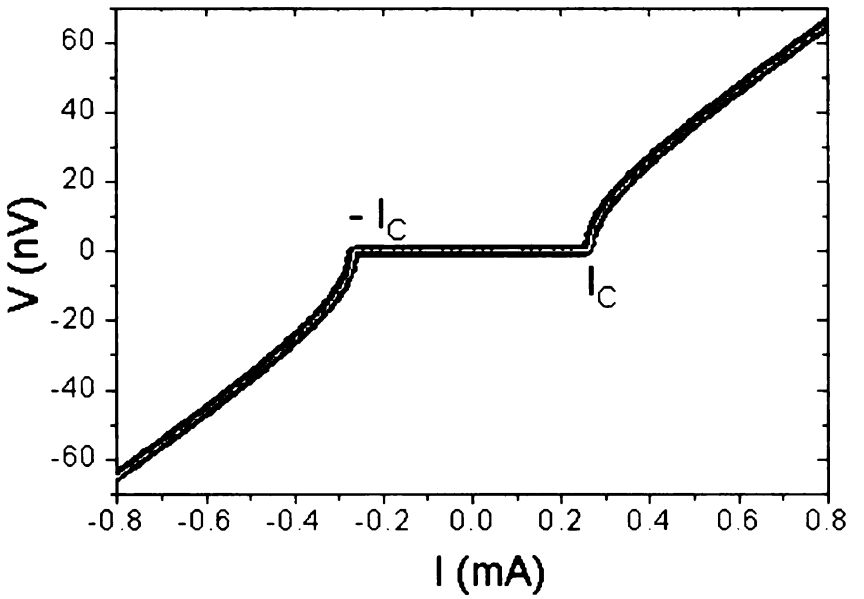

Figure 3.2: Voltage vs current for one of our Josephson junctions. The white solid line is a fit to Eqn. 3.23

3.3 Characterization of Josephson junctions

We characterized our Josephson junctions by measuring their current voltage characteristics, I-V characteristics, and their response to an applied magnetic field. In the following sub-sections I will describe both of them in more detail.

3.3.1 Current voltage characteristics

The critical current of a Josephson junction can be deduced from its Current Voltage characteristic (I-V). I-V characteristics can be measured by passing a current through the junction and measuring the voltage between the superconducting electrodes. Figure 3.2 shows an I-V curve typical for our SFS Josephson junctions. The I-V curve follows the Resistively Shunted Junction (RSJ) model [23] for overdamped junctions,

given by:

$$V(I) = \frac{I}{|I|} R_N \mathrm{Re}[(I^2 - I_c^2)^{1/2}] \tag{3.23}$$

where R_N is the resistance at very large currents, and I_C is the critical current. Occasionally, we find that the I-V curves are shifted horizontally, so that the critical current is not exactly the same in the positive and negative current directions. In such cases, we average the critical currents in the two current directions.

3.3.2 Josephson junction response to magnetic field

Another way of characterizing Josephson junctions is to observe their response to an applied magnetic field in plane of junction. I will discuss first the simple case of two superconductors separated by a normal metal layer, SNS junction. Then I will extend this discussion for the the case of two superconductors separated by a ferromagnetic metal layer, SFS junction. Before going into details, let me introduce the concept of Josephson penetration depth, λ_J.

3.3.3 Josephson penetration depth

As a superconductor screens magnetic field over the length scale λ_L, known as the London penetration depth; Josephson junctions have an analogous effect, Josephson currents will be screened from the interior of the junction due to the self generated magnetic field (Φ_F). That means the Josephson current will be confined in a length scale governed by the Josephson penetration depth, λ_J,

$$\lambda_J = \sqrt{\frac{\Phi_0}{2\pi\mu_0 J_c(2\lambda_L + t)}} \tag{3.24}$$

where Φ_0 is the magnetic flux quantum, and J_c is the critical current density (current/area). Josephson penetration depth is very important parameter since it deter-

mines the junction behavior. We have to distinguish between two types of Josephson junction;

1. Long Josephson junction. A Josephson junction is considered long if the width, L of the junction is larger than the Josephson penetration depth ($\lambda_J < L$). In this case, one needs to take into account the magnetic filed generated by the Josephson current itself. In this case the current flow is not uniform, and the diffraction pattern (which will be derived later) deviates from the ideal one.

2. Short Josephson junction. A Josephson junction is considered short if the width, L of the junction is smaller than the Josephson penetration depth ($\lambda_J > L$). In this case, the magnetic field generated by the Josephson current (self-field) is negligibly small compared to the externally applied field. As a result, the applied magnetic field penetrates the junction uniformly, and the supercurrent density will be uniform across the junction.

All Josephson junctions studied in this thesis satisfied the short junctions limit. A more detailed discussion can be found in [24, 25].

3.3.4 SNS Josephson junction response to magnetic field

An external magnetic field gives rise to a modulation of the critical current of the junction. The simplest case to consider is shown in Figure 3.3a for a short SNS Josephson junction. In this case the redistribution of the current in the junction under the influence of its own self-field can be neglected. In zero applied magnetic field the phase difference between the electrodes is uniform and the dc Josephson relation holds. When an external field H_{ext} is applied in the plane of the barrier it penetrates not only the barrier (thickness t), but also the electrodes up to the London penetration depth λ_L. So the effective thickness is given by:

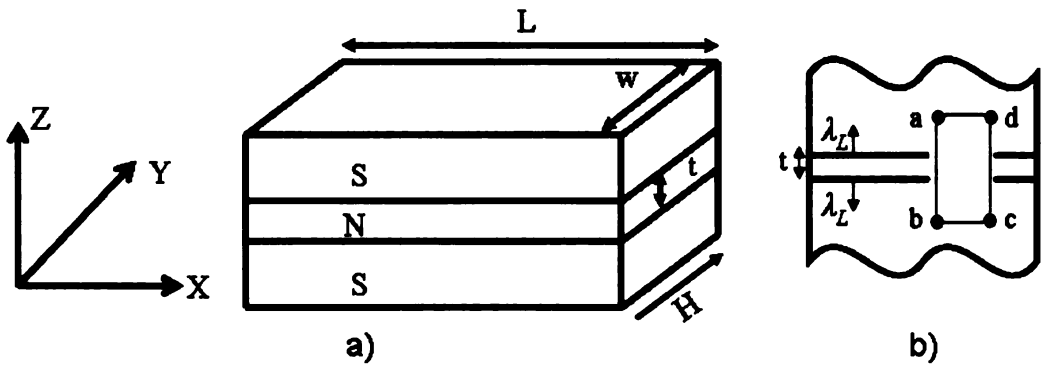

Figure 3.3: Cartoon of a Josephson junction in a magnetic field. Field applied in the plane of the junction penetrates the London penetration depth λ_L into both the superconductors.

$$d_{eff} = t + 2\lambda_L \tag{3.25}$$

The superconducting layers will generate screening currents that restrict the penetration of the magnetic field within λ_L. Quantum mechanically, the current density is given by:

$$\mathbf{J} = \frac{e^*\hbar}{2im^*}(\Psi^*\nabla\Psi - \Psi\nabla\Psi^*) - \frac{e^{*2}}{m^*c}|\Psi|^2\mathbf{A} \tag{3.26}$$

where e^* = -2e and m^* = 2m are the Cooper pair charge, and mass, respectively. **A** is a vector potential of the electromagnetic field.

$$\mathbf{H} = \nabla \times \mathbf{A} \tag{3.27}$$

The current density, depends on the phase of the wavefunction describing the quantum state of Cooper pairs by:

$$\Psi = \sqrt{n_s}exp(\imath\phi(r,t)) \tag{3.28}$$

Substituting equation 3.28 into equation 3.26, we get:

$$\mathbf{J} = \frac{en_s\hbar}{m}(\nabla\phi - \frac{2e}{c\hbar}\mathbf{A}) \tag{3.29}$$

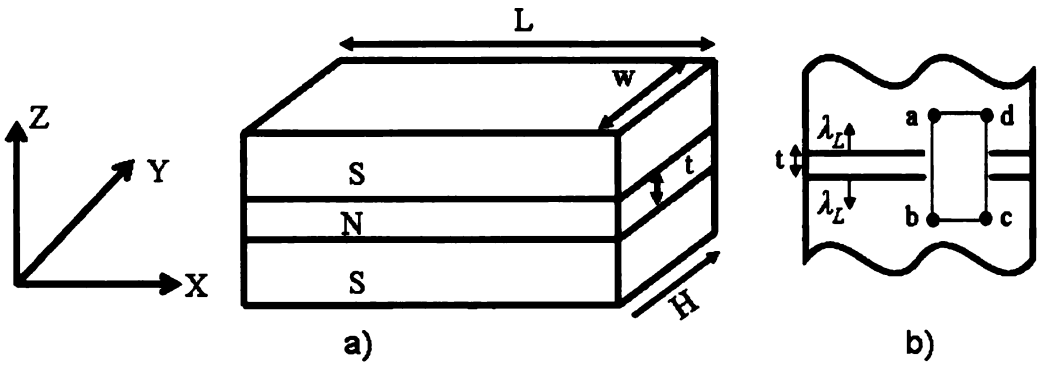

Figure 3.3: Cartoon of a Josephson junction in a magnetic field. Field applied in the plane of the junction penetrates the London penetration depth λ_L into both the superconductors.

$$d_{eff} = t + 2\lambda_L \tag{3.25}$$

The superconducting layers will generate screening currents that restrict the penetration of the magnetic field within λ_L. Quantum mechanically, the current density is given by:

$$\mathbf{J} = \frac{e^*\hbar}{2im^*}(\Psi^*\nabla\Psi - \Psi\nabla\Psi^*) - \frac{e^{*2}}{m^*c}|\Psi|^2\mathbf{A} \tag{3.26}$$

where e^* = -2e and m^* = 2m are the Cooper pair charge, and mass, respectively. **A** is a vector potential of the electromagnetic field.

$$\mathbf{H} = \nabla \times \mathbf{A} \tag{3.27}$$

The current density, depends on the phase of the wavefunction describing the quantum state of Cooper pairs by:

$$\Psi = \sqrt{n_s}exp(\imath\phi(r,t)) \tag{3.28}$$

Substituting equation 3.28 into equation 3.26, we get:

$$\mathbf{J} = \frac{en_s\hbar}{m}(\nabla\phi - \frac{2e}{c\hbar}\mathbf{A}) \tag{3.29}$$

and after rearrangement

$$\nabla\phi = \frac{m}{en_s\hbar}\mathbf{J} + \frac{2\pi}{\Phi_0}\mathbf{A} \tag{3.30}$$

Integrating equation 3.30 around the contour shown in Figure 3.3b, taking into account the fact that deep inside the superconductors, the current density drops to zero, we get

$$\frac{\partial\phi}{\partial x} = \frac{2\pi}{\Phi_0}d_{eff}H_y \tag{3.31}$$

Similarly, if H_x is not zero, then

$$\frac{\partial\phi}{\partial y} = \frac{-2\pi}{\Phi_0}d_{eff}H_x \tag{3.32}$$

In general the expression for the phase difference is:

$$\nabla\phi = \frac{2\pi}{\Phi_0}d_{eff}H \times \hat{z} \tag{3.33}$$

where $\hat{z}$ is a unit vector normal to the plane of the junction. This equation states that the spatial dependence of the phase difference across the junction (hence the Josephson current) is proportional to the spatial dependence of the magnetic field inside the junction. If the magnetic field is uniform, then equation 3.31 leads to,

$$\phi(x) = \phi_0 + \frac{2\pi}{\Phi_0}d_{eff}H_y x \tag{3.34}$$

and the first Josephson equation (equation 3.20) is then written as:

$$J(x) = J_c \sin(\phi_0 + kx) \tag{3.35}$$

with $k = \frac{2\pi}{\Phi_0} d_{eff} H$. The critical current density, J(x) varies sinusoidally in the x-direction with a period $\triangle$x

$$\triangle x = \frac{2\pi}{k} \tag{3.36}$$

or

$$\triangle x d_{eff} H = \Phi_0 \tag{3.37}$$

showing that the magnetic flux through the junction over a single oscillation period corresponds to a single flux quantum. The total supercurrent is given by $\int J(x)dx$,

$$I_c(H) = \int_{\frac{-L}{2}}^{\frac{L}{2}} J_c \sin(\phi_0 + kx)dx \tag{3.38}$$

$$I_c(H) = Im[\exp(i\phi_0) \int_{-\infty}^{\infty} J_c \exp(ikx)dx] \tag{3.39}$$

Since J_c is zero outside the junction, i. e $|x| > \frac{L}{2}$, we have replaced the integration limits by $\pm\infty$.

$$I_c(H)^{max} = Im[\int_{-\infty}^{\infty} J_c \exp(ikx)dx] \tag{3.40}$$

For the case of a short SNS Josephson junction with square cross section, then the maximum Josephson current is given by:

$$I(\Phi) = I_C(0) \frac{\sin(\frac{\pi\Phi}{\Phi_0})}{(\frac{\pi\Phi}{\Phi_0})} \tag{3.41}$$

where $\Phi = L d_{eff} H_y$ is the total magnetic flux going into the junction. This pattern is called the Fraunhofer pattern, due to its similarity to the pattern produced in single-slit diffraction of light, and was first observed by Rowell [26]. Minima in I_C occur where an integer number of flux quanta are introduced into the barrier. Similarly for SNS Josephson junctions with circular cross section, the magnetic field modulates

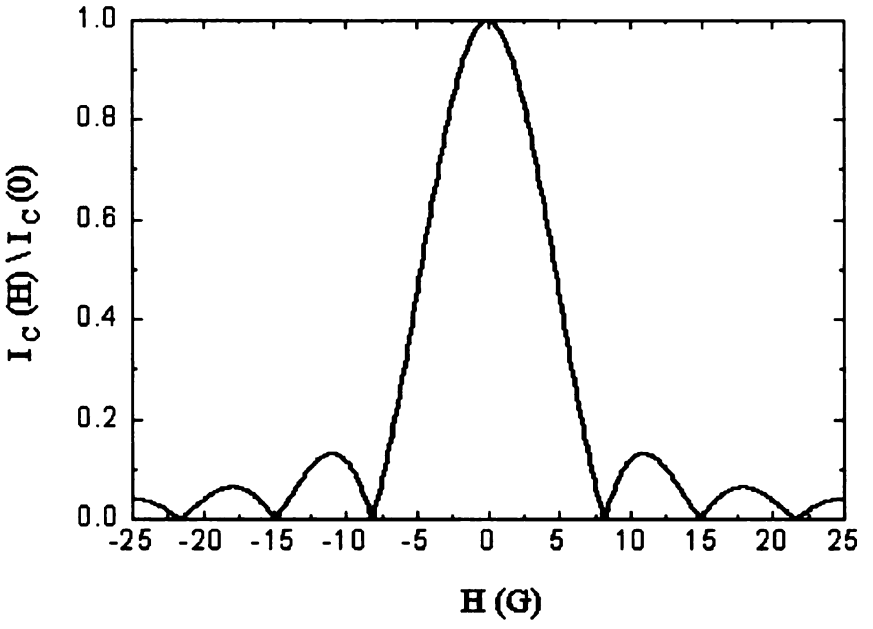

Figure 3.4: Critical current Vs in-plane magnetic field for a circular Josephson junction.

the critical current according to:

$$I(\Phi) = I_c(0)\frac{2 \times J_1(\frac{\pi\Phi}{\Phi_0})}{(\frac{\pi\Phi}{\Phi_0})} \tag{3.42}$$

where J_1 is the Bessel function of type 1. This pattern is called an Airy pattern, and is shown in Figure 3.4. The pattern is qualitatively similar to the Fraunhofer diffraction pattern, but the first minima are spaced more widely apart in field than the subsequent minima.

3.3.5 SFS Josephson junction response to magnetic field

If the barrier is replaced with a ferromagnetic material, then the total magnetic flux threading the junction comes from two sources. The first one is the intrinsic magnetic flux enclosed by a Josephson junction of size L and thickness t. If the magnetization

M is uniform, the intrinsic flux is given by (in SI units):

$$\Phi_F = tL\mu_0 M \tag{3.43}$$

where μ_0 is the permeability of free space ($4\pi \times 10^{-7}$ H/m). The second source is the flux from the external magnetic field, and is given by:

$$\Phi_{ext} = H_{ext}(t + 2\lambda_L)L \tag{3.44}$$

then the total magnetic flux through the ferromagnetic layer is:

$$\Phi_{tot} = tL\mu_0 M + H_{ext}(t + 2\lambda_L)L \tag{3.45}$$

It is clear from this equation that the intrinsic magnetic flux trapped in the junction can shift the diffraction pattern, and then the peak (maximum critical current usually at zero applied field) occurs at a non zero magnetic field. In order to cancel the intrinsic magnetic flux, we need to apply a magnetic field in one direction (opposite to direction of the shift) given by (after setting $\Phi_{tot} = 0$)

$$\Delta H_{ext} = -\frac{\mu_0 tM}{2\lambda_L + t} \tag{3.46}$$

In macroscopic samples the magnetization breaks into domains (see Figure 6.2), and Eqn. (3.45) is not valid. Instead, one must integrate the current density across the area of the junction, taking into account the spatial dependence of the magnetic vector potential $\vec{A}$ due to the domains. We can rewrite equation (3.30) (with J = 0) as follows:

$$\nabla\phi = \frac{2\pi}{\Phi_0}\int \mathbf{dl} \times \mathbf{B} \tag{3.47}$$

where I used $\mathbf{B} = \mu_0(\mathbf{H} + \mathbf{M}) = \nabla \times \mathbf{A}$. For illustration assume $\mathbf{M}$ and therefore $\mathbf{B}$ depend only on x and have only nonzero y-component. $\mathbf{B}$ = B(x) $\hat{y}$, also assume dl along the z-axis, dl = dz $\hat{z}$, then

$$\mathbf{dl} \times \mathbf{B} = -B(x)dz\widehat{x}. \tag{3.48}$$

so we can rewrite equation 3.47 as follows:

$$\frac{\partial \phi}{\partial x} = -\frac{2\pi}{\Phi_0}\int B(x)dz \tag{3.49}$$

Since the magnetic field doesn't penetrate the bulk of the superconductor, then $\mathbf{H}$ is non-zero only between $(-\frac{d_{eff}}{2}, \frac{d_{eff}}{2})$. While $\mathbf{M}$ is non-zero only between $(-\frac{t}{2}, \frac{t}{2})$, so integrating equation 3.49 gives

$$\phi(x) = \phi_0 - \frac{2\pi\mu_0}{\Phi_0}(d_{eff}H + tM(x)) \tag{3.50}$$

The total Josephson current $I_c(H)$ is then,

$$I_c(H) = \int J(x,y)dxdy \tag{3.51}$$

where

$$J(x,y) = J_c \sin(\phi_0 + \frac{2\pi\mu_0}{\Phi_0}(d_{eff}H + tM(x)) \tag{3.52}$$

The term containing the magnetization performs a random walk as one moves across the sample, due to the domains pointing in random directions. If the magnetic domains are very small and/or the magnetization is very weak (weak ferromagnetic alloys), then that term stays near zero in all parts of the junction, and the critical current is hardly affected. If, however, the magnetic domains are large and/or have large magnetization as in the case of strong ferromagnet, the contribution to the phase

due to the magnetization deviates far from zero as it crosses even a single domain, thus severely suppressing the critical current. This can lead to complete destruction of the Fraunhofer pattern. This is clearly seen in Figure 6.1, which shows data for an S/F/S junction of diameter 40 μm, with a 5 nm thick Co layer.

Chapter 4

Josephson junctions with ferromagnetic interlayer

In chapters one and two, I introduced the basic theory of superconductivity and ferromagnetism. In this chapter, I will introduce some fascinating aspects that appear when a superconductor is placed in intimate contact with a nonmagnetic (N) or ferromagnetic (F) metals. In section 4.1 the proximity effect between a superconductor and a normal metal or ferromagnetic metal is explained, followed by the theory of π junctions in section 4.2. In section 4.3, a comparison between weak and strong ferromagnets is introduced, and finally some of the previous studies are introduced in section 4.4.

4.1 Proximity effect

In Chapter 2 of this thesis, I was talking about what may be called "intrinsic" superconductivity, in which some materials make a transition to the superconducting phase if cooled to a temperature below their critical temperature, T_C. Beside this intrinsic type of superconductivity, another type may exist, and is known as induced

superconductivity. In this latter type of superconductivity, a material which by itself is not a superconductor may under certain conditions have induced superconducting behavior. This transition to the superconducting phase happens as a result of the proximity effect, which is the topic of the following two subsections.

4.1.1 Proximity effect in superconductor/normal metal (S/N)

When a superconductor is brought into a contact with nonsuperconducting metal (normal or ferromagnet), then the two influence each other in the vicinity of the interface between the two metals on a length scale of the order of the coherence lengths. The appearance of the superconducting correlations in the non-superconducting metal is called the proximity effect. On the other hand, the suppression of superconductivity in the superconductor is known as the inverse proximity effect. The microscopic mechanism that explains the proximity effect is Andreev reflection. Imagine an electron with energy ϵ close to the Fermi energy approaching the SN interface from the N-side. Because of the energy gap, the electron can't be transferred into the superconductor. If that electron finds a time-reversed electron with energy - ϵ, then the two electrons can form a Cooper pair on the S-side of the SN interface. The disappearance of the second electron can be seen as creation of a hole in the N-side. From the S-side, an electron is Andreev-reflected as a hole as shown in Figure 4.1. Proximity effect can also be described using the language of electrons only [27]. In that language, the inverse Andreev process can be viewed as "leakage" of a Cooper pair from S-side to N-side of the interface. The two electrons from the Cooper pair enter N with nearly opposite momenta as shown in Figure 4.2 The wavefunctions of the two electrons in N remain in phase for times of the order $\hbar/\epsilon$, which translates into the length $\hbar v_f/\epsilon$ in the clean limit or $\sqrt{\frac{\hbar D}{\epsilon}}$in the dirty limit, where v_f, $D = \frac{v_f l_e}{3}$ and $l_e = v_f \tau$, are the Fermi velocity, diffusion constant of the N metal, and the mean free path of the conduction electrons, respectively. At finite temperature, we can define the normal

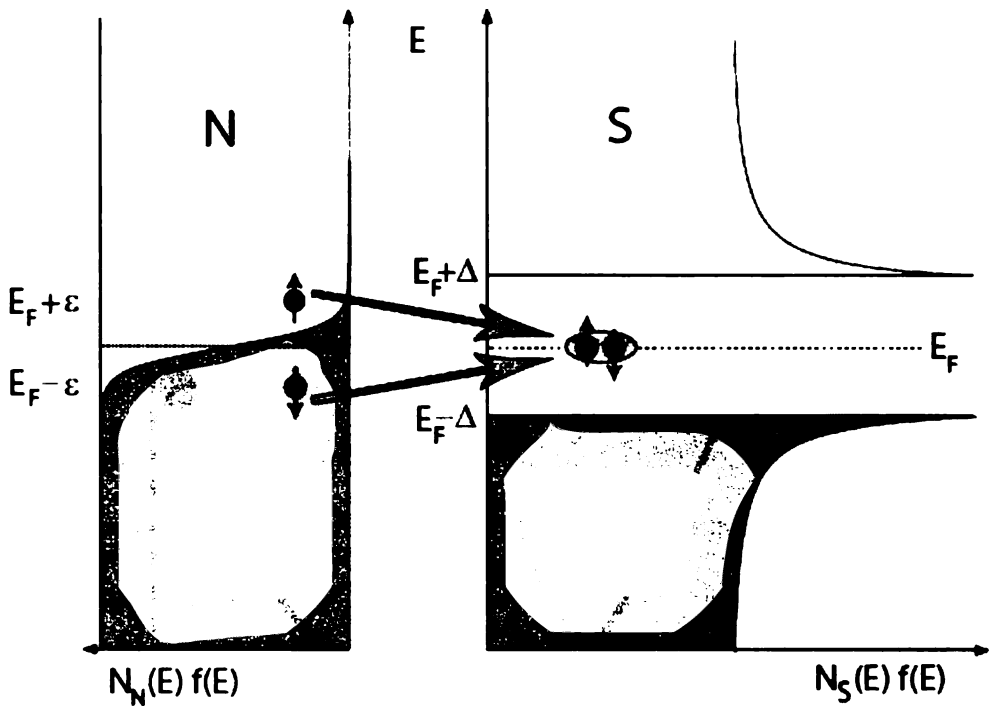

Figure 4.1: Description of the Andreev-reflection at a SN interface. An incoming electron with energy smaller than the superconducting energy gap from the normal metal can only enter the superconductor by involving a second electron of opposite spin and momentum, to form a Cooper-pair in S.

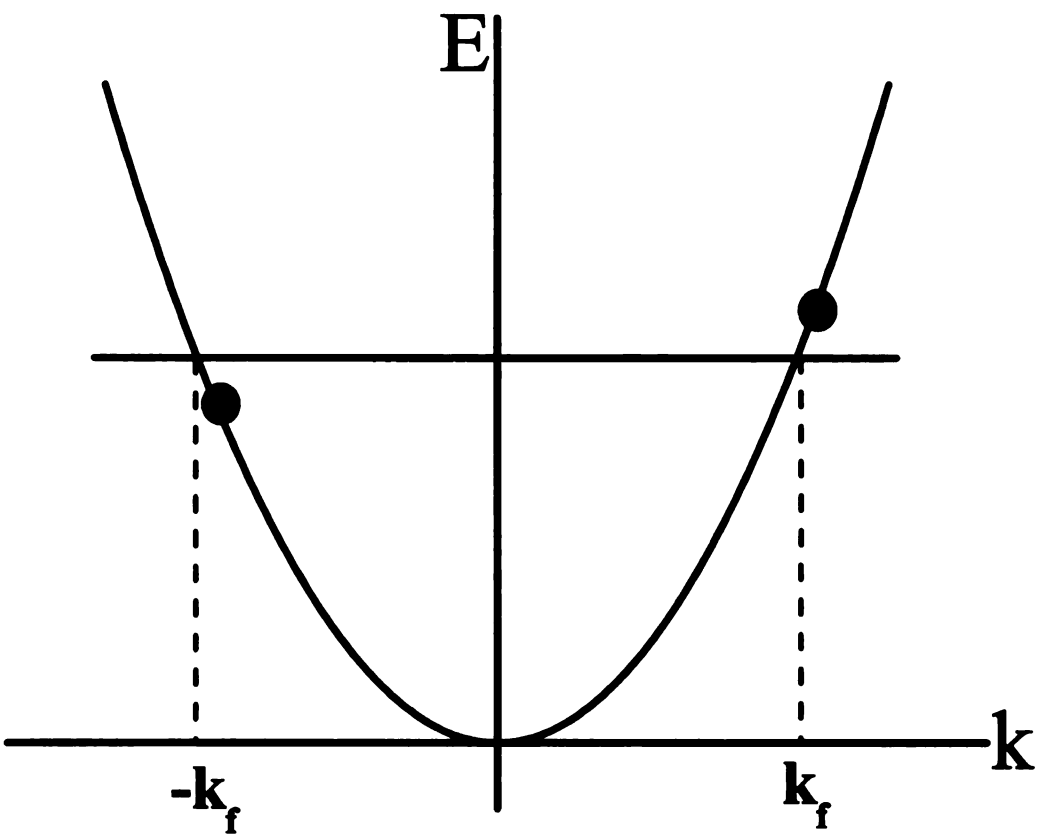

Figure 4.2: Dispersion relation in a normal metal, showing two electrons that have "leaked" from S into N.

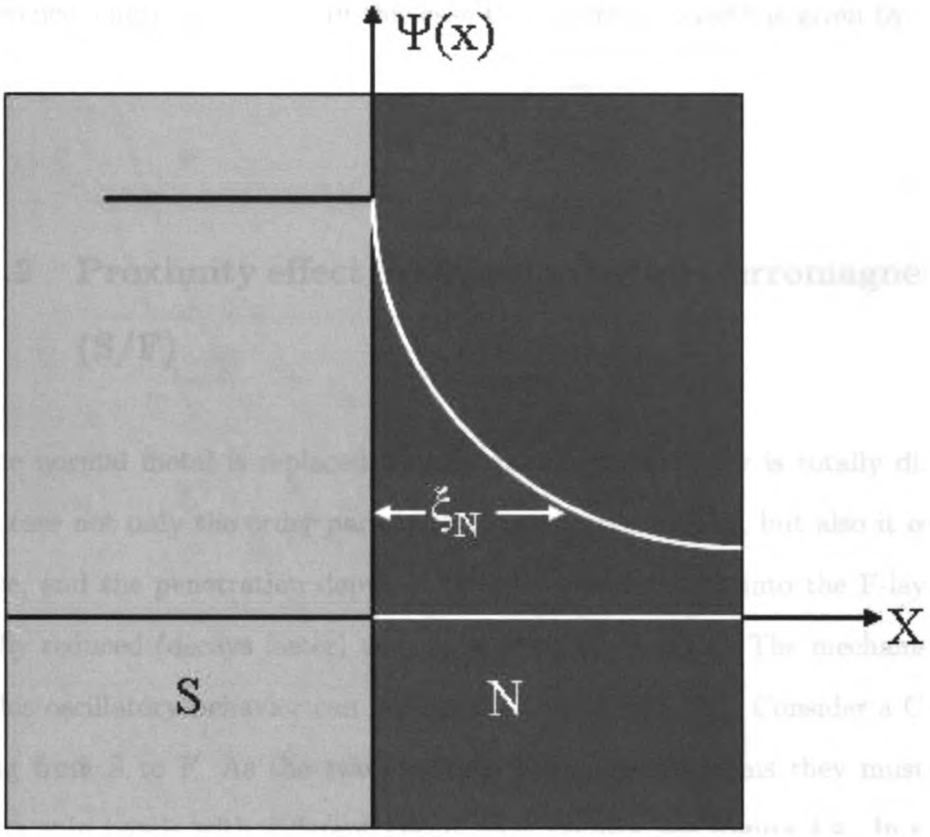

Figure 4.3: Proximity effect in SN structures: The superconducting pair amplitude penetrates into the normal metal (N) over the length scale ξ_N known as the normal metal coherence length.

metal Coherence length as the average length on which the two electrons maintain their coherence. This is shown in Figure 4.3. At finite temperature, in the clean limit (the mean free path of the electrons is larger than the coherence length, $l_e > \xi_N$), it has the form [28]:

$$\xi_N^{clean} = \frac{\hbar v_f}{2\pi k_B T} \tag{4.1}$$

where v_f and k_B are the Fermi velocity and the Boltzmann's constant. On the other hand, the dirty limit is defined such that the mean free path is smaller than the

coherence length ($l_e < \xi_N$). In this case the coherence length is given by:

$$\xi_N^{dirty} = \sqrt{\frac{\hbar D}{2\pi k_B T}} \tag{4.2}$$

4.1.2 Proximity effect in superconductor/ferromagnetic metal (S/F)

If the normal metal is replaced by a ferromagnet, the story is totally different. In this case not only the order parameter decays exponentially, but also it oscillates in space, and the penetration depth of the pair wavefunction into the F-layer is drastically reduced (decays faster) as compared to the N-layer. The mechanism leading to this oscillatory behavior can be explained as follows [27]. Consider a Cooper pair going from S to F. As the two electrons have opposite spins they must enter opposite spin bands with different Fermi wave vectors, see Figure 4.4. In the Cooper pair, the electron with the spin parallel to the exchange field decreased its potential energy, while the electron with spin anti-parallel to the exchange field raised its potential energy by the same amount. The ferromagnetic exchange field E_{ex} splits the energies of the spin up and spin down electron in a Cooper pair. Conservation of energy requires that electrons adjust their kinetic energy, and shift their momentum by $\Delta P = E_{ex}/\hbar v_f$. As initially the electrons had Fermi wave vectors in opposite directions but equal magnitudes, this leads to a nonzero center of mass momentum, $Q = K_f^{\uparrow} - K_f^{\downarrow} = 2E_{ex}/\hbar v_f$. If the spin up and down configurations are interchanged (as required by Fermionic antisymmetry), then the Cooper pair obtains a center of mass of the opposite sign $-Q$. The order parameter is the average over all Cooper pair configurations. This causes the center of mass wave function of the Cooper pair to oscillate in space as $\cos(Qx)$, where x is normal to the SF interface. The wave function order parameter not only oscillates in space, but also decays exponentially away

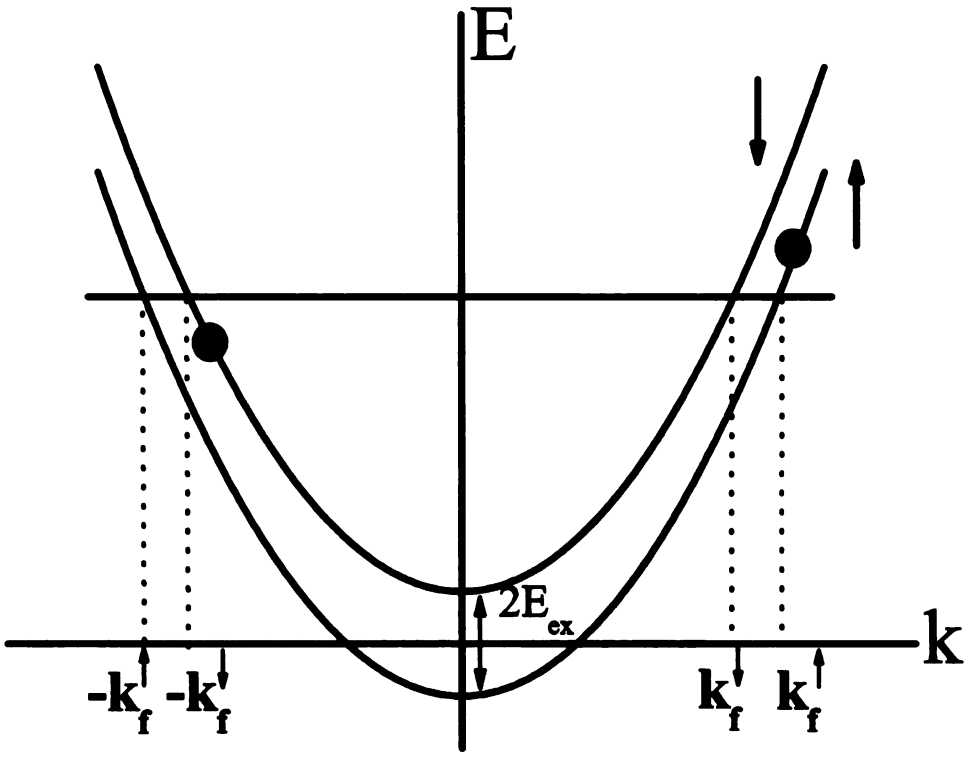

Figure 4.4: Cooper pair leakage into F from S. In this case there is a shift in K_f of the two electrons due to the exchange energy of the ferromagnetic metal.

from the SF interface as in the case of SN interface, i.e. $\Psi(x) \propto exp(-x/\xi_F)\cos(Qx)$, where $Q = 1/\xi_F$. This is shown in Figure 4.5 The superconducting coherence length in the ferromagnetic layer is then defined as the decay length of the superconducting correlations in the ferromagnetic layer, which in the clean limit is given by:

$$\xi_F^{clean} = \frac{\hbar v_f}{2E_{ex}} \tag{4.3}$$

and in the dirty limit

$$\xi_F^{dirty} = \sqrt{\frac{\hbar D}{E_{ex}}} \tag{4.4}$$

If the exchange energy is large compared to the temperature $E_{ex} > k_B T$, then the coherence length is much shorter than in the case of the superconductor-normal metal

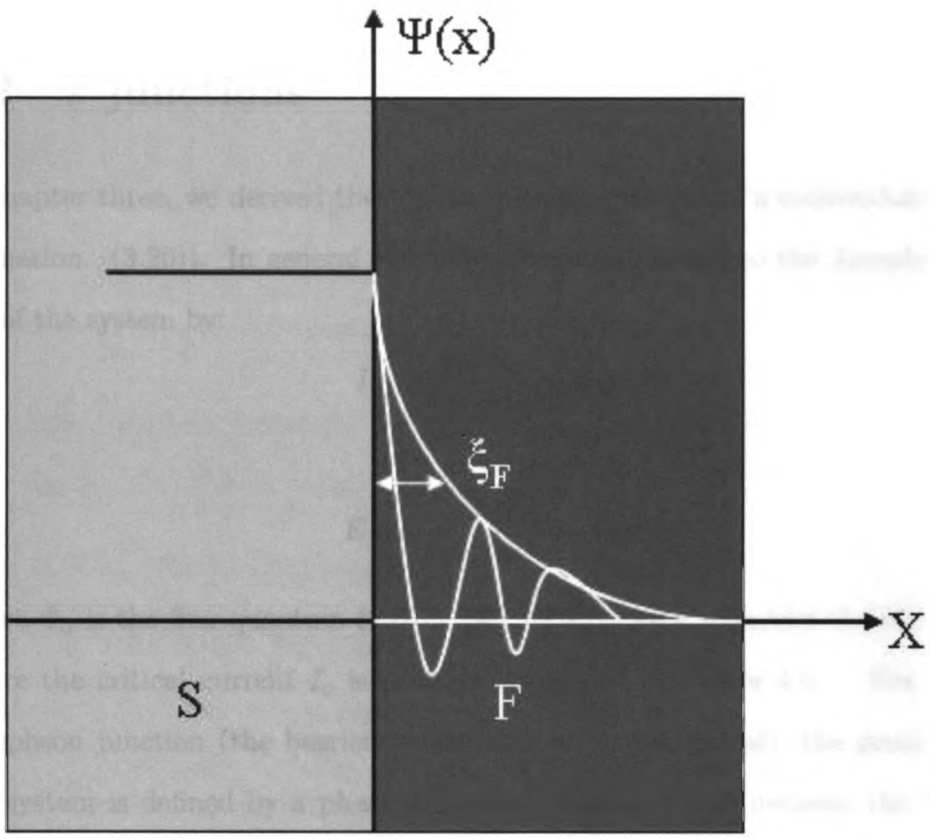

Figure 4.5: Proximity effect in SF structures: The superconducting pair amplitude oscillates and decays exponentialy in the F-layer over the length scale ξ_F known as the normal metal coherence length set by the exchange field, $E_e x$.

proximity effect. This is true for strong elemental ferromagnets like Co, Ni, and Fe, in which the coherence length has a typical value of 1 nm. However, one can overcome this difficulty by using diluted ferromagnetic alloys (weak ferromagnetic alloys) with small exchange energies. In this case the induced superconducting correlations can penetrate deeper in the ferromagnetic layer, on the order of few nm.

4.2 π junctions

In chapter three, we derived the the Josephson equations of a conventional junction (Equation. (3.20)). In general the supercurrent is related to the Josephson energy E_J of the system by:

$$I_s = \frac{2\pi}{\Phi_0}\frac{\partial E_J}{\partial \phi} = I_c \sin\phi \tag{4.5}$$

or

$$E_J(\phi) = \frac{\Phi_0 I_c}{2\pi}(1 - \cos\phi) \tag{4.6}$$

where Φ_0 is the flux quantum ($2.07 \times 10^{-15} T.m^2$) First, consider the standard case where the critical current I_c is positive, as shown in Figure 4.6. For a classical Josephson junction (the barrier is insulator or normal metal), the ground state of the system is defined by a phase difference of zero, $\phi = 0$ between the two superconductors. In 1965, Kulik [29] studied spin flip tunneling through an insulator with magnetic impurities, and predicted a negative critical current $I_c < 0$. In 1977, Bulaevskii et al. [30] showed that under certain conditions, spin flip tunneling could dominate direct tunneling through a barrier with magnetic impurities leading to a negative supercurrent, $I_c < 0$, as shown in Figure 4.7. The ground state is shifted to a phase difference of $\phi = \pi$. Josephson junctions with $\phi = \pi$ are called π-junctions. In 1982, Buzdin [31] studied SFS Josephson junctions and predicted that the Josephson critical current, I_c, would display damped oscillations as a function of the ferromag-

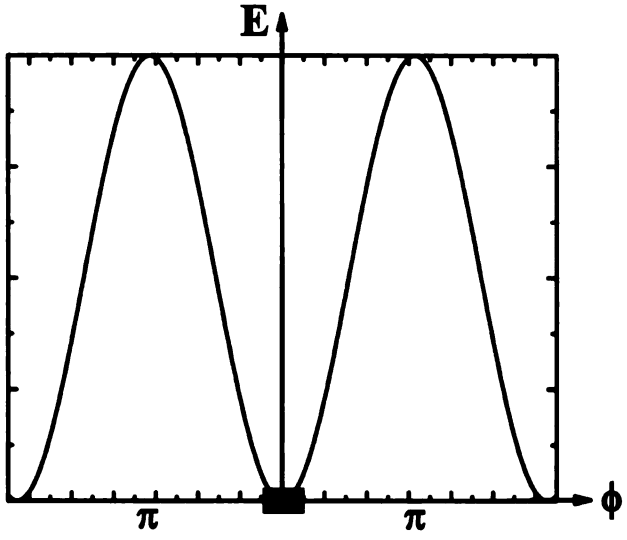

Figure 4.6: Josephson energy phase relation for a phase difference of 0 between the two superconductors. The square indicates the ground state

netic layer thickness, where the vanishing of the critical current signals the transition from the 0 state to the π state as shown in Figure 4.8.

4.3 Previous studies of the π junctions

Of crucial importance to experimentally observe the predicted oscillations of the critical current as a function of the ferromagnetic material thickness [31], is the choice of a proper ferromagnetic material for the barrier in SFS junction. The most common elemental ferromagnets are Fe, Ni, Co, and Gd. They have large exchange energies and hence very short values of the coherence length ξ_F, of the order of 1 nm, which makes it very difficult, and experimentally challenging to detect the oscillations at this length scale. The use of weak ferromagnets, e.g. a pure ferromagnet diluted with a diamagnetic or a paramagnetic metal with low exchange energy allows Josephson coupling through thicker ferromagnetic layers. Ryazanov and coworkers [32, 33] were the first to observe the $0 - \pi$ transition in SFS Josephson junctions. For the F-layer

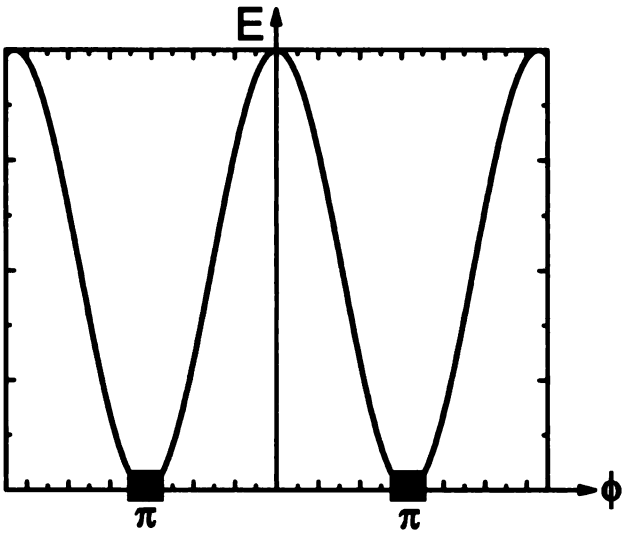

Figure 4.7: Josephson energy phase relation for a phase difference of π between the two superconductors. Squares indicate the ground state.

they used the weak ferromagnetic alloy, $Cu_{1-x}Ni_x$, with x about 0.5 and Curie temperature, T_c in the range $20 - 150K$. Figure 4.9 clearly shows the critical current oscillating between $0 - \pi$ states as a function of F-layer thickness. The use of the weak ferromagnetic $Cu_{1-x}Ni_x$ alloy with low Curie temperature allows one to prepare homogeneous and continuous interlayers with a thickness close to the coherence length ξ_F which made possible flowing of supercurrents through ferromagnetic layers as thick as 20-30 nm. Others studied SFS Josephson junctions using pure ferromagnets. For example, Robinson et al. [34] studied SFS Josephson junctions using strong ferromagnets, Ni, Co, Fe, Py ($Ni_{80}Fe_{20}$), and their data showed the oscillatory behavior of the Josephson critical current Ic as function of F-layer thickness, which is a clear manifestation of the transitions between the between $0 - \pi$ states. Figure 4.10 shows clear oscillatory critical current as a function of F-layer thickness for Josephson junctions containing Co.

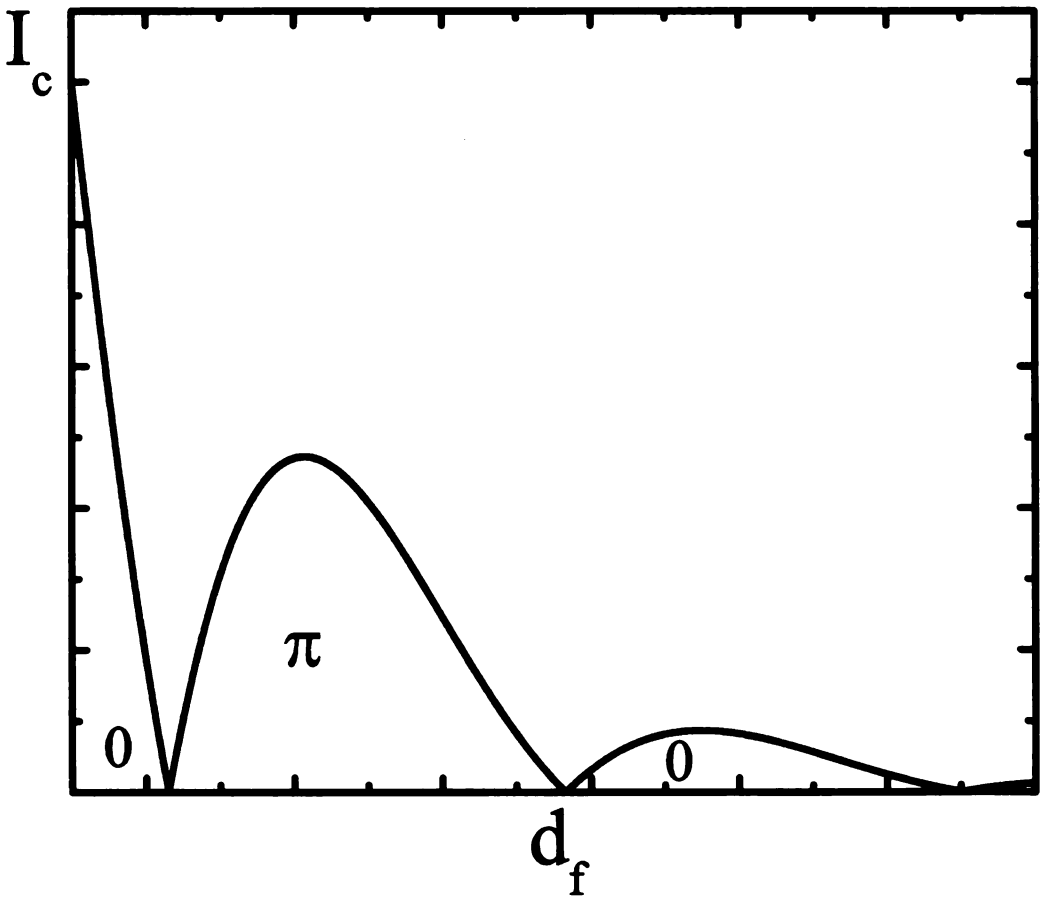

Figure 4.8: Critical current of SFS junctions as a function of the ferromagnetic layer thickness, d_f as predicted by [31].

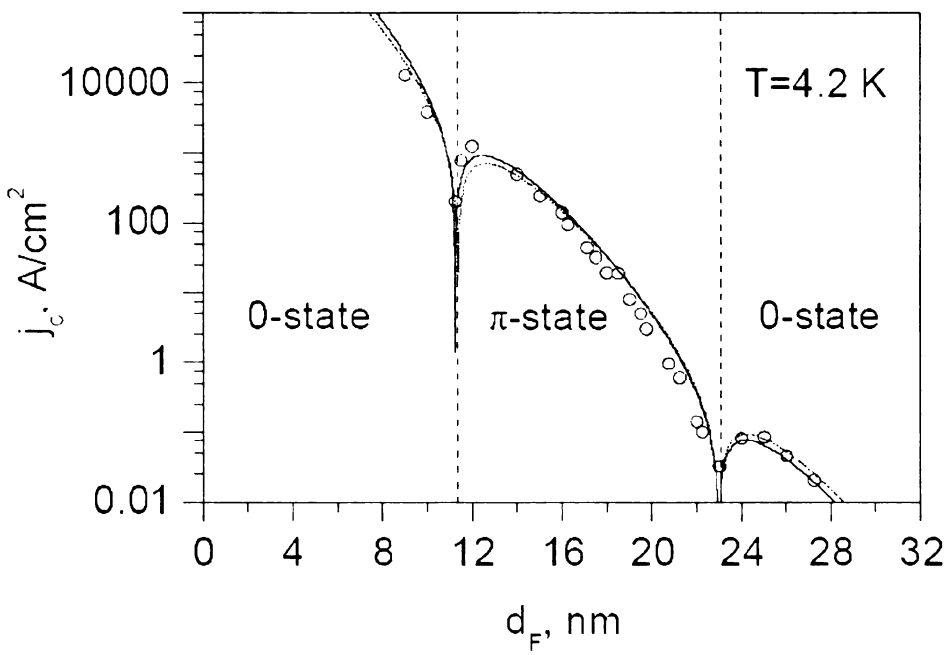

Figure 4.9: Oscillations of critical current density J_c as a function of CuNi thickness as measured by [33].

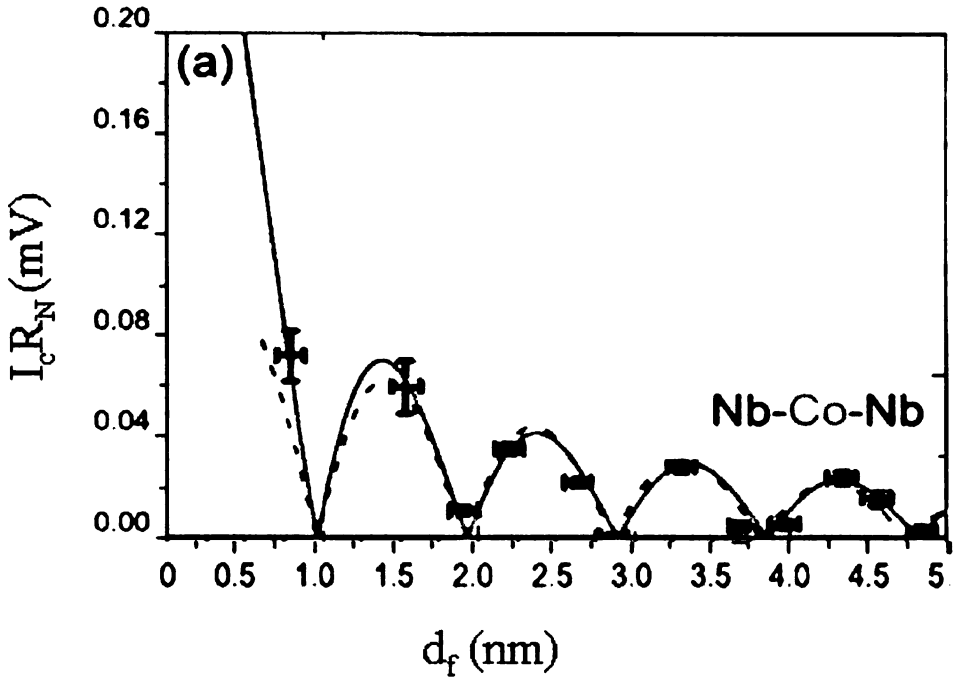

Figure 4.10: Oscillatory dependence of the product of the critical current and the normal resistance $I_C R_N$ as a function of d_{Co} as measured by [34].

4.4 Long range proximity effect

As shown in the previous section, the penetration length of superconducting correlations into ferromagnets is very short, in the order of a few nm. This is because the exchange field tries to align the spins of Cooper pairs in one direction (the direction of the magnetization), so superconducting correlations die very fast in the ferromagnet. This effect has been studied extensively and it was not the main incentive for our study. Instead our incentive is to find a new exotic behavior of these SFS Josephson junctions that appears if there is some sort of magnetic inhomogeneity in the system as will be explained in detail in the next section.

4.4.1 Long Range Triplet correlations in conventional superconductors, LRTC

One fascinating aspect of the proximity effect is the possibility of generating a new type of superconducting pairing state. The original BCS theory of superconductivity leads to a conventional s-wave pairing between electrons with opposite spin orientations, and for several decades it was the only type of superconductivity observed experimentally (for superconductors with critical temperatures below 20 K). However, high T_c superconductors show d-wave symmetry or a mixture of s-wave and d-wave components of the order parameter. Both the s-wave and d-wave types of symmetries of the order parameter imply singlet pairing, which means that the total spin of the Cooper pair is zero. Moreover, there are some superconductors that have intrinsic spin-triplet (p-wave) pairing such as Sr_2RuO_4. If the Cooper pair has equal spin triplet correlations ($\uparrow\uparrow$) or ($\downarrow\downarrow$) then it will be much more at home in the ferromagnet and so it will survive longer in the F-layer, of the order of the coherence length in the normal metal ξ_N. Odd-frequency superconducting pairing state, characterized by pair amplitude which is an odd function of Matsubara frequency, was first pro-

posed by Berezinskii [35] as a possible mechanism of superfluidity in He^3. Table 4.4.1 summarizes different types of symmetries. In 2001 Bergeret et al. [36, 37, 38, 40], and [39] predicted that under certain conditions, spin-triplet correlations similar to those suggested by Berezinskii, but s-wave and odd in frequency, might be induced in multilayered SF structures with conventional spin-singlet superconductors. This state has the following main properties:

1. It contains all the triplet components. Triplet correlations are classified according to their projection on the spin quantization axis. Since the spin of one electron can have two possible orientations ($\uparrow$ *or* $\downarrow$), then the number of possible configurations for a two electron system is four: the Singlet with total spin zero ($S = 0 = \frac{1}{\sqrt{2}}(|\uparrow\downarrow\rangle - |\downarrow\uparrow\rangle)$), and three triplets ($S = 1$) with projections of the total spin (sometimes given the index S_z), $m = 0, \pm 1$. The $m = 0$ triplet pairs always exist in S/F systems. They are suppressed in the ferromagnetic layer over the short length scale (in the dirty limit), $\xi_F^{Singlet} = \sqrt{\frac{\hbar D}{2E_{ex}}}$ just as the singlet pairs. But the $m = \pm 1$ pairs are not sensitive to the presence of an exchange field as pairing occurs in the same spin band. As a result they can penetrate into the F-layer on a length scale much larger than that of singlet Cooper pairs, of the order the normal metal coherence length (in the dirty limit) $\xi_F^{Triplet} = \sqrt{\frac{\hbar D}{2\pi k_B T}}$. They are known as Long Range Triplet Correlations (LRTC).

2. It has s-wave symmetry. According to the Pauli exclusion principle, no two identical electrons can occupy the same state at the same time, or in other words, the two electrons wavefunction $\Psi(\vec{r_1}, \vec{r_2})$ must be antisymetric under the exchange of the particles positions $\vec{r_1}$ and $\vec{r_2}$. The wavefunction is composed of a spin part and orbital angular momentum part. Since (in our case) it has s-wave symmetry, then the pair correlation function is even in momentum, $l = 0$, so the

	$S=0$	$S=1$
$L=0$	BCS	
$L=1$		Sr_2RuO_4
$L=2$	$High-T_c$	

Table 4.1: Symmetry classification of superconductor. Normally the blank boxes are not allowed, but they become available if pair correlations are odd in time (or frequency).

triplet component is symmetric under exchange both in spin and momentum space, which appears to be a violation of Pauli's exclusion principle. In order to satisfy Pauli's exclusion principle the pair correlation function should be odd under time reversal or in the frequency.

4.4.2 Mechanism for generation of the long-range triplet correlations

According to the theory [36, 40], the main condition needed for the generation of the long-range triplet correlations, LRTC is the existence of some sort of magnetic heterogeneity near the S/F interface.This could be achieved by one of the following:

1. Intrinsic inhomogeneity through the existence of domain walls in the ferromagnet [37, 38], or through spiral magnetic order in the ferromagnet [41, 42].

2. Extrinsic inhomogeneity. Engineering structures with two F-layer of non-collinear magnetizations, provided that the superconducting layer is not too thick, because the triplet component decays in the superconductor on length scale ξ_S, where ξ_S the superconducting coherence length [38].

3. Spin active region at the SF interface [43, 44].

To understand the mechanism by which these long range spin triplet correlations generated, consider a two-particles system. In the case of an s-wave superconductor

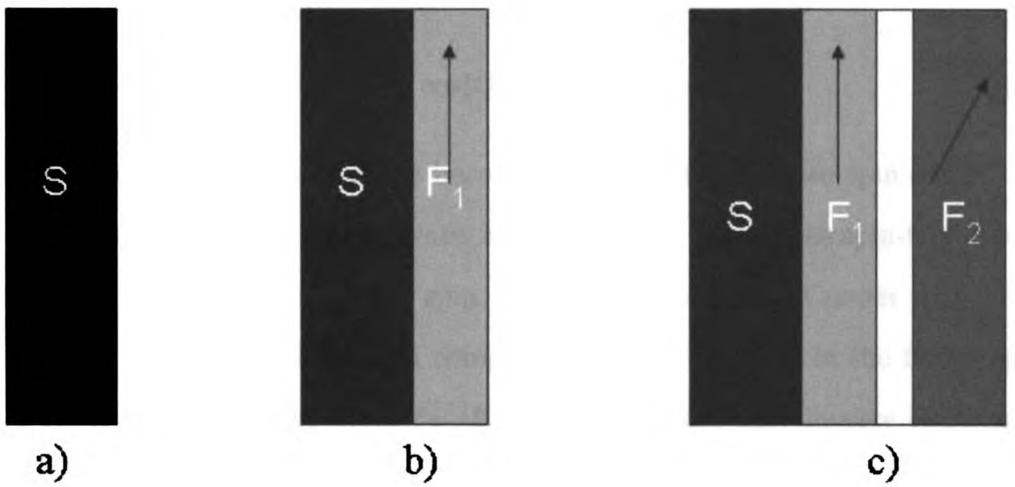

Figure 4.11: Mechanism for Spin triplet generation.

shown in Figure 4.11a, the spin part of the wavefunction is odd (singlet), and can be written as:

$$|\Psi\rangle = |0,0>= \frac{1}{\sqrt{2}}(\uparrow\downarrow\rangle - \downarrow\uparrow\rangle) \tag{4.7}$$

If we place a ferromagnet with homogeneous magnetization next to a superconductor as shown in figure 4.11b, then due to proximity effect, superconducting correlations are induced at the SF interface and penetrate into the F-layer. As the two electrons have opposite spins they must enter opposite spin bands with different Fermi wave vectors. As initially the electrons had Fermi wave vectors in opposite directions but equal magnitudes, this leads to a nonzero center of mass momentum, $Q = k_f^{\uparrow} - k_f^{\downarrow}$. If the spin up and down configurations are interchanged, then the Cooper pair obtains a center of mass of the opposite sign Q. This transforms Eq. (4.7) into:

$$|\Psi\rangle = \frac{1}{\sqrt{2}}(\uparrow\downarrow\rangle e^{iQx} - \downarrow\uparrow\rangle e^{-iQx}) \tag{4.8}$$

which can also be written as:

$$|\Psi\rangle = \frac{1}{\sqrt{2}}[(\uparrow\downarrow\rangle - \downarrow\uparrow\rangle)\cos(Qx) + i(\uparrow\downarrow\rangle + \downarrow\uparrow\rangle)\sin(Qx)] \tag{4.9}$$

or

$$|\Psi\rangle = |0,0\rangle_z \cos(Qx) + i|1,0\rangle_z \sin(Qx) \tag{4.10}$$

So the superconducting correlations become a superposition of two spin states. The first term is the usual spin-singlet state, and the second term is the spin-triplet component with zero projection of the spin magnetic moment of a Cooper pair on the z-axis, $S_z = 0$. However, both spin components decay very fast in the ferromagnet over a short distance of the order ξ_F (Eq. (4.4)) because they involve electrons in both Spin bands in the ferromagnet. To generate the triplet correlations of equal spin-pairing, $S_z = \pm 1$, one needs some sort of magnetic inhomogeneity, or noncollinear magnetization, as shown in figure 4.11c. It is the triplet component with zero spin magnetic moment projection which is responsible for the generation of the spin triplet with $S_z = \pm 1$. So under rotation of basis along the new direction θ, $|1,0\rangle_z$ component contains all 3 components $|1,1\rangle_\theta$, $|1,0\rangle_\theta$ and $|1,-1\rangle_\theta$:

$$|1,0\rangle_z \Longrightarrow \|1,1\rangle_\theta = |\uparrow\uparrow\rangle \tag{4.11}$$

and

$$|1,0\rangle_z \Longrightarrow \frac{1}{\sqrt{2}}(|\uparrow\downarrow\rangle + |\downarrow\uparrow\rangle) \tag{4.12}$$

and

$$|1,0\rangle_z \Longrightarrow \|1,-1\rangle_\theta = |\downarrow\downarrow\rangle \tag{4.13}$$

Eqs. (4.11) and (4.13) are the spin triplet components with non-zero projections $S_z = \pm 1$, and are independent of the exchange field and can penetrate the ferromagnet over a long distance of the order of ξ_N (Eq. (4.2)).

4.5 Signature of the long-range triplet correlations

Two signatures can demonstrate the existence of the Long Range triplet superconducting correlations (LRTC). The first is a measurement of the density of states (DOS) of a FSF structure similar to those performed by Kontos et al. in $Nb/Pd_{1-x}Ni_x$ bilayers [45] (kontos didn't have noncollinear magnetization). With the magnetization orientations of the different ferromagnets are noncollinear, triplet component will be generated. For distances in the F-layer larger than ξ_F, only the triplet component exists, and that leads to a variation in the DOS. By comparing the DOS when the magnetization of the two magnetic layers are collinear (no triplet component) and noncollinear (triplet exists), we can tell if the triplet component is induced or not. We have not yet pursued this approach. The approach we pursued was to fabricate and characterize SFS Josephson junctions containing an elemental strong ferromagnetic material like Co. The thickness of the F-layer was systematically increased from very thin, where the the spin singlet component is the dominant, to very thick samples where the spin triplet component (if it exists) dominates. A measurement of the ferromagnetic layer thickness dependence of the critical current, $I_c(d_F)$ over a broad range of d_F will provide a strong test of the theory. Figure 4.12 shows the expected behavior of the critical current of SFS Josephson junction as a function of F-layer thickness. At small F-layer thickness d_F, I_c oscillates (not shown) and decays rapidly over the short length scale ξ_F. At larger values of d_F, in the presence of some sort of magnetic inhomogeneity, the triplet component of the pair correlations takes over, and I_c decays over a much longer length scale, comparable to that of the normal metal, limited only by the temperature or by spin-flip and spin-orbit scattering. In the absence of magnetic inhomogeneity, the LRTC vanishes, and only the singlet supercurrent remains.

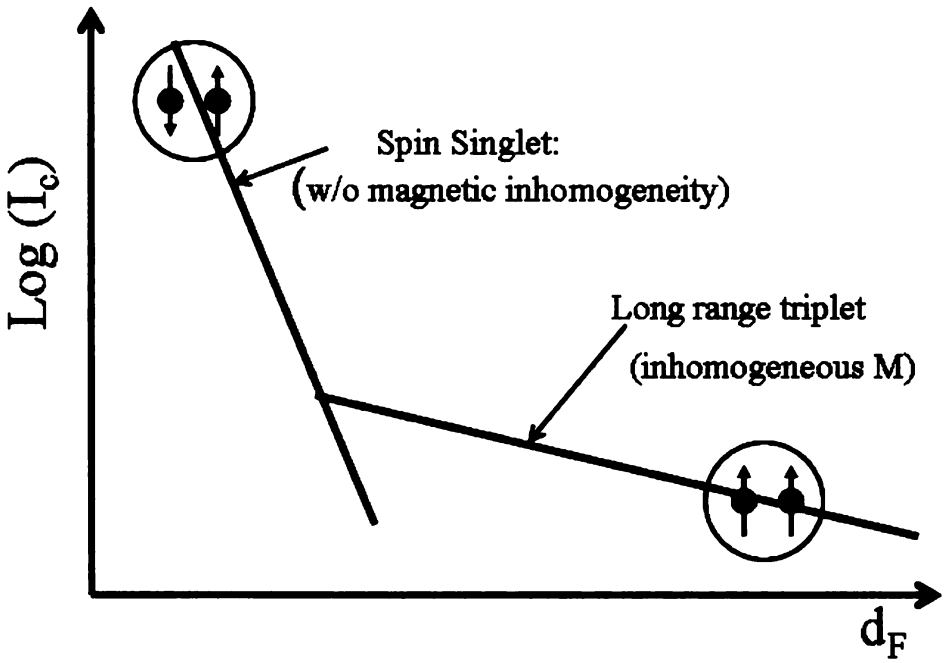

Figure 4.12: Penetration of the singlet (oscillations are not shown) and triplet components of the order parameter in the ferromagnet.

4.6 Previous studies of the long-range triplet correlations

Since elemental ferromagnetic materials like Co have large exchange energies, E_{ex}(Co) = 0.36 eV, then the corresponding coherence length is very short, in the order on 1 nm [34]. Any observation of the proximity effect in SF structures may be limited to very thin ferromagnetic layers. In the late 1990's, (a couple of years before the Bergeret [36] theory on LRTC), three groups observed substantial decrease in the resistance of SF hybrid systems consisting of micron sized ferromagnetic wires connected to superconducting electrodes when cooled below the T_c of the superconductor [46, 47, 48]). All three groups attributed their findings to an anomalously long range proximity effect, but there were not sufficient control experiments to rule out alternative explanations. And these papers appeared before the LRTC had been proposed. Then in

2006, two papers appeared in the literature, and the authors of both papers explicitly interpret their findings in terms of the LRTC. The first of the two was Klapwijk's group [49]. They used the lateral geometry for their SFS Josephson junctions with the half metal CrO_2 as the ferromagnet and NbTiN as the superconducting electrodes. Since CrO_2 is a half metal ferromagnet (fully spin polarized), the authors concluded that the current must be due to spin triplet correlations. But large sample to sample fluctuations in the critical current made it difficult to analyze the data. The other one was Petrashov's group [50]. They reported a phase-sensitive modulation of the resistance of a 300-nm long Ho wire (much longer the ξ_F) connected to two superconducting electrodes, and suggested that the observed long-range phase coherence must be due to spin-triplet correlations generated as a result of the spiral magnetization of the Ho wire.

Chapter 5

Fabrication and measurement

5.1 Introduction

In this chapter I discuss the experimental methods used in this work to fabricate, characterize, and measure our samples.

5.1.1 Fabrication

All samples were prepared and measured at MSU. Mainly three types of samples were prepared. The first type are Josephson junctions with the current flowing perpendicular to the plane (CPP). The second type are also samples with the current flowing perpendicular to the plane used in the Giant Magneto Resistance GMR measurements, and the third type are the samples used used to measure the magnetic behavior of our Josephson junctions (M vs H) using SQUID magnetometer. Details of each type will be explained later. The fabrication process of the Josephson junctions consists of:

1. Substrate cleaning.

2. Sputtering the multilayers.

3. Photolithographically pattern the samples.

4. Ion milling to create the SFS junctions.

5. Depositing the SiO_X insulating layer.

6. Lift off.

7. Depositing the top Nb leads.

5.1.2 Substrate cleaning

Substrate choice is critical to the production of good quality junctions. The substrate should be a good insulator to avoid shorting out devices. It should be extremely flat and have good adhesion properties, also the cost is another important factor. Silicon wafers are used as substrates due to their good properties and price. The whole sample fabrication process was carried out in the clean room. The only time the substrates were exposed to the outside (before being ready for measurement) was when they were diced. To do that the whole wafer was coated with a thick enough layer of photoresist, then baked for a minute on a hot plate inside the clean room, then taken out for dicing into pieces 0.5 inch by 0.5 inch in size using a MicroAutomation 1006 Dicing Saw. This is very important in order to produce dust free and unscratched substrates. Once the wafer is diced, it is then taken back to the clean room for cleaning. Every substrate was first submerged in a beaker of remover-AZ Kwik Strip- to remove the photoresist. All samples were then rinsed in water. After that, substrates were submerged in acetone which was agitated in an ultrasonic bath for 10 minutes. They were then placed in beakers of isopropyl alcohol (IPA) in the ultrasonic bath for another 10 minutes. Finally substrates were submerged in dionized water in the ultrasonic bath for 10 minutes. They were then blown dry using compressed dry Nitrogen gas, and visually checked using an Olympus BX60 optical microscope at a

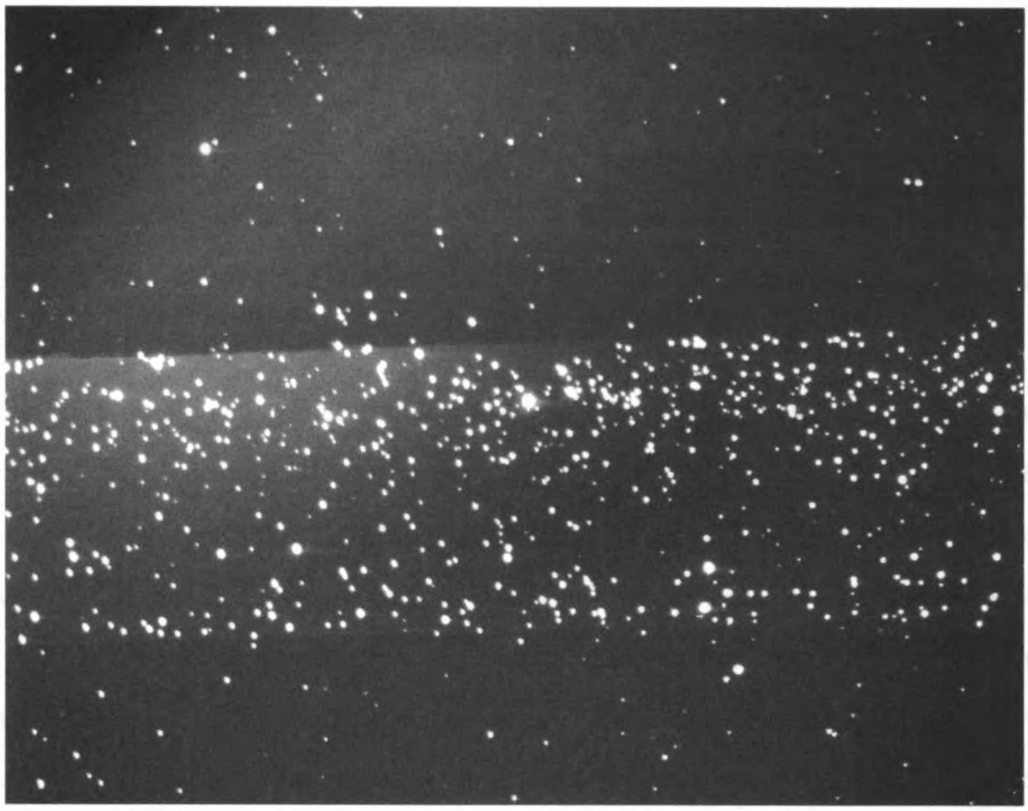

Figure 5.1: Sample under the optical microscope (dark field mode) showing dust particles that may lead to pinholes.

magnification of 20-100X for drying marks or traces of dirt especially in the central area, where the multilayer would be deposited. Samples with defects were cleaned in acetone by rubbing the surface with a Q-tip and inspected again under the optical microscope. If there is a non removable defect, then the substrate is discarded. This procedure was found to be highly effective in the production of very clean, regular substrates. Figure 5.1 shows a sample cleaned outside of the clean room.

5.1.3 Sputtering the multilayer

All junctions used in this project were grown using a computer controlled dc magnetron sputtering system under high vacuum conditions in order to minimize interaction with residual air molecules. This system allow deposition from up to 6 different

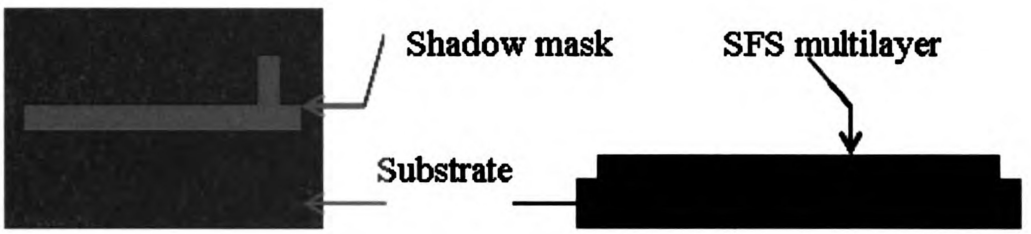

Figure 5.2: Top view of the shadow mask used in sputtering the SFS samples. Side view of the SFS multilayer. Dimensions are not to scale.

targets in a single run. Target materials are high purity metals or alloys, mainly purchased from commercial companies. Sputtering is a physical vapor deposition technique in which a potential difference is applied across two electrodes separated by a small distance in the presence of Argon gas. With Ar forming a plasma of ionized gas, the Ar^+ ions are then accelerated to the surface of one electrode, where they transfer kinetic energy, knocking atoms off the surface of the target. In magnetron sputtering a series of magnets located near one electrode causes each electron to ionize more gas particles and as a result more target atoms are knocked off. Most of the power delivered during sputtering is consumed in heating the target material, which in turn needs to be constantly water cooled. Films were deposited using shadow masks as shown in Figure 5.2. In a single run we can make up to 16 samples of the Josephson junction type or 8 GMR samples. All samples were fit snugly into the sample holders with the shadow masks facing down which in turn are attached to the sample positioning and masking apparatus (SPAMA) plate. In the sputtering chamber we have four triode guns, and two dc-magnetron guns situated in the bottom of the chamber. Above each big gun is a set of 2 chimneys, one with a hole on top for material deposition, and the other one without a hole to block the deposition of any material. All chimneys were wrapped in Al foil as shown in Figure 5.3. The Al foil should be changed from run to run to prevent contamination . Once the chimneys are placed on top of the guns, the substrates are loaded into the SPAMA plate (outside the cleanroom), the system is closed, and pumped down using a mechanical

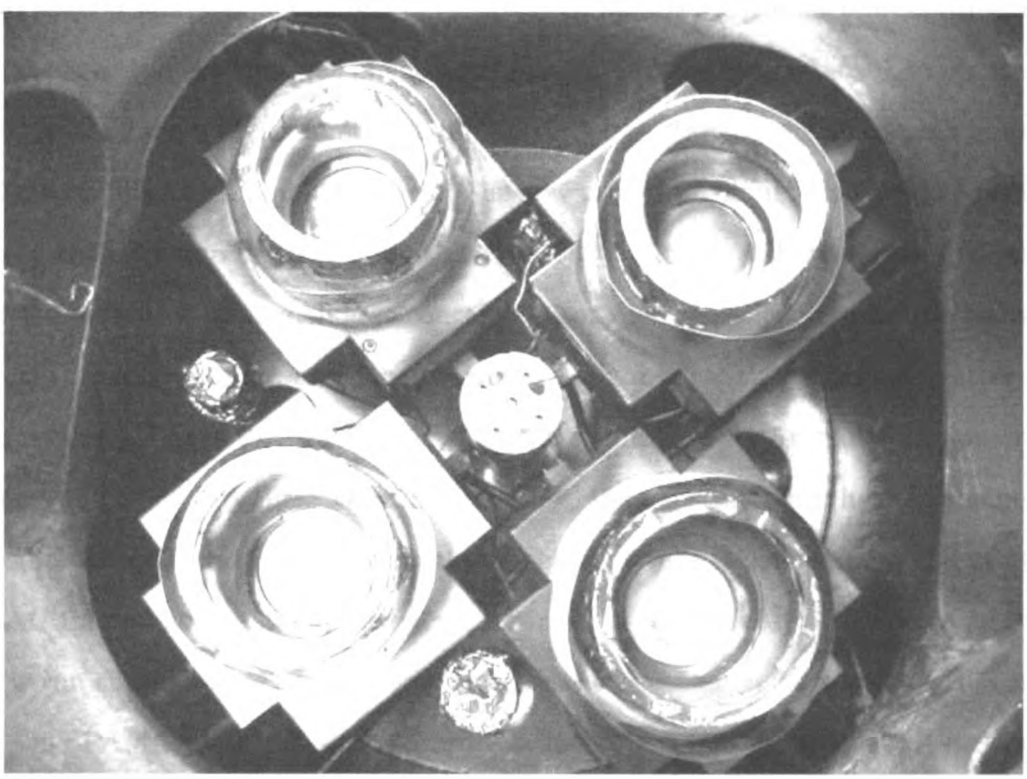

Figure 5.3: Top view of 4 main triode sputter sources as well as two smaller magnetron sources.

pump down to 2×10^{-2}Torr with the gate valve to the cryopump close. Once the pressure is 2×10^{-2} Torr the gate valve to the mechanical pump is closed and the gate valve to the cryopump is opened to further pump down the chamber. We pump down the chamber for about 15 minutes until the pressure reaches 8×10^{-6}Torr, then we test the guns to make sure they are working fine. If the guns are OK, we open the gate valve 13 turns or 5×10^{-6}Torr, then we turn on the heater and bake the chamber for at least 8 hours at about 60 ^0C. Upon cooling down to room temperature, the gate valve to the cryopump is opened completely, and the system is left to pump for 24 hours reaching a pressure of 3×10^{-8}Torr. Before starting the sputtering guns, a cold trap is filled with liquid nitrogen. The flow rate of the liquid nitrogen is adjusted to keep the cold trap temperature at about -190 ^0C. It takes about an hour to reach that temperature. This cooling encourages absorption of molecules into the walls of the cold trap, thereby lowering the pressure to about 2.5×10^{-8}. During sputtering, high pressure Ar gas (99.999 %) back fills the chamber. The Ar sputtering pressure is kept at 2.5 ± 0.3 mTorr. During sputtering, the substrates are held at temperatures between -30 and 30 ^0C. To do that a capillary tube is connected with both the SPAMA plate and the liquid nitrogen cold trap. A pressurized nitrogen gas at 1000 PSI is run through the capillary tube to enable heat exchange between the cold trap and the SPAMA plate. The temperature is monitored by a thermocouple mechanically attached to the back of one of the samples on the SPAMA plate. After cooling the system for about an hour, and the temperature of the substrates has reached -30 ^0C, we turn on all the sputtering guns, and let them equilibrate for about 10 minutes. The voltages and currents for each target material are kept fixed from run to run so that the deposition rates are similar for samples made in different runs. Before depositing any materials on the substrates, we make a dummy run to clean the targets. A shutter is placed between the targets and the sample holder, and has 2 positions: open to allow material from the target to reach the substrate, or closed

to prevent it from reaching the substrate. In this dummy run, target materials are deposited on the shutter without exposing the substrates. Before depositing the real samples, the deposition rate D.R(Å/s) of each target material is measured using a quartz crystal film thickness monitor (FTM). The SPAMA plate has 2 FTM's for this purpose. The FTM reading along with the desired thickness d(Å) of the target material to be deposited is then used to calculate the time needed for sputtering of that material according to

$$t(s) = \frac{d}{(D.R)} \tag{5.1}$$

These rates are measured just before making every sample. The values for target voltages, currents and deposition rates are listed in table 5.1. After measuring the

Material	Voltage (V)	Current (A)	Deposition Rate $(\AA/s)$
Nb	600	0.6	4.7
Co	550	0.5	5.3
Cu	240	0.45	4.3
Au	150	0.5	4.7
CuNi	300	0.43	4.7
Ru	-	-	0.8

Table 5.1: Sputtering materials voltages, currents and deposition rates.

deposition rates, the sample to be made is exposed by rotating the circular stainless steel mask that is attached to the base of the sample holder to the open position using a vacuum compatible wobble stick. The alignment of the sample with the opening on the rotating mask is checked visually through the view window of the sputtering chamber as shown in Figure 5.4. If the alignment is OK, then the SPAMA plate will rotate bringing the assigned sample over the gun containing the material to be sputtered, and when in place the system of chimneys rotates to allow deposition for a specified time. When the time is reached, the chimney system rotates back to the close position and the SPAMA plate rotates so that the sample is on top of the next

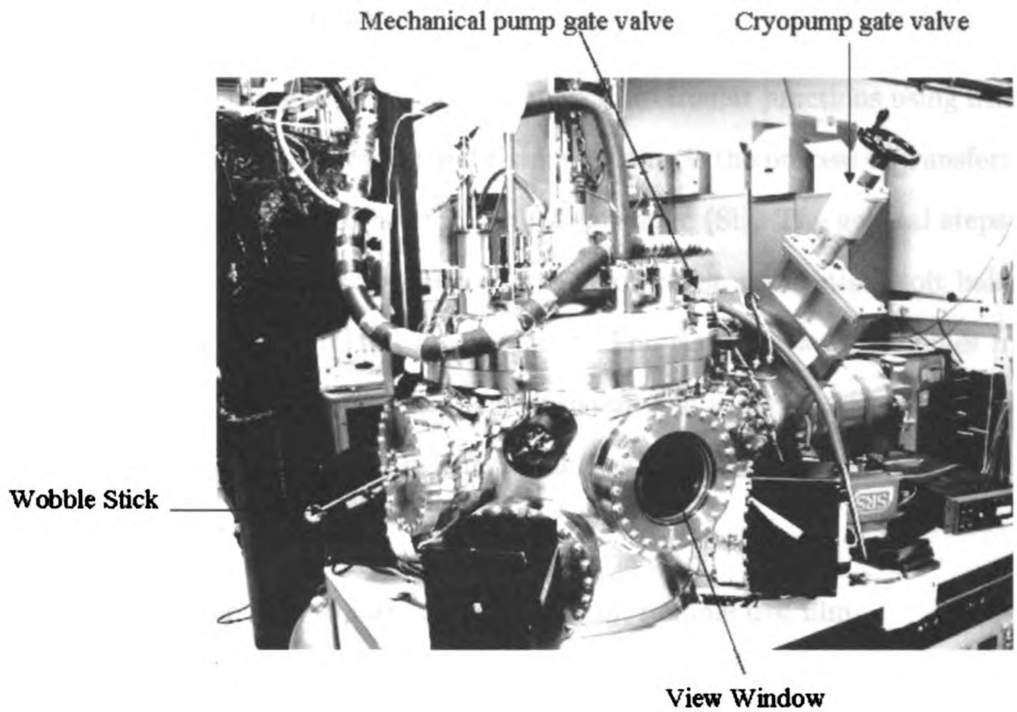

Figure 5.4: Sputtering chamber.

sputtering gun. This process is repeated until the entire sequence of materials to be deposited is finished. Finally the sample holder is brought to the wobble stick position so I can rotate the shutter back to the close position to prevent further deposition on the sample. All of this is controlled by the computer. Once we finish making all the samples, the gate valve to the croypump is closed and the system is left to warm up to room temperature either overnight, or by filling the chamber with Nitrogen gas up to 350 Torr and heating the system for about 45 minutes. Then the system is opened, the targets are removed and put back in their cabinet, and the samples are are detached from the SPAMA plate, put in a plastic bag and taken to the cleanroom for processing.

5.1.4 Photolithography

The next step is patterning the multilayer to make the circular junctions using lithography. Lithography, literally meaning light-stone writing is the process of transferring geometric shapes on a mask to the surface of a substrate (Si). The general steps involved in the photolithography process include: photoresist application, soft baking, mask alignment, UV exposure and development. The word photoresist comes from the combination of photosensitive and acid resistant, i.e a photoresist can be photolithographically patterned and can survive acid etch. A photoresist must exhibit certain characteristics:

1. coating: must be able to form a thin, uniform, pinhole free film
2. adhesion: adheres to the underlaying substrate and doesn't lift off during subsequent processing.
3. sensitivity: must be sensitive to the wavelength of radiation used for exposure.
4. developing: must have a significant difference in developing rate between the exposed and unexposed areas without pattern distortion.
5. process resistance: must withstand ion milling, and wet etchant.
6. easy removal: must be removable after processing is done.
7. stability and safety: must be stable enough to be stored for reasonable periods of time, and must be safe and present no health hazard.

Photoresists are generally composed of three components:

1. Base material (polymer resin): the backbone of the photoresist.
2. Photoactive compound (PAC): it is the part of the photoresist that undergoes a chemical reaction when exposed to light.

3. Solvent: it controls the mechanical properties of the photoresist. It keeps it in liquid form until after coating.

The main property of photoresists is that they change chemically when exposed to UV light. Different photoresists react differently, but generally speaking, they become either less or more acidic. The more acidic the resist is, the easier to remove with an alkali solution (such as developer). Because of this property, photoresists are divided into three types.

1. Positive photoresists: exposure to the UV light changes the chemical structure of the exposed areas making them soluble in the developer, while the unexposed areas are insoluble.

2. Negative photoresists: behave opposite to the positive photoresist, in which the unexposed areas are soluble in the developer, while the exposed ares are insoluble. Figure 5.5 is a cartoon showing positive and negative photoresists.

3. Image reversal photoresists: can either be processed in positive or negative mode, and will be discussed in detail later.

In this thesis, was used image reversal lithography, in which a positive photoresist (AZ 5214E) is used to produce a negative tone image of the mask. A mask is a glass plate that has a patterned chrome layer on one side. Image reversal can be thought of as three processes:

1) Spin coating the substrate: a few drops of the photoresist are dispersed onto the center of the substrate, then the substrate is spun at a high speed to produce a uniform photoresist film. The fast spinning causes the photoresist to be spread across the surface of the substrate with excess being thrown off. The thickness of the photoresist (T_{PR}) after spin coating is given by:

$$T_{PR} \propto \frac{1}{\sqrt{V}} \tag{5.2}$$

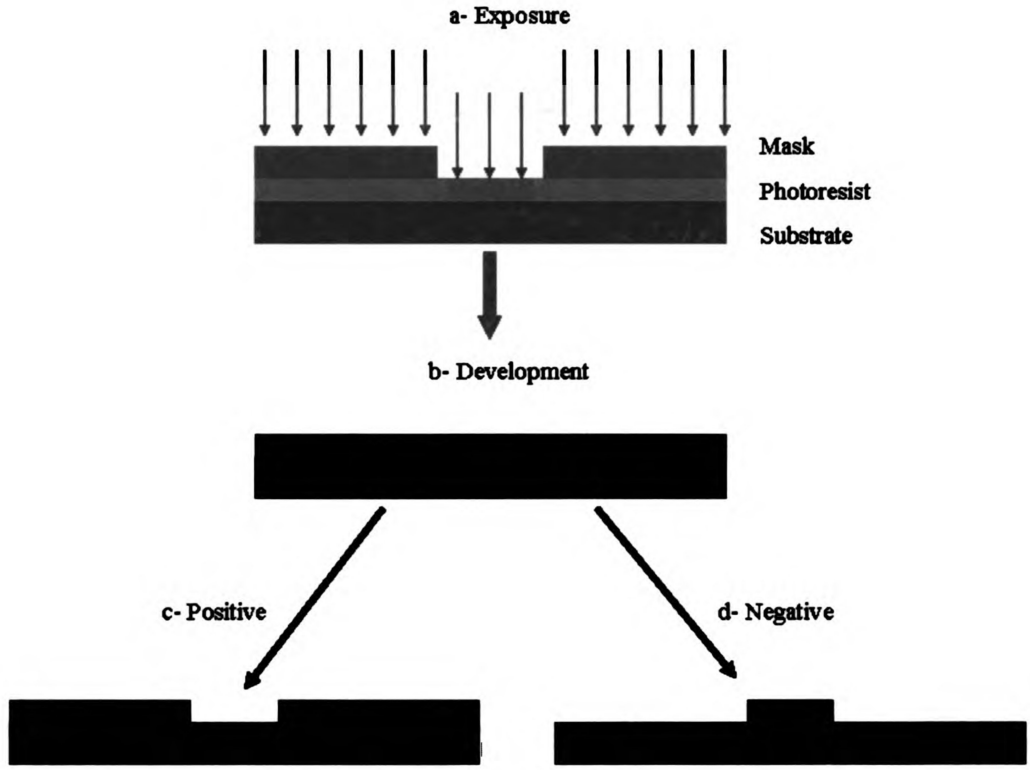

Figure 5.5: Cartoon showing positive and negative photoresists. (a) Exposure to UV light causes a chemical change in the exposed region. (b) Development. (c) Positive photoresist: the exposed region is removed by the developer. (d) Negative photoresist: the exposed region is not removed by the developer.

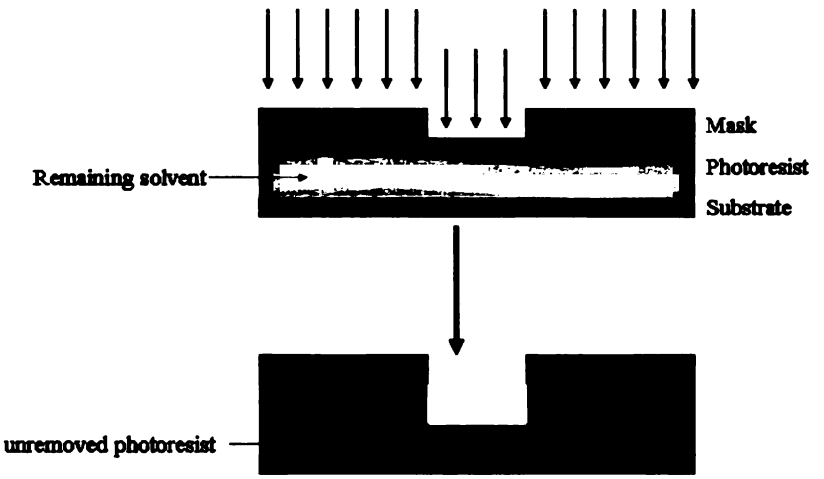

Figure 5.6: Under-baked photoresist

where V is the speed of the spin coater in RPM. A speed of 4000 RPM for 45 seconds gives an approximately 1.4 μ m thick uniform layer. The photoresist coated substrate is then soft-baked (pre-baked) to remove the solvent component of the photoresist and make it sensitive to the UV light. Over-baking the substrate will increase the sensitivity to UV light, and in severe cases may destroy the PAC and reduce the solubility of the photoresist in the developer. On the other hand, under-baking will prevent UV light from reaching the PAC due to excess solvent remaining in the photoresist, see Figure 5.6. Our samples were baked on a hot plate at 110 ^0C for 50 seconds. Once the substrate has been coated with photoresist and pre-baked, then it is ready for UV light exposure. We expose the substrate to UV light for 3 seconds through a dark mask , i.e dark everywhere except at the feature positions. The areas that are exposed to the UV light will undergo a chemical reaction. Upon exposure, the exposed areas are soluble in the developer while the unexposed are not. It is important to expose the substrate for the right amount of time. If the exposure time is too short, the chemical reaction will be incomplete, and the photoresist will not become completely soluble. This is called under-exposure, and the photoresist will not or will partially develop. The most common result of this is that the corners

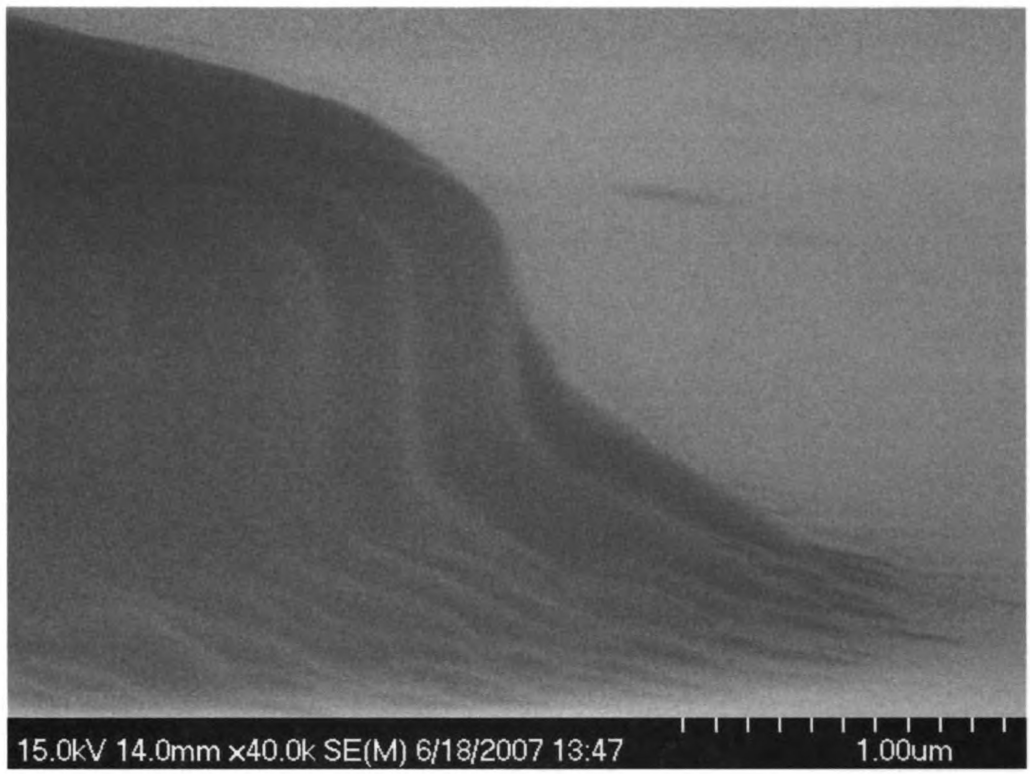

Figure 5.7: Over-exposed photoresist

and edges of the feature which receive less energy from the UV light than the central part, will not be removed when immersed in the developer, and rounded corners will be seen in the under exposed regions, and there will be areas of the photoresist remaining after development. On the other hand, if the exposure times is too long, the chemical reaction can spread outside of the limits of the exposed region. This is called over-exposure, and may result in exposed areas under the mask where it should be protected from UV light. This can be seen as ragged edges in the features as shown in Figure 5.7.

2) The substrate with partially exposed photoresist is subjected to a post exposure bake. The post exposure bake, sometimes called Image reversal bake (IM) is the most critical step in image reversal photolithography, once optimized it must be kept constant within $\pm$ 1 ^0C to maintain a consistent process. This image reversal baking

Figure 5.8: Sample over baked (115 ^0C) after exposure.

initiates cross linking of the polymer resin in the exposed areas of the photoresist making them insoluble in the developer solution. In our current research an image reversal baking temperature of 110 ^0C gave the best results. Above 115 ^0C, the unexposed areas of the photoresist start to cross link as well, as shown in Figure 5.8.

3) After the image reversal bake, the entire substrate is flood exposed without a mask for about 100 s. This causes all the previously unexposed areas of the photoresist to undergo a chemical reaction that make them soluble in the developer, while the areas that were originally exposed become insoluble. This creates a reverse image of the original mask with negative wall profile known as undercut that is ideally suited for lift off. Figure 5.9 shows how image reversal process works. Table 5.2 summarizes the parameters used in this work for image reversal lithography.

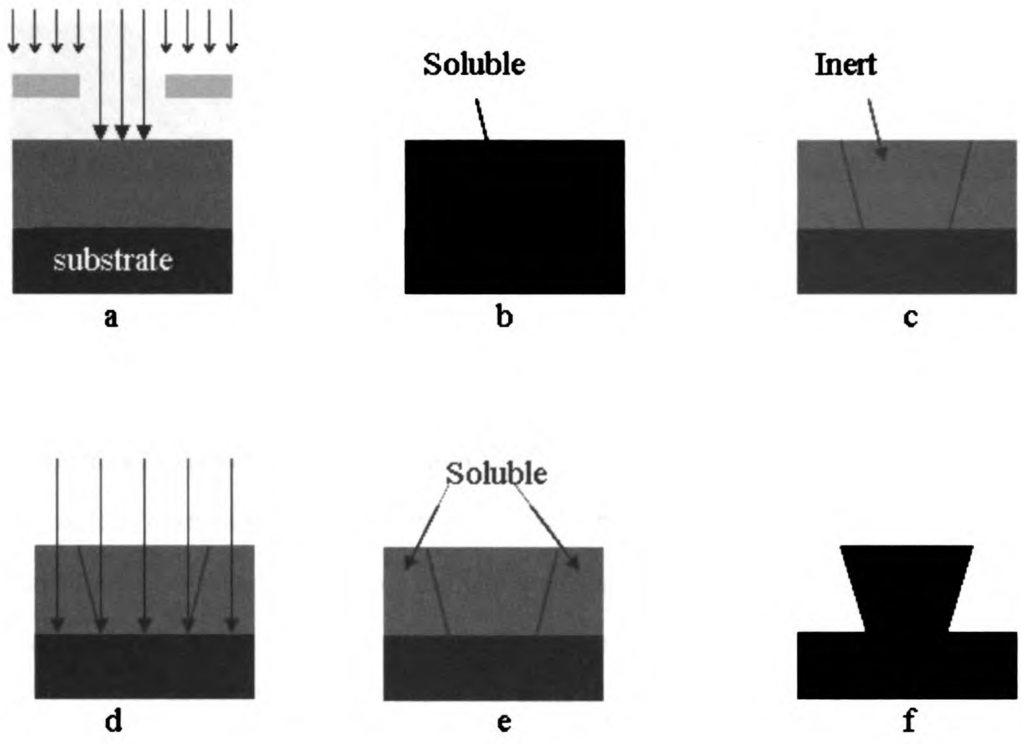

Figure 5.9: Cartoon showing the basic steps Image reversal lithography. a: Exposure to UV light using a dark field mask, b: Exposed areas are soluble in the developer., c: Image reversal bake cross-links the exposed areas, while the unexposed areas remain photoactive., d: Flood exposure without mask., e: Flood exposure makes areas unexposed in a) soluble., f: After development,the areas exposed in step a remain with the needed undercut.

Spin Coating	AZ 5214E	4000 rpm	45 sec
Pre-Bake	Hot plate	110°C	50 sec
Expose	UV		3 sec
Image reversal bake	Hot plate	110°C	60 sec
Flood exposure (no mask)	UV		100 sec
Develop	AZ 300 MIF		30 sec
Lift-Off	AZ Kwik Strip	90°C	10-13 min

Table 5.2: Parameters used for image reversal lithography.

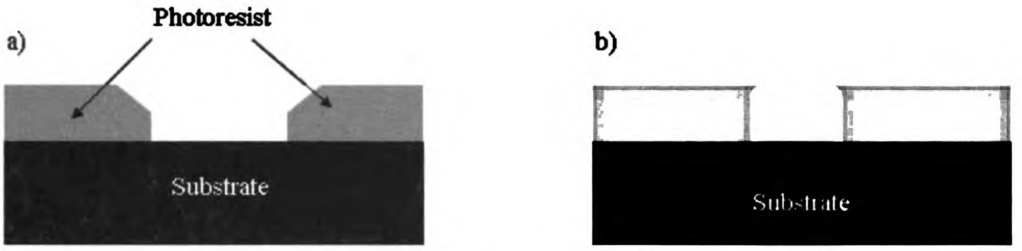

Figure 5.10: Development profile. a) Over development. b) Under development

Once flood exposed, the substrate is then immersed in a developer solution. Developer solutions are typically aqueous and will dissolve away areas of the photoresist that were flood exposed to light. When developing the substrates, it is very important to use the correct developing time. The effects of the developer are pretty much the same as the exposure. Developing the substrates for too short period of time – under-developing –, may leave photoresist in the exposed region. On the other hand, if the substrates are developed for too long, then the less acidic parts will be partially dissolved, as shown in Figure 5.10. In our case, we developed for 30 s although we see the photoresist disappeared after about 20 s, then we checked the substrates under the optical microscope to make sure the photoresist has been removed everywhere except where the features are. It was challenging and time consuming to optimize the image reversal process, as we have many factors, but once optimized and tested; it gave us good and reproducible results as shown in Figure 5.11b.

5.1.5 Ion Milling

To successfully transfer the patterns using photolithography, it is important to have an undercut, which is the profile of the photoresist after development with negative slope. The undercut is good for lift off. The negative slope of the photoresist shadows the corners of the features on the substrate from deposition. It prevents tearing when the photoresist is removed and enhances remover penetration. The photoresist can be

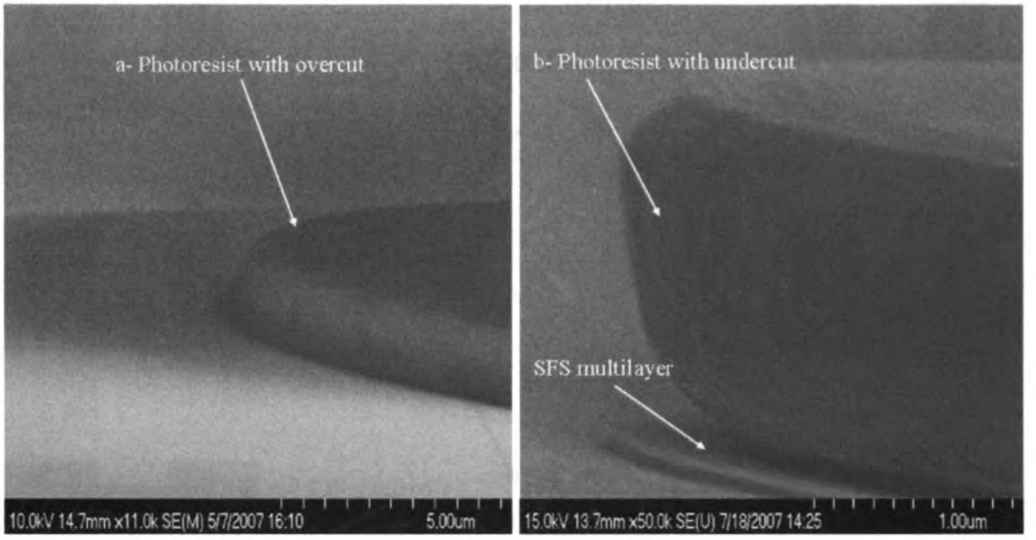

Figure 5.11: a: Pillar covered with photoresist, but with overcut (bad!!), b: Pillar covered with photoresist with undercut (after ion milling).

used as a temporary mask when etching an underlying layer, so that the pattern may be transferred to the underlying layer as shown in Figure 5.12a, this process is known as a subtractive process. However, photoresist may also be used as a sacrificial layer for patterning material deposited after lithography. The photoresist is subsequently removed, and the material deposited on the photoresist is lifted off. This is shown in Figure 5.12b, this process is known as an additive process. In this research we used both subtractive (ion milling) and additive (SiO deposition processes). The ion milling system was used to pattern the circular junctions. Ion milling is a process used to remove the material that is not protected by the photoresist. The disadvantages of ion milling are the lack of selectivity of materials (so the rate of ion milling should be well calibrated), and the redeposition or back-sputtering of the milled material on the sides of the junctions which produces shorts in the junctions. To overcome the problem of back-sputtering, we ion mill through the top Nb layer and stop in the middle of the ferromagnetic layer. We didn't ion mill the bottom Nb layer to prevent back sputtering of the ion milled Nb layer into the junctions. Before loading the samples in the ion milling chamber, they were placed in sample holders. These

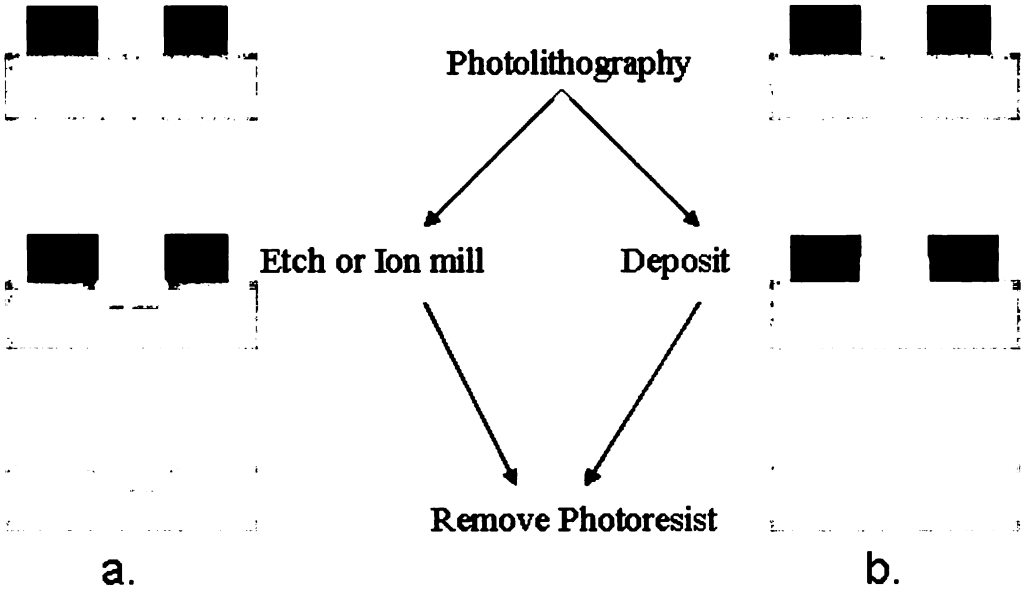

Figure 5.12: a: Subtractive process, b: Additive process.

holders have copper heat sinks so that the temperature of the samples doesn't go too high during ion milling, as overheating of the samples may burn the photoresist and make it hard to dissolve in the remover. Also the sample holders have magnetic disks to help load the samples into the milling chamber through a load lock equipped with a magnetic arm. Base pressure for ion milling was $\leq 6 \times 10^{-8}$Torr. The Ar pressure during ion milling is 2×10^{-4}Torr. The ion milling rates for different materials were calibrated with respect to the ion milling rate of gold (Au), and are given by:

$$D.R(Nb) = 0.149 \times D.R(Au) \tag{5.3}$$

$$D.R(Cu) = 0.67 \times D.R(Au) \tag{5.4}$$

$$D.R(CuNi) = 0.67 \times D.R(Au) \tag{5.5}$$

$$D.R(Co) = 0.274 \times D.R(Au) \tag{5.6}$$

5.1.6 Insulation and Lift off

After the multilayers are ion milled and the pillar shapes are created, but before breaking the vacuum, an insulating layer of SiO is evaporated onto the substrates. The SiO is evaporated while the sample is rotating at 200-300 RPM, to minimize the chance of pinholes through the 160-nm thick SiO layer. By evaporating SiO, the areas of the substrate that are not covered with the photoresist will be covered by SiO, while the covered areas, pillars in our case, will be protected, and the SiO will be deposited on top of the photoresist and will be removed through lift off. This creates a layer of insulation between the base (area on the substrate with no photoresist) and the top Nb layer to be deposited at the end. After evaporating the insulating layer of SiO, the samples are taken out from the ion milling chamber for lift off in the clean room. Lift off is the process of removing the photoresist. Another challenge we had was lift off. First we tried lift off in hot acetone, but the results were very poor, see Figure 5.13 a. It could be a heating problem, so we contacted the company that sells the photoresist we used (AZ 5214E) and told them about our problem. They suggested using a special kind of remover known as AZ Kwik Strip Remover that can remove this photoresist even if heated up to 70 ^0C. Just heat the remover to 90 ^0C for some time, then dip the sample in the hot remover and agitate it in an ultrasonic cleaner for 10-12 min's. The results were improved considerably as shown in Figure 5.13 b.

5.1.7 Top Nb leads

Before depositing the top Nb contacts, the samples were taken again to the ion milling chamber to slightly ion mill the protective Au layer and remove any residual photoresist. The Au layer becomes superconducting by proximity as it becomes sandwiched between two Nb layers, one from the trilayer and the second being the top electrode

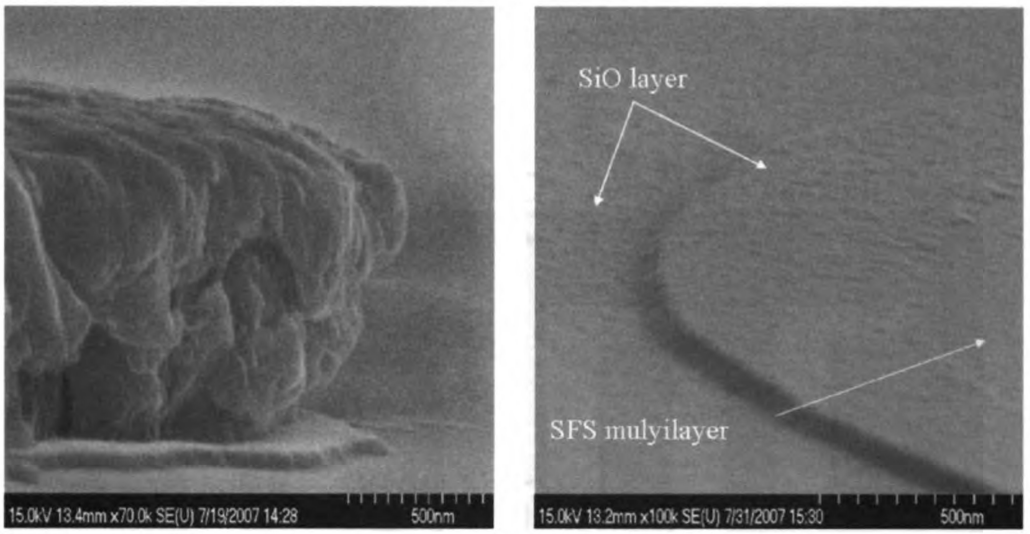

Figure 5.13: 7 a: Sample after lift off in acetone b: Sample after lift off in the remover.

sputtered last. Figure 5.14 is a cartoon of a sample ready for testing. A schematic diagram of our SFS Josephson junctions is shown in Figure 5.15.

5.2 Measurements

After the sample is prepared and ready for measurements, it is mounted on a quick dipper, which is a dip-stick with sample holder, superconducting magnet to provide the magnetic field and a superconducting quantum interference device (SQUID) null detector. All the four-probe measurements were performed at 4.2 K by inserting the quick dipper slowly into a 60 lt liquid Helium dewar equipped with a cryoperm shield. Each sample had 6 Josephson junctions of diameters 10 (2), 20 (2), 40, and 80 μm. The normal-state resistances of our Josephson junction pillars vary from 2 $\mu\Omega$ to 120 $\mu\Omega$, depending mostly on the pillar area. Resistances in this range require an extremely sensitive low noise measurement technique which is provided by using a superconducting quantum interference device (SQUID) as a null detector in a current-comparator circuit shown in Figure 5.16 [51]. A known current (I_S) passes through the sample (R_S), and the current (I_{ref}) through the reference resistor (R_{ref}) is varied

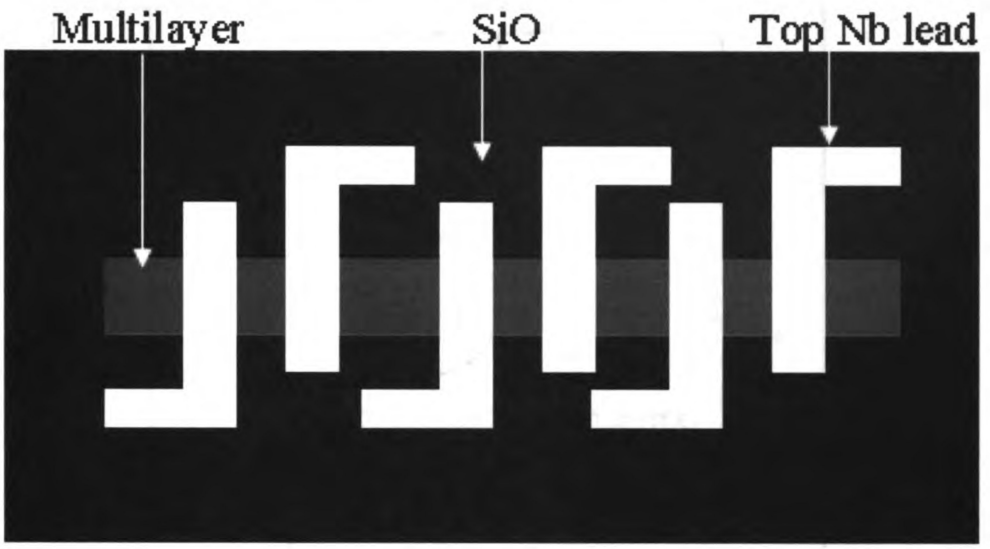

Figure 5.14: Cartoon showing the finished sample ready for measurement.

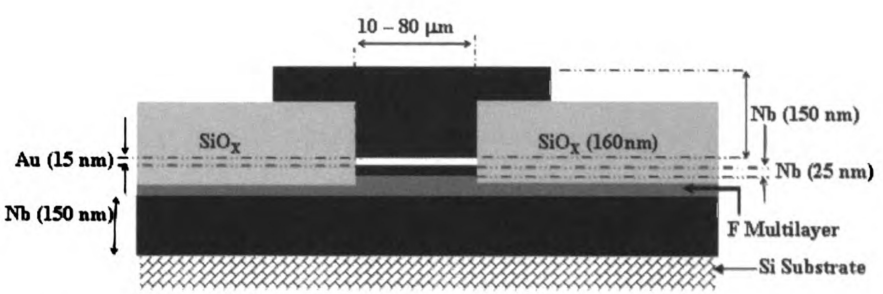

Figure 5.15: Schematic diagram of S/F/S Josephson junction cross section. Current flow is in the vertical direction. The magnetic field is applied in the plane of the layers, i.e. perpendicular to the current direction.

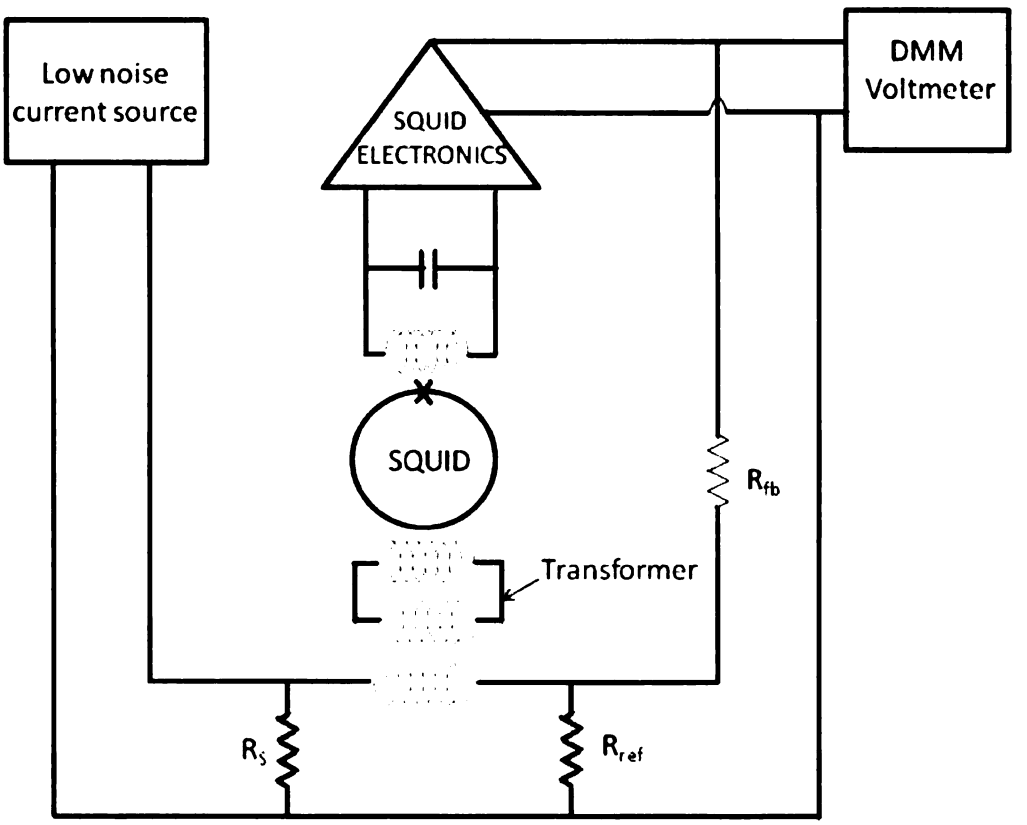

Figure 5.16: A low-temperature potentiometer circuit in feedback mode for measuring resistances in the nΩ range.

until the potential across the reference resistor exactly balances the potential across the sample. Further details about the measurement setup can be found elsewhere [84, 53, 54].

Chapter 6

Experimental results

6.1 Introduction

As described in detail in the theory chapter of this thesis, when a ferromagnetic metal is sandwiched between two conventional superconductors to form what we call an SFS Josephson junction, then by proximity the superconducting correlations can penetrate into the F-layer. As a consequence of the exchange splitting of the spin-up and spin-down electrons in the ferromagnet, the superconducting pair correlation oscillates and decays exponentially as a function of the F-layer thickness. If the F-layer has some sort of magnetic inhomogeneity then a new type of spin symmetry can be induced at the SF interface. It is known as the spin triplet in which the electrons have their spins pointing in the same direction, and as a result they will not be affected by the exchange field, so they can penetrate the F-layer for long distances as given Eq. (4.2). In section 6.2 we discuss our early data of Co Josephson junctions, then in section 6.3 we introduce the idea of a synthetic antiferromagnet. In section 6.4 the magnetic behavior of junctions with the synthetic antiferromagnetic layer is explained, and in section 6.5 the I_c R_N versus the F-layer thickness is discussed and finally in section 6.6 we discuss the possible reasons for the lack of indication of spin triplet correlations

in these samples.

6.2 Early data of Co Josephson junctions

For the purpose of studying this new type of spin symmetry, our strategy was to search for a Josephson effect in a SFS system where the central layer is thick enough so that the Josephson effect due to the spin singlet electron pairs is very small. We chose to work with Nb as a superconductor because it has a critical temperature 9.2K, which allows measurements at 4.2K. Also we chose to work with the strong ferromagnet Co (T_C =1388 K for bulk), because it has a long spin diffusion length with a lower bound of 40 nm. Having a long spin diffusion length helps the triplet order parameter penetrate deep into the F-layer. Our first set of samples were of the form Nb(150)/Co(d_{Co})/Nb(25)/Au(15)/Nb(150) with all thicknesses in nm. Recall that the Au-layer on top of Nb prevents oxidation during processing.

As we explained in chapter three, the best way to characterize Josephson junctions is to apply a magnetic field parallel to the plane of the junction, and observe the modulation of the critical current as a function of magnetic field H_{ext} known as the Fraunhofer pattern. Since our junctions are circular pillars, the Fraunhofer pattern is actually a Bessel function of the applied field given by Eqn. (3.42). Observation of a good Fraunhofer pattern demonstrates that the supercurrent is uniform across the junction area, and that there are no short circuits in the surrounding SiO_x insulator. An example for a circular junction of diameter 40μm, with a single Co layer 5 nm thick, is shown in Figure 6.1. The deep minima in I_c at $H = -5$ and +8 Oe demonstrate that there are no shorts in the oxide surrounding the junction. The overall pattern, however, is quite random, so why is that? In Josephson junctions containing magnetic materials, the magnetization breaks up into domains with different relative orientations. This leads to a random pattern of magnetic flux in

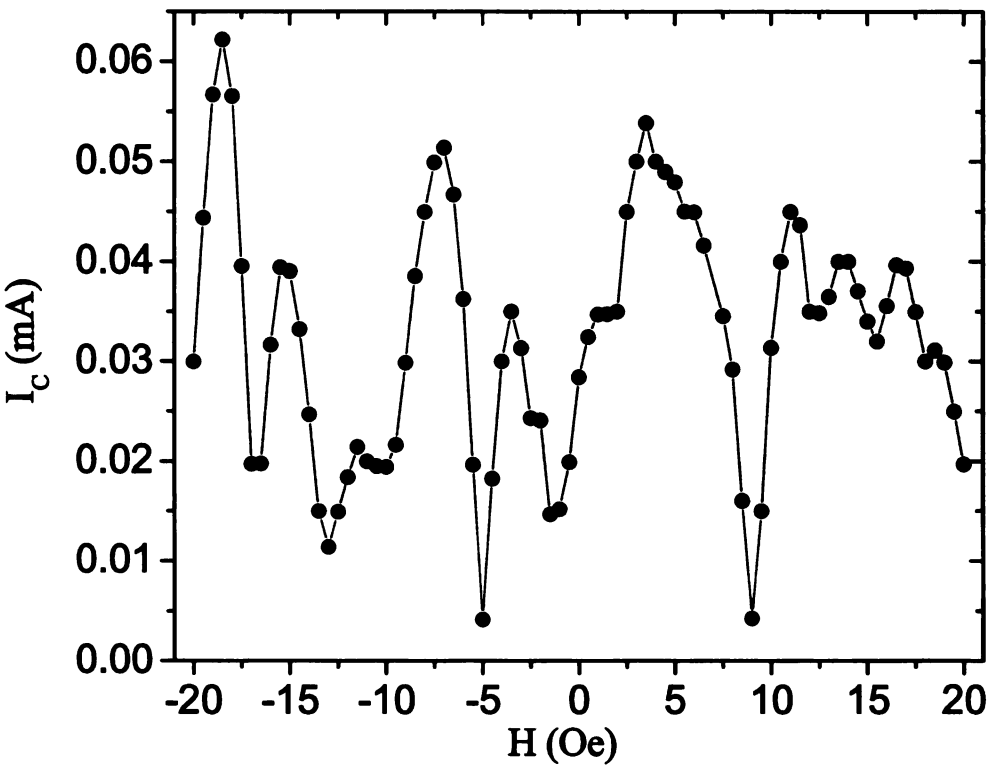

Figure 6.1: Critical current vs. magnetic field applied in the film plane (perpendicular to the current direction) for a Nb/Co/Nb circular Josephson junction of diameter 40 μm and d_{Co}= 5 nm.

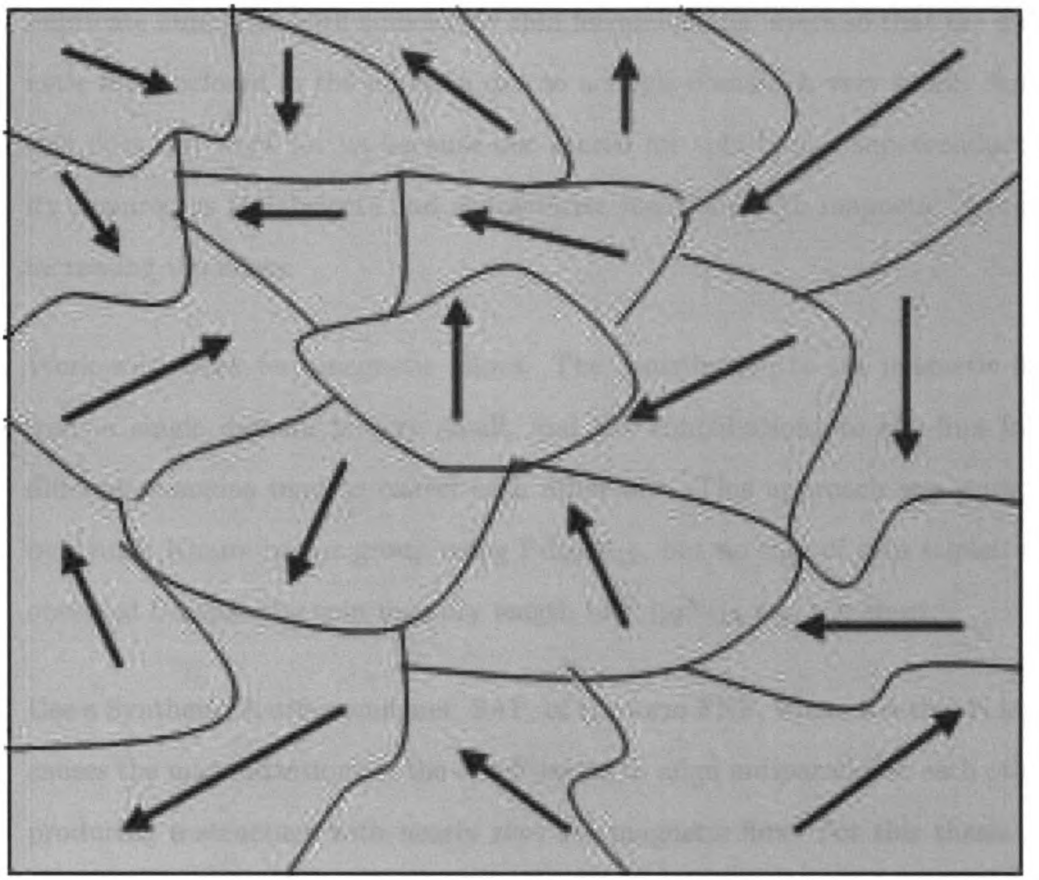

Figure 6.2: Schematic of ferromagnet domain structure.

the junction, which in turn distorts the pattern. Figure 6.2 shows a cartoon of the magnetic domain structure of Co. There are several approaches that can be used to overcome the problem of intrinsic flux trapped in the ferromagnetic junction that leads to the distortion of the Fraunhofer pattern:

1. Fabrication of ultra small lateral dimensions ferromagnetic Josephson junctions. Junctions in this regime will probably be single domain structures, so the intrinsic magnetic flux in the junction will be reduced, and one may get good Fraunhofer patterns [55, 56]. This option is not good for us as we are looking for the long range triplet superconductivity since it will become less effective as the thickness of the ferromagnetic layer is increased.

2. Fabricate Junctions with sufficiently thin ferromagnetic layers so that the magnetic flux enclosed in the junction due to a single domain is very small. Again this does not work for us because our search for spin-triplet superconductivity requires us to fabricate and characterize junctions with magnetic layers of increasing thickness.

3. Work with weak ferromagnetic alloys. The contribution to the magnetic flux from a single domain is very small, and the contributions to the flux from different domains tend to cancel each other out. This approach was pursued by Trupti Khaire in our group using $Pd_{82}Ni_{12}$, but no sign of spin triplet was observed because the spin memory length in $Pd_{82}Ni_{12}$ was too short.

4. Use a Synthetic Antiferromagnet, SAF, of the form FNF, where the thin N layer causes the magnetizations of the two F-layers to align antiparallel to each other, producing a structure with nearly zero net magnetic flux. For this thesis, we have chosen option 4.

6.3 Synthetic Antiferromagnet "SAF"

The phenomenon of antiferromagnetic coupling between F-layers across a nonmagnetic spacer layer was first discovered by Grünberg [57] in 1986. Thin film structures composed of ferromagntic thin layers separated by a nonmagnetic spacer have attracted a lot of interest especially after the discovery of the Giant Magnetoresistance (GMR) effect in 1988 [58, 59]. In zero field, when the magnetization of the two F-layers on either side of the spacer layer are ordered antiparallel to one another, this structure is known as a Synthetic Antiferromagnet or "SAF". When the magnetizations are ordered parallel to one another, the structure is Ferromagnetically coupled. This is shown schematically in Figure 6.3. The antiferromagnetic coupling of the

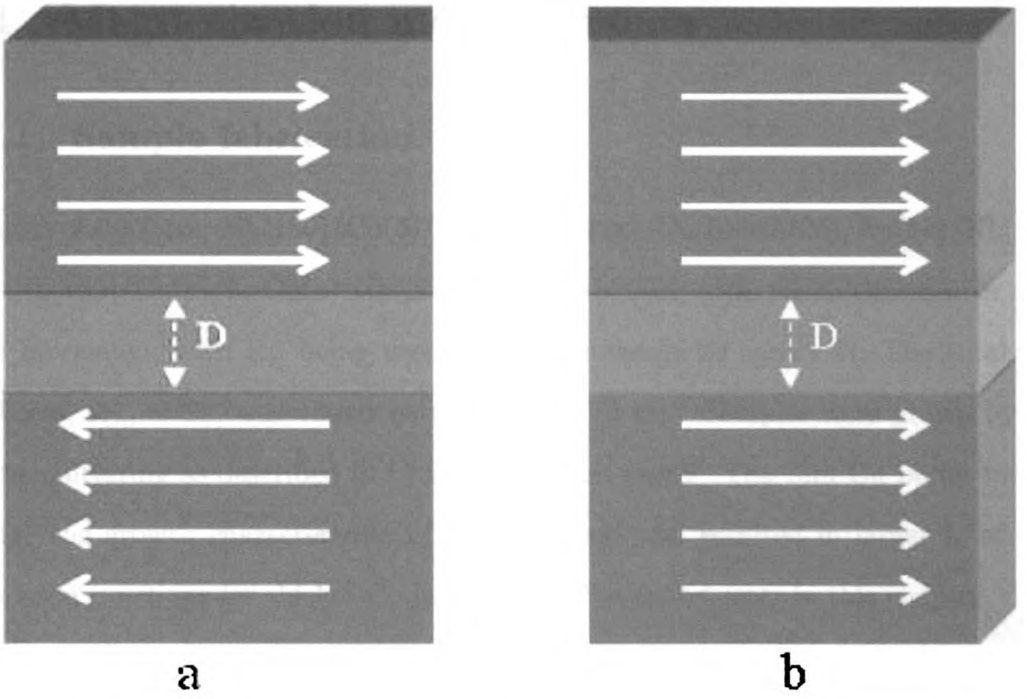

Figure 6.3: Coupling of two ferromagnetic layers through a thin non magnetic spacer. a) Antiferromagnetic coupling "SAF". b) Ferromagnetic coupling.

moments is due to the well-known oscillatory interlayer exchange coupling in which the two ferromagnetic layers exhibit an exchange coupling that oscillates between ferromagnetic and antiferromagnetic depending on the thickness of the non-magnetic spacer [60, 61]. The largest contribution to the oscillating interlayer exchange coupling comes from the RKKY coupling, named after Rudermam, Kittel, Kasuya and Yosida [62]. In RKKY coupling, spins in one ferromagnetic layer are coupled by a local exchange interaction to a conduction electron in the spacer layer which then transfers to distant spin in another layer via another local exchange interaction. Strong antiferromagnetic coupling leads to a flux cancelation in the two F layers. This is what we are looking for, because it will insure that the Fraunhofer pattern will not be shifted and a clear peak at zero magnetic field will be measured. If there is any shift, it will be minimal.

6.4 Magnetization measurements

6.4.1 Sample fabrication

Samples of the form: Nb(150)/Cu(5)/Co(x)/N/Co(x)/Cu(5)/Nb(25)/Au(15)/Nb(150), and Nb(150)/Co(x)/N/Co(x)/Nb(25)/Au(15)/Nb(150) with all thicknesses in nm were fabricated, with Ru being used as the non-magnetic spacer N. The total Co thickness, $d_{Co} = 2x$, was varied between 4 and 12 nm. Samples were grown by dc triode sputtering as described in Chapter 5 of this thesis. The thin Cu buffer layers change the growth characteristics of the Co layers and resulted in larger I_c of the Josephson junctions for thicker Co layers as will be shown later in this chapter. The thin copper layers can be considered superconducting as they will be completely penetrated by the proximity effect from the two Nb electrodes on top and bottom of the Josephson junction. The shadow mask used to make these samples is shown in Figure 6.4. Each 0.5" x 0.5" sample chip has a 4-probe device for the Van der Pauw resistivity measurements (not used in this thesis), as well as a 9.4 x 5.1 mm^2 rectangular device used for M vs. H measurements. Once the sputtering run is done, the samples were taken to the SQUID measurement room, and cut in the middle to separate the two devices. We then use the rectangular part for the magnetic measurements, and the other one is kept as backup, in case the magnetization measurements data look strange so we can check the quality of our Nb film. For the magnetic measurements no processing of the samples is needed.

6.4.2 Magnetization measurements using SAF with Ru as the spacer

Our first choice for the nonmagnetic spacer was Ru. Our SAF is Co/Ru/Co, with a Ru thickness of 0.6 nm [60]. At this thickness, the Ru layer couples the two Co layers

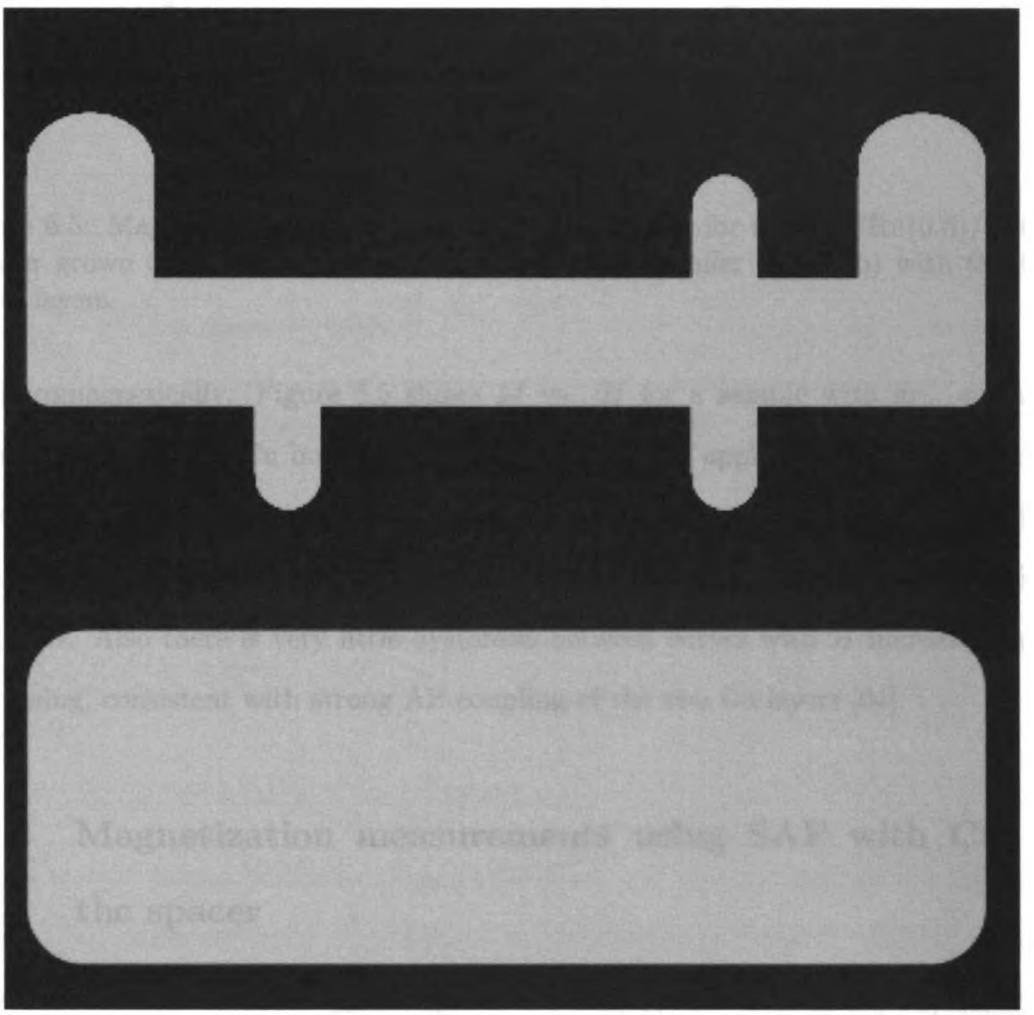

Figure 6.4: Shadow mask used to make rectangular samples used in the M vs H measurements.

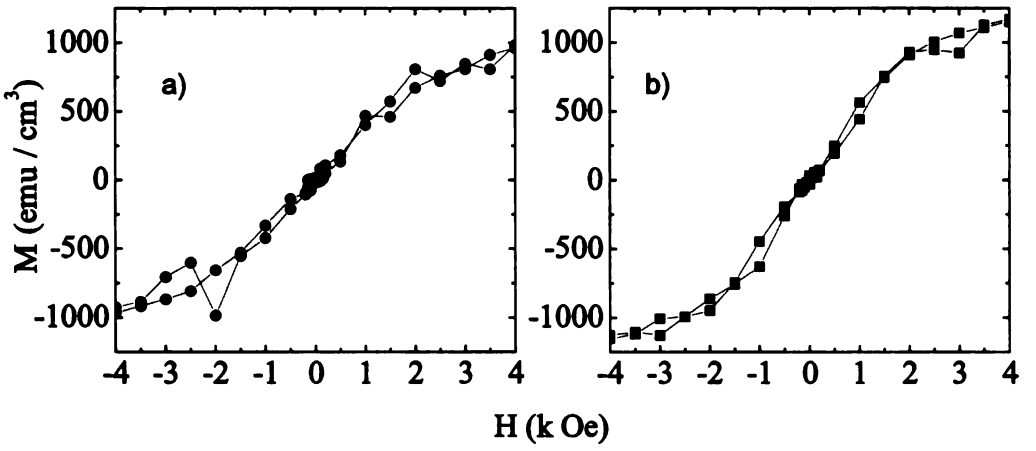

Figure 6.5: Magnetization vs. applied field at T = 10K for a Co(4)/Ru(0.6)/Co(4) trilayer grown on 150 nm of Nb. a) without the Cu buffer layers, b) with the Cu buffer layers.

antiferromagnetically. Figure 6.5 shows M vs. H for a sample with d_{Co} = 4nm, with and without the Cu buffer layers. It was only after application of a sufficiently large magnetic field of about 5 kOe, the two moment of the Co layers on either side of the Ru spacer layer become aligned in the same direction, and the magnetization saturates. Also there is very little hysteresis between curves with H increasing and decreasing, consistent with strong AP coupling of the two Co layers [64].

6.4.3 Magnetization measurements using SAF with Cu as the spacer

Another choice for the nonmagnetic spacer was Cu [63]. Our SAF is Co/Cu/Co, with a Cu thickness of 0.8 nm. At this thickness, the Cu layer couples the two Co layers antiferromagnetically. Figure 6.6 shows M vs. H for a sample with d_{Co} = 4nm. M saturates quickly when H is at about 150 Oe, and there is a large hysteresis between curves with H increasing and decreasing, indicating a weak antiferromagnetic coupling of the two Co layers. According to [63], the coupling strength at the first antiferromagnetic oscillation in the Co/Cu/Co system is 30 times smaller than that

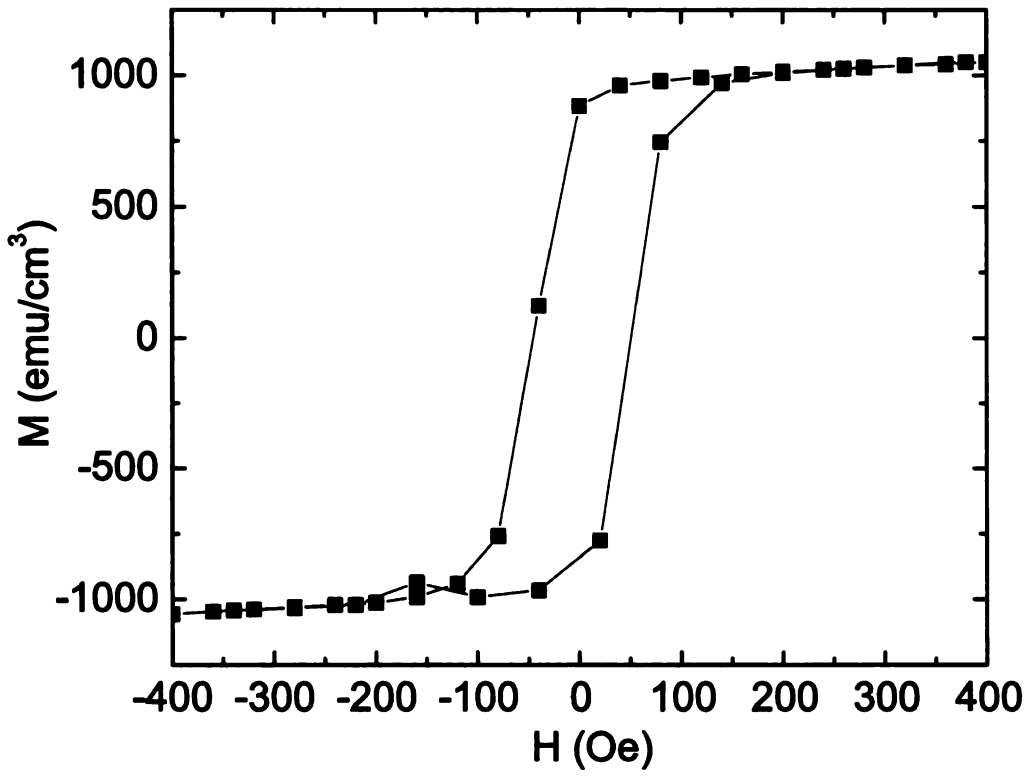

Figure 6.6: Magnetization vs. applied field at T = 10K for a Co(4)/Cu(0.8)/Co(4) trilayer grown on 150 nm of Nb.

in the Co/Ru/Co system.

6.4.4 Magnetically dead layers

The reduction of the thickness of magnetic films and the presence of the interface might significantly influence the magnetic properties of the films. In 1969, L. Liebermann et al. [65] studied the thickness dependence of magnetization of iron films. The thickness was increased atomic layer by atomic layer. They noticed that the Fe film had two layers that were nonmagnetic. Later in the year 1970, they [66] observed similar effect in Ni and Co samples, and they introduced the term dead layer to indicate the loss of magnetic moment of the ferromagnetic layer. Magnetic dead layers exist at the surface/and or interfaces, and may form during the deposition of the multilayers, or during the fabrication process due to interface diffusion. It manifests itself as a

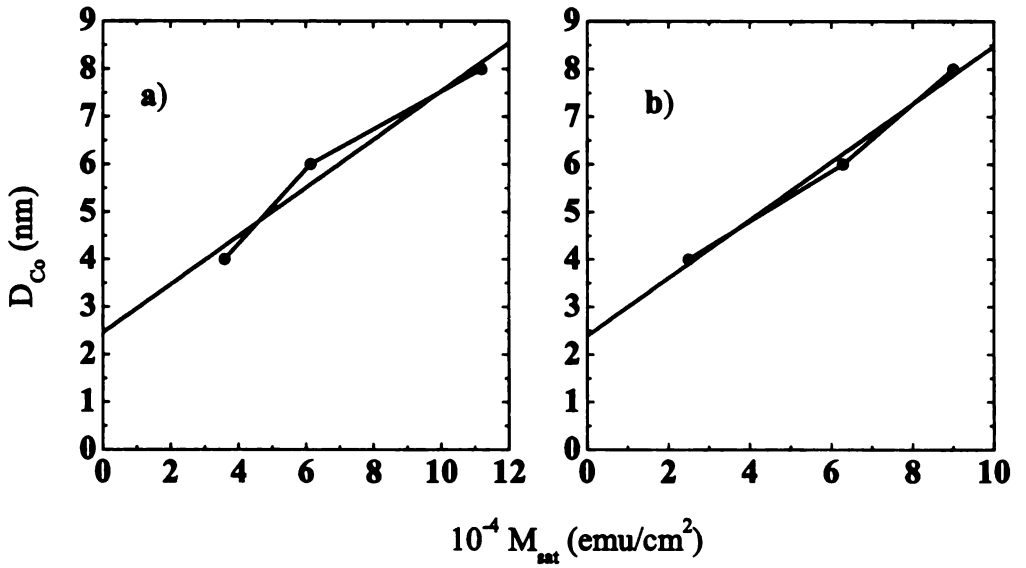

Figure 6.7: Saturation magnetization per unit area measured by a SQUID magnetometer at $T = 10$K vs Co thickness. a) samples with the Cu buffer layer. b) samples without the Cu buffer layer. Solid lines are least-square fits to the data.

loss of magnetic moment of the ferromagnetic layer. Formation of the magnetic dead layer and its extent depend on the temperature, ferromagnetic material-whether it is pure element or alloy-, and the layers used to make the interfaces with the ferromagnetic layer. For thick ferromagnetic layers, this effect can be neglected, but it becomes very important for thin film structures, where the thickness of the ferromagnetic layer approaches the thickness of the dead layer, D_{dead}. To estimate the magnetic dead layer, we plot M_{sat} vs. the Co thickness and do a linear fit. If the fitting line passes through the origin then the ferromagnetic layer has no dead layers. If otherwise it passes a certain thickness, then the intercept at the vertical axis (the Co film thickness) indicates the total magnetic dead layers thickness associated with the interfaces of the ferromagnetic film. Figure 6.7 shows the thickness dependence of the ferromagnetic layers as a function of the saturations magnetization, M_{sat} for two sets of samples. Figure 6.7a shows data for samples with a Cu buffer layer between the Co and the Nb electrode, Nb-Cu-Co-Ru-Co-Cu-Nb. It is obvious that

our samples are magnetic, but there is a dead layer of 2.52 ± 0.20 nm. Since the Co in this case has four interfaces (Cu-Co, 2(Co-Ru), and Co-Cu), then there could be a dead layer at every interface. But according to [67], Cu/Co interfaces don't form dead layers, which means that the dead layer in our systems should be originated at the Co/Ru interfaces. It is known that growing Co into Ru and vice versa lead to the formation of CoRu alloys, and depending on the concentration of Ru, a magnetic dead layer may form [68, 69, 70, 71, 72]. Figure 6.7b shows data for samples without a Cu buffer layer between the Co and the Nb electrode, Nb-Co-Ru-Co-Nb. The intercept is 2.39 ± 0.38 nm. Again, the Co in this case has four interfaces (Nb-Co, 2(Co-Ru), and Co-Nb), so the estimated dead layer of every interface ranges from 0.50-0.69 nm. Previous studies [55, 72, 73, 75] showed that Nb/Co interfaces have a dead layer of 0.5-1.0 nm, which is in agreement with our data (of course with the extra dead layer resulting at the Co/Ru interfaces). The average magnetization of Co is determined from the inverse slopes of Figures 6.7a and b. For samples with the Cu buffer layer, the average magnetization is 1969.85 ± 373.79 emu cm^{-3}, while for samples without the Cu buffer layer, the average magnetization is 1642 ± 158.8 emu cm^{-3} (M_{sat} for bulk Co = 1420 emu cm^{-3} [76]). The magnetization curves were measured at 10 K for all our samples, using SQUID magnetometer. The field was applied in the direction parallel to the film plane. In order to estimate the saturation magnetization M_{Sat} of our samples, we should subtract the diamagnetization contribution from the Nb electrodes and the silicon substrate. To do that, we scan the field up to 20 K Oe. The diamagnetic effect appears at about 5 K Oe. So we do a linear least square fit to the diamagnetic part with the y- intercept being the M_{Sat} . An example is shown in Figure 6.8.

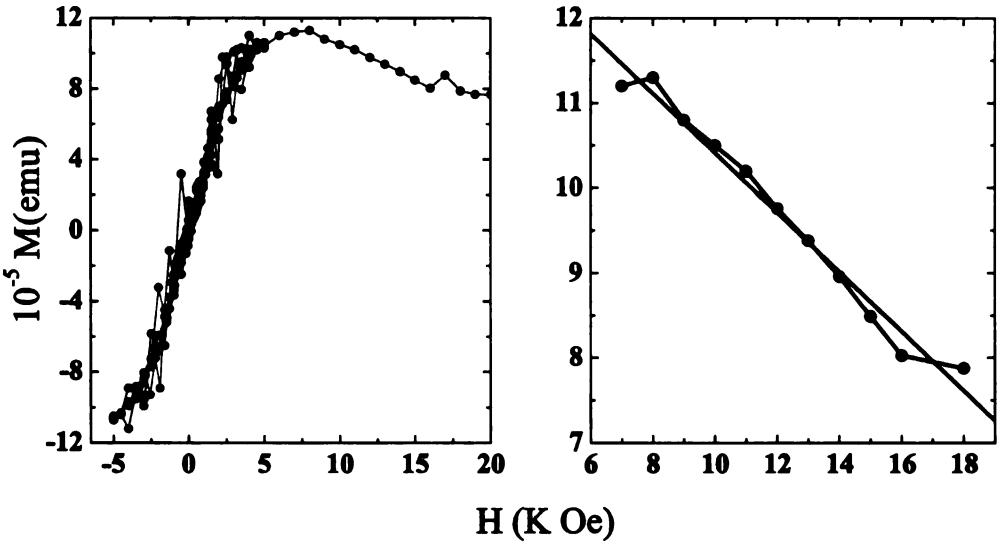

Figure 6.8: Example of the estimation of the saturation magnetization. a) Magnetization vs. applied field at $T = 10$K for a Co(3)/Ru(0.6)/Co(3) trilayer grown on 150 nm of Nb. b) Linear least square fit to the diamagnetic part of a) with the y-intercept being the M_{Sat}.

6.5 Magnetic field diffraction patterns of Josephson junctions containing SAF with Ru as the spacer

As it was shown in section 6.2, it is possible to circumvent the problem of flux trapped in Josephson junctions containing strong ferromagnetic materials by fabricating Josephson junctions containing the SAF trilayer, Co(x)/Ru(0.6)/Co(x). Multilayer samples of the form Nb(150)/Cu(t)/Co(x)/Ru(0.6)/Co(x)/Cu(t)/Nb(25)/Au(15), with all thicknesses in nm, were grown by dc triode sputtering. In this run, the total Co thickness, $d_{Co} = 2x$, was varied between 4 and 12 nm. Two sets of samples were prepared, one set with a 5 nm thick Cu buffer layer between the Nb and Co layers, and the other set has no Cu buffer layers. Figure 6.9 shows the Fraunhofer diffraction patterns for an SFS Josephson junctions using the artificial antiferromagnetic trilayer

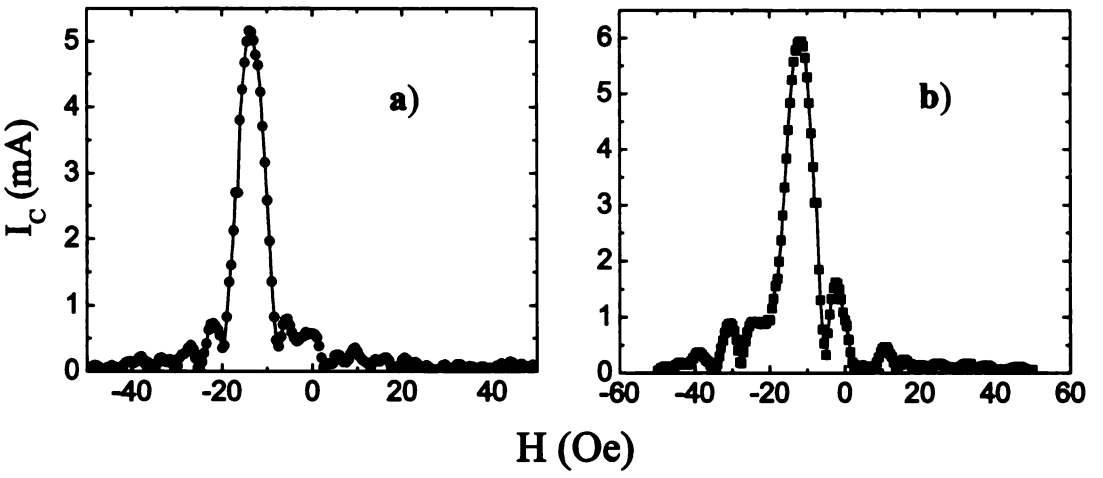

Figure 6.9: Critical current vs. applied magnetic field obtained for two of our circular Josephson junctions with total thickness of the Co layer is 4 nm: a) With the Cu buffer layers, b) Without the Cu buffer layers. The pillar diameter is 20 μm in both samples.

Co(2)/Ru(0.6)/Co(2) as the F-layer with and without the Cu buffer layers. The maximum critical currents in both figures are very close, which may indicate that the additional Cu buffer layers don't make any difference in the measured critical current of the junctions. But what is remarkable about these junctions is that the Fraunhofer patterns are extremely high quality and are centered very close to zero applied field, which demonstrates drastic changes in the critical current amount and form of the Fraunhofer pattern compared to the samples without the synthetic antiferromagnetic layer shown in Figure 6.1. The fact that samples with only Ru inserted but without Cu showed the same high quality Fraunhofer pattern as the sample with Ru and Cu both inserted, is a strong evidence that the thin Ru spacer is responsible for the high quality Fraunhofer patterns, not the Cu layer. A new set of samples without the Cu buffer layers were fabricated for total Co thicknesses of : 3, 5, 7, 9, 11, and 12 nm. All of them showed excellent Fraunhoffer patterns; a discussion of the critical current vs. applied magnetic field will be given later. When we measured samples from the same run but with thicker Co with and without the Cu buffer layers, it was

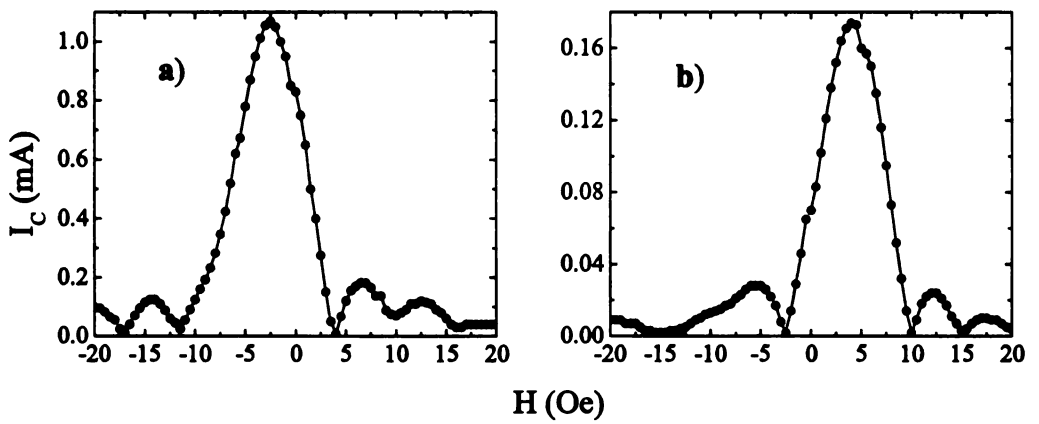

Figure 6.10: Critical current vs. applied magnetic field obtained for two of our circular Josephson junctions with total thickness of the Co layer is 8 nm: a) With the Cu buffer layers, b) Without the Cu buffer layers. The pillar diameter is 20 μm in both samples.

clear that the critical current is larger in samples with the Cu buffer layers as shown Figure 6.10. All junctions reported in this thesis from now on have the Cu buffer layers. A new set of junctions with total Co thickness as thin as 2 nm and as thick as 23 nm were fabricated, and measured. Figure 6.11 shows Fraunhofer patterns for four junctions with total thickness varying from 6.1 to 23 nm. All junctions have Josephson penetration depth, λ_J larger than one-quarter of the junction diameter. This ensures uniform current density in the Josephson junction. The solid lines are fit to Equation (3.42), taking into account the shift in the central peak. The first three patterns are almost textbook-like Airy patterns, while the fourth one is very good. The central maximum is slightly shifted from $H = 0$ by only a few Oe, which indicates a very strong antiferromagnetic coupling between the top and bottom Co layers in the SAF trilayer, Co(x)/Ru(0.6)/Co(x). To test the strength of the antiferromagnetic coupling of the two F-layers, one Josephson junction of total Co thickness 5.8 nm was subjected to a series of large in-plane magnetic fields, then I_c vs. H was remeasured at low field. After applying a large in-plane field, the Nb electrodes trap some flux, so it is very important to get rid of it. The way to do that is to pull the sample out of the

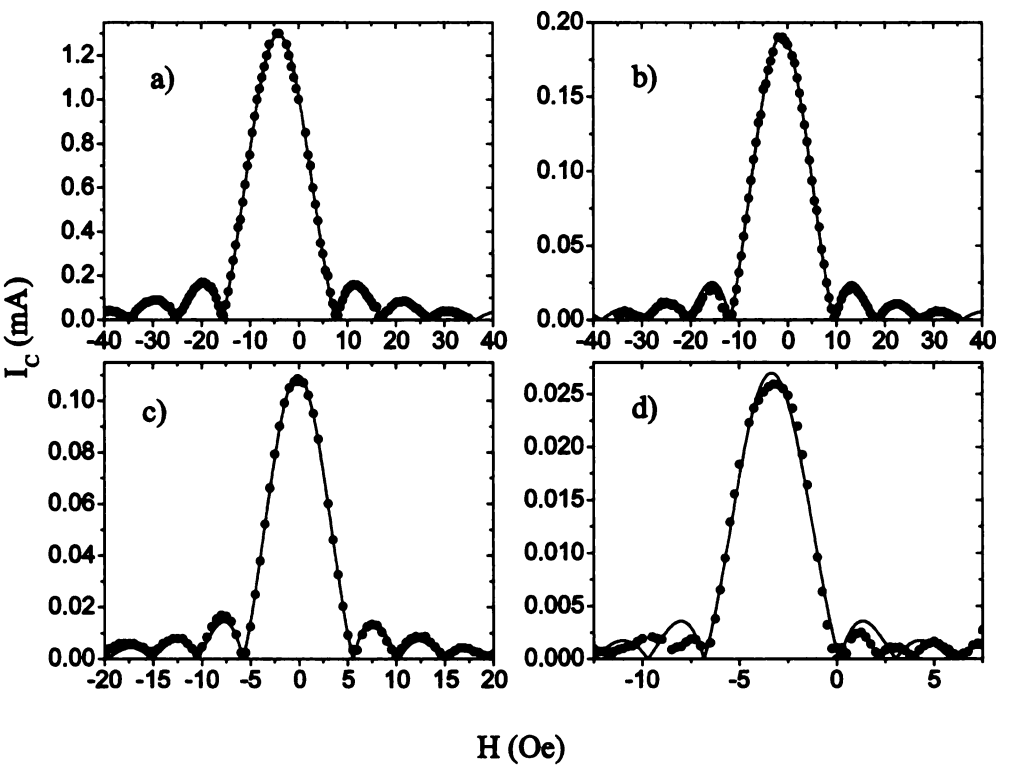

Figure 6.11: Critical current vs. applied magnetic field obtained for Nb/Cu/Co/Ru/Co/Cu/Nb circular Josephson junctions with different total thickness of the Co layers:a) 6.1 nm, b) 11nm, c) 18 nm, and d) 23 nm. The pillar diameters w are 10, 10, 20, and 40 μm, respectively. The solid lines are fits to Eq. (3.42).

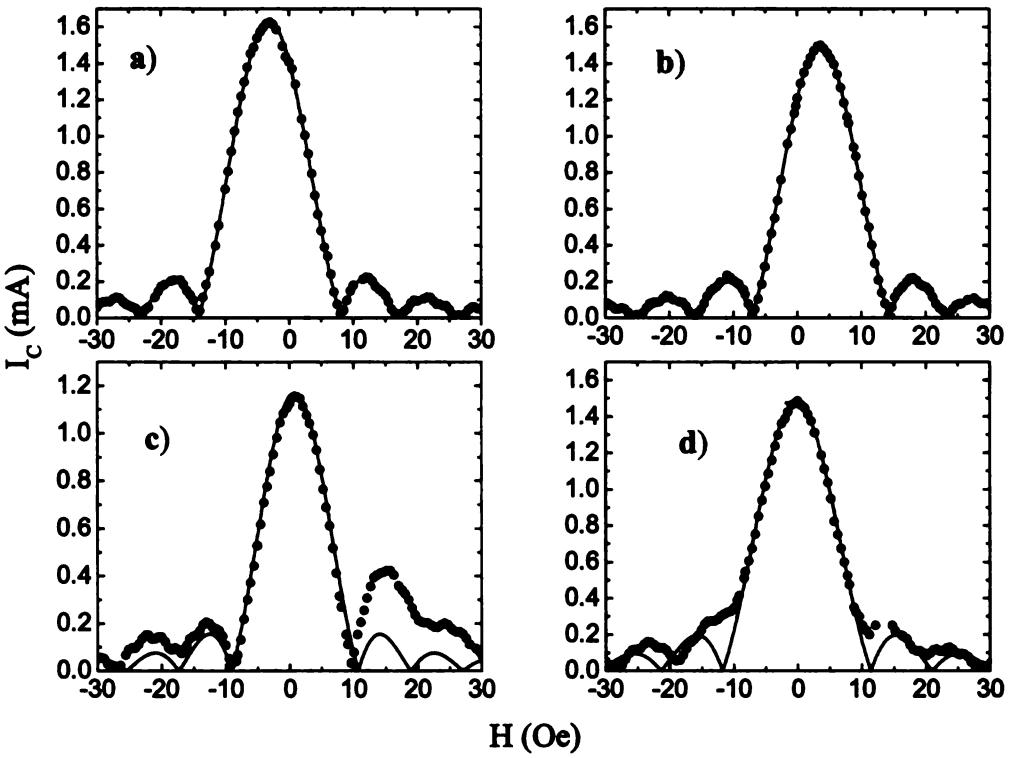

Figure 6.12: Critical current vs. applied magnetic field obtained for circular Josephson junctions with total Co thickness of 5.8 nm magnetized to :a) zero field, b) 1 kG, c) 2 kG, and d) 5 kG. The pillar diameter is 20 μm. The solid lines are fits to Eq. (3.42).

liquid Helium (just pull it up so it is barely above the liquid helium level) for about one minute, then cool it back to 4.2 K and measure I_c vs. H. Figure 6.12 shows the Airy pattern before and after magnetization to different magnetic fields. It is obvious that magnetizing the sample up to 5 kG resulted in no or very slight distortion to the Airy patterns. It was only after magnetizing the sample to 10 kG, the central peak in the Airy pattern split into two peaks about half the original magnitude. As we are working with strong ferromagnet, it is possible that the magnetic configuration of the two Co layers has changed, which lead to a finite magnetization trapped in the junction. Leaving the sample to warm up to room temperature for two days, and remeasuring I_c vs. H at low field resulted in excellent Airy pattern as shown in Figure 6.13.

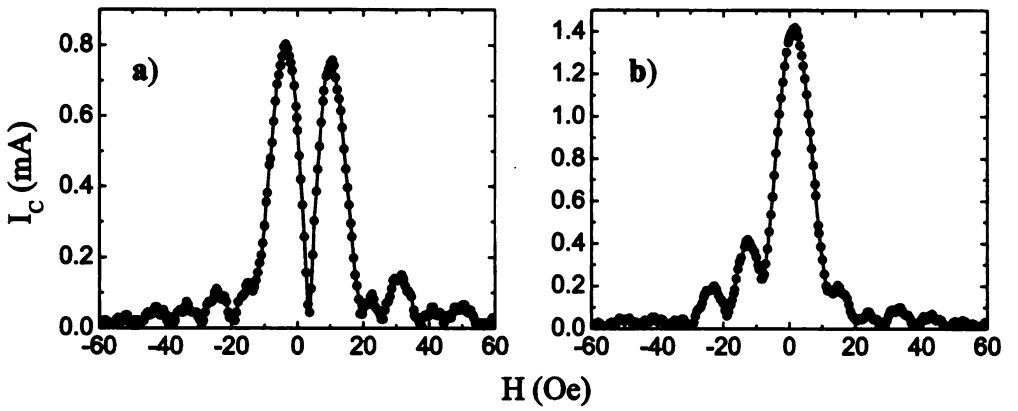

Figure 6.13: Critical current vs. applied magnetic field obtained for circular Josephson junctions with total Co thickness of 5.8 nm: a) magnetized 10 kG, b) after warming the sample to room temperature and recooling. The pillar diameter is 20 μm.

6.6 Critical current vs. Co thickness

Replacing the single Co layer by two layers separated by a 0.6 nm thick Ru layer allowed us to study SFS Josephson junctions with total Co thickness up 23 nm, nearly five times larger than what had been studied before [55]. Figure 6.14 shows the product of critical current times normal state resistance vs. total Co thickness for all of our SAF Josephson junctions. Triangles are data for samples without Cu buffer layers, while circles are data for samples with Cu buffer layers. In both cases I_c R_N decays exponentially with increasing d_{Co}. For junctions not containing the Cu buffer layers, the decay is faster than in junctions with Cu. Neither of the two data sets show a clear oscillations (transition to the π state) as a function of d_{Co}, but there are a few data points (e.g., for d_{Co}= 4.0, 18, and 23 nm) that have large fluctuations. To address the issue of oscillations, we fabricated a set of samples in one sputtering run with closely spaced Co layer thicknesses in the range $4.3 - 6.1$ nm. Those samples do not exhibit any local minima in I_c, whereas Robinson *et al.* [55] observed a spacing of 1.0 nm between local minima for Nb/Co/Nb junctions containing a single Co layer. So why didn't we observe any oscillations?

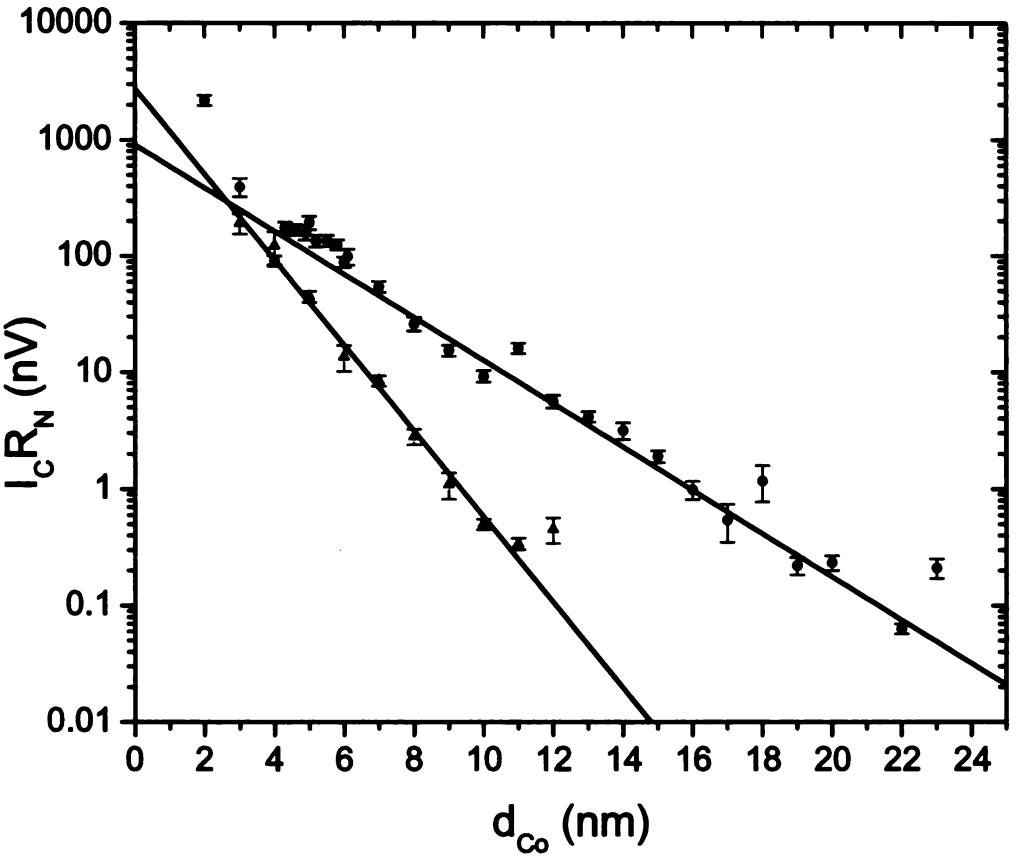

Figure 6.14: Product of critical current times normal state resistance vs. total Co thickness for all of our SAF Josephson junctions. Triangles are data for samples without Cu buffer layers, while circles are data for samples with Cu buffer layers. Error bars represent the standard deviation of measurements taken on more than one pillar on the same substrate, with the minimum uncertainty chosen to be 10%. The solid lines are fits to a simple exponential decay, with decay lengths of 1.18 ± 0.05nm and 2.34 ± 0.08nm, respectively.

6.7 Theory of SFFS Josephson junctions

Theoretically, the Josephson effect in multilayered SFS junctions has been studied by several groups in different regimes. There are three energy scales whose relative size determines three different regimes. The energy scales are the exchange energy in the ferromagnet, E_{ex}, the gap in the superconductor, Δ, and $\hbar/\tau$, the inverse of the mean free time between collisions of an electron propagating in the ferromagnet. In all of the experimental work on SFS Josephson junctions published to date, including this work, $E_{ex} \gg \Delta$. There is a wide variation, however, in the size of $\hbar/\tau$ relative to those two energies:

1. The clean limit is expressed by $\Delta\tau \gg \hbar$, which also implies $E_{ex}\tau \gg \hbar$ [77, 78].

2. The intermediate limit is expressed by $E_{ex}\tau \gg \hbar$ but $\Delta\tau \ll \hbar$, [36, 79].

3. The dirty limit is where both $\Delta\tau \ll \hbar$ and $E_{ex}\tau \ll \hbar$, [80, 82].

To answer the question, why we didn't observe any oscillations in Figure 6.14, consider the clean SFFS josephson junction shown in Figure 6.15 studied theoretically by [77]. In this limit, the critical current density is given by:

$$j \cong -\frac{2j_0}{\sqrt{\pi}}\frac{\hbar v_F}{ha} exp(-\frac{h^2a^2}{\hbar^2 v_F^2}) \sin\varphi \tag{6.1}$$

where v_F is the Fermi velocity, h is the exchange field and a has the meaning of a typical scale of the interface fluctuations (the interfaces as presented in Figure 6.15 are not straight, but exhibit small fluctuations in position). Two features can be drawn from Equation 6.1: 1) the amplitude of the critical current decays exponentially. 2) symmetric junction with identical F-layers in the antiparallel configuration can't produce the π state. Consider a Cooper pair propagating from left to right between the two superconducting electrodes shown in Figure 6.15. They will acquire the

relative phase shift $\delta\varphi_1 = \frac{2hx_1}{\hbar v_f}$, with x_1 being the distance traversed in the first ferromagnetic layer. In the second ferromagnetic layer, the exchange field has the opposite sign, and the Cooper pair acquires a relative phase shift $\delta\varphi_2 = -\frac{2hx_2}{\hbar v_f}$, with x_2 being the distance traversed in the second ferromagnetic layer. For $x_1 = x_2$, the relative phases cancel each other out, and the ferromagnetic layer behaves similarly to a normal metal. Our data are consistent with this picture. The diffusive SFFS Josephson junction similar to the one shown in Figure 6.15 was studied theoretically in [80] where the Usadel equation is valid. The phase difference between the two layers is $\varphi = 2\chi$, the thicknesses of the two F-layers are d_1 and d_2. In the antiparallel configuration, the exchange field has the opposite direction in the two F-layers. The critical current I_c is given by:

$$I_c = I_0 Re[\frac{2}{\sin(d_+ id_-) + \sinh(d_+ id_-)}] \tag{6.2}$$

where

$$d_+ = \frac{d_1 + d_2}{\xi_F} \tag{6.3}$$

$$d_- = \frac{d_1 - d_2}{\xi_F} \tag{6.4}$$

For identical F-layers, $d_1 = d_2 = d$, the critical current is positive for any value of d, and hence SFFS systems with identical F-layers in the antiparallel configuration can't produce the π state.

Theoretical works on SFFS Josephson junctions cited above calculate the form of the critical current only in the pure ballistic limit, and in the diffusive limit, but not in the intermediate limit. Co Josephson junctions studied in this thesis fall into the intermediate limit, where $E_{ex}\tau \gg \hbar$, but $\Delta\tau \ll \hbar$, with Δ the superconducting gap. A large number of theoretical work has been done for SFS Josephson junctions in the intermediate limit, and predict I_c to oscillate and decay exponentially with a decay

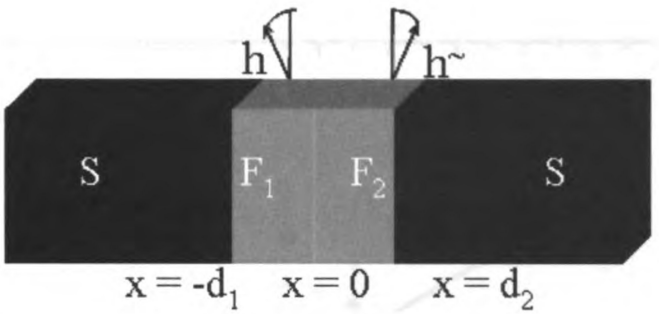

Figure 6.15: SFFS Josephson junction with noncollinear magnetization [80].

constant equal the mean free path in the F-layer [79, 36]. Equation (20) from [36] gives the dependence of the critical on F-layer thickness as

$$I_c(d_F) \propto \pi T \sum_{\omega>0} \frac{\Delta^2}{\Delta^2+\omega^2} \frac{\sin(d_F/\xi_F)}{d_F/\xi_F} \exp(\frac{-d_F}{l_e}(1+2\omega\tau)) \tag{6.5}$$

where the sum is over the positive Matsubara frequencies, $\omega_m = \pi k_B T(2m+1)$ with T the temperature. In our SFFS Josephson junctions , the oscillations are not present as explained earlier. The solid lines in Figure 6.14 are least-squares fits of an exponential decay to our two data sets, with decay lengths 2.34 ± 0.08 nm for the samples with Cu buffer layers and 1.18 ± 0.05 nm for the samples without Cu. This analysis suggests that the mean free path in the Co grown on the Cu buffer layer is longer than in the Co grown directly on Nb, probably due to less strain in the former case. The ratio of these with-Cu to without-Cu decay lengths is 2.0 ± 0.1. From the current-voltage characteristics of each sample, we have measured the normal state resistance at currents much larger than I_c. A plot of the specific resistance AR_N (area times resistance) vs. d_{Co} is shown in Figure 6.16. The interface and bulk contributions to AR_N are given by:

$$AR_N = 2AR_B + \rho_{Co} d_F \tag{6.6}$$

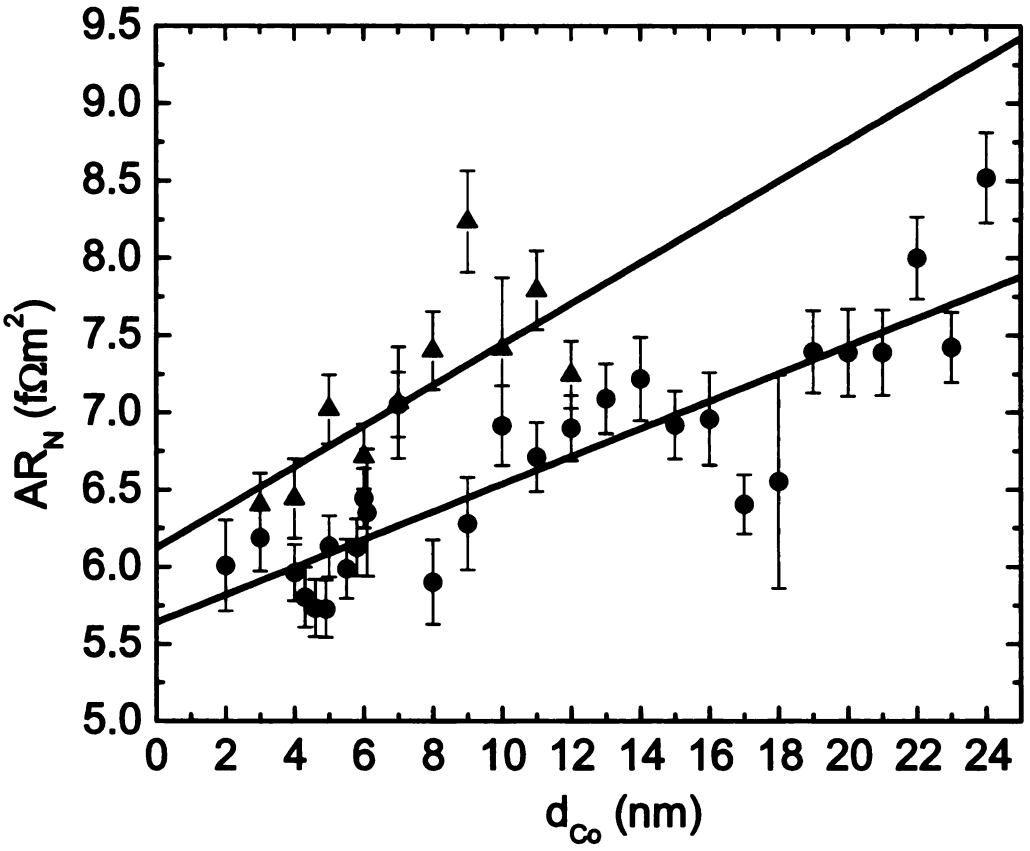

Figure 6.16: Area times normal-state resistance vs. d_{Co} for all of our Josephson junction samples. Triangles are data for samples without Cu buffer layers, while circles are data for samples with Cu buffer layers. The slope provides the resistivity of Co and the y-intercept provides twice the Nb/Co boundary resistance

where ρ_{Co} is the resistivity of Co, d_F is the thickness of the Co layer, and R_B is the Nb/Co boundary resistance. A linear fit to all samples with Cu gives a boundary resistance of $2AR_B = 5.64 \pm 0.12$ fΩ m^2 and a resistivity of Co, $\rho_{Co} = 89 \pm 10 n\Omega m$, and for samples without the Cu a boundary resistance of $2AR_B = 6.12 \pm 0.29 f\Omega m^2$ and a resistivity of Co, ρ_{Co}=130 ± 37 nΩ m. The effective resistivity of Co ρ^*_{Co} is inversely proportional to the mean free path as given by

$$\rho^*_{Co} = \frac{mv_f}{nel_e(1-\beta^2)} \tag{6.7}$$

where m is the electron mass, v_f is the fermi velocity, e is the electron mass, and β is the spin-scattering asymmetry, and n is the carrier density. The ratio of the mean free paths in the Co with-Cu to without-Cu determined from the slopes in Figure 6.16 is 1.5 ± 0.5. This mean free path ratio is consistent with the ratio for the decay lengths, as predicted by [36, 79] for SFS in the intermediate limit.

The single exponential decay of I_c vs. d_{Co} shown in Figure 6.14 indicates a lack of spin-triplet superconducting correlations in these samples, which would manifest themselves as a crossover to a slower decay with increasing d_{Co}. There are several possible reasons why we do not observe the long-range triplet correlations (LRTC). First, there could be too much spin-flip scattering at the Co/Ru interfaces. To address this issue, we have independently measured the spin memory loss at the Co/Ru interface using techniques borrowed from the giant magnetoresistance (GMR)community. These results are not discussed in this thesis, but our conclusion is that spin-flip scattering at the Co/Ru interfaces is not a strong effect. Second, it could be that there is not enough non-collinear magnetization (the LRTC requires non-collinear magnetizations), because the domain structure in the Co films contains mostly domains aligned along a single directions in space. Also it could be that the magnetic inhomogeneity is on the wrong length scale. According to theory [36, 39, 40], spin-triplet correlations are generated if the Cooper pairs from the superconductor experience regions of non-collinear magnetization within their coherence length, ξ_S. Let us refer to the length scale characterizing the magnetic inhomogeneity as δ_m. If $\delta_m \ll \xi_s$, then a Cooper pair will experience the magnetization averaged over the length ξ_s, and triplet correlations will not be produced efficiently. If $\delta_m \gg \xi_s$, then a typical Cooper pair experiences no magnetic inhomogeneity. Scanning electron microscopy with polarization analysis (SEMPA) measurements on Co films grown under similar conditions as ours reveal magnetic domains with typical sizes of about 3 microns, but with the magnetization directions of neighboring domains largely antiparallel as shown in Fig-

ure ?? [83]. Non-collinear magnetization resides only in the domain walls, which is apparently not enough to produce a significant amount of spin-triplet.

6.8 Magnetic field diffraction patterns of Josephson junctions containing SAF with Cu as the spacer

A year ago we thought that substituting Cu for Ru in our SAF could overcome the issue of spin memory loss. We know from GMR measurement that spin memory loss at the Co/Cu interface is only about 25% [84]. In section 6.4.3, we presented our magnetic measurements for the Co/Cu(0.8)/Co samples. Although the antiferromagnetic coupling is not as strong as in Co/Ru(0.6)/Co, we hoped that it would be strong enough to cause flux cancelation inside the Josephson junctions, which in turn can give good Fraunhofer patterns. Multilayers of the form Nb(150)/Cu(5)/Co(x)/Cu(0.8)/Co(x)/Cu(5)/Nb(25)/Au(15), with all thicknesses in nm, were grown on Si substrates as explained in chapter 5. The total Co thickness, $d_{Co} = 2x$, was varied between 4 and 28 nm. An example for a circular junction of diameter 24μm, is shown in Figure 6.18. The deep minima in I_c at $H = -12.5$, -2.5 and $+10$ Oe demonstrate that there are no shorts in the oxide surrounding the junction. The overall Fraunhofer pattern, however, is quite random due to the magnetic domain structure of the Co layers. Since the antiferromagnetic coupling in the Co/Cu(0.8)/Co is weaker than that of the Co/Ru(0.6)/Co, there is not enough cancelation of the magnetic flux in Co layers on either side of the Cu spacer, which leads to a net magnetic flux trapped in the Josephson jnuction, and as a result to a distorted Fraunhofer pattern. For comparison, Figure 6.18 looks very similar to Figure 6.1, where a single layer of Co was used in the Josephson junction. The distorted Fraunhofer pattern indicated that

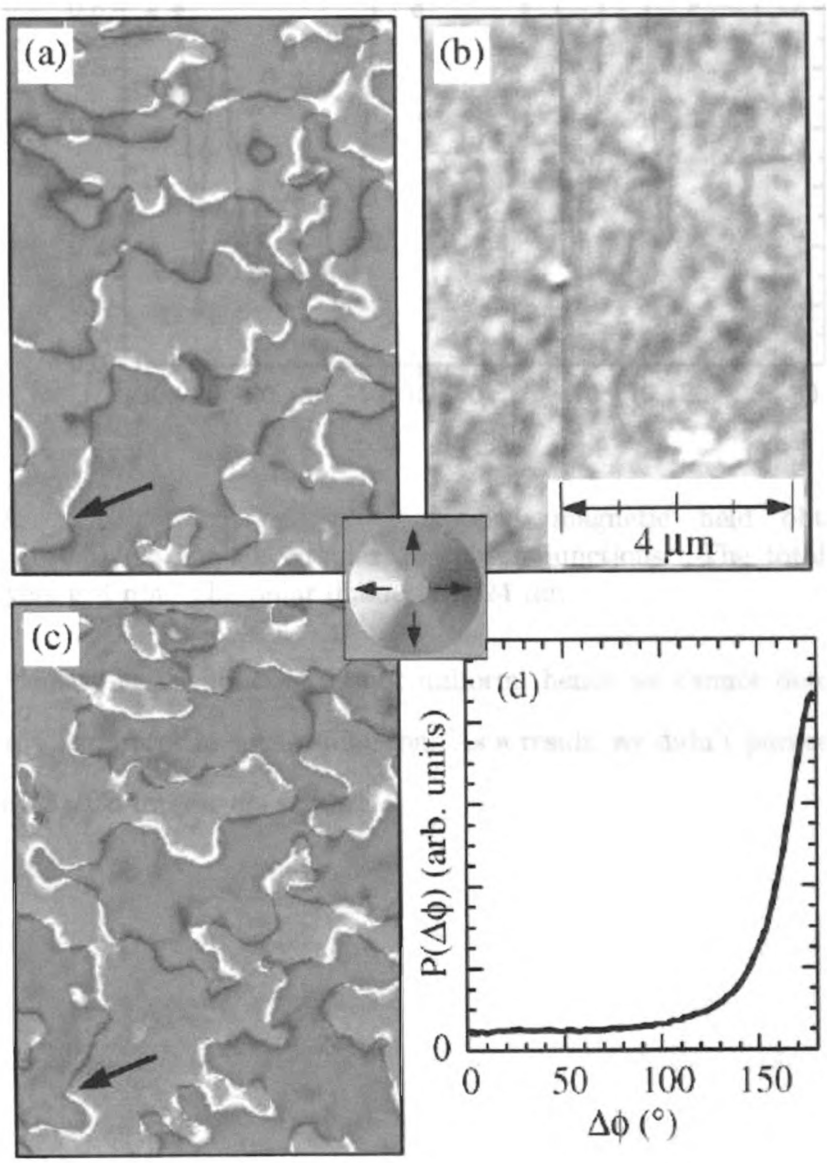

Figure 6.17: SEMPA images samples studied by Unguris *et al.* [83].

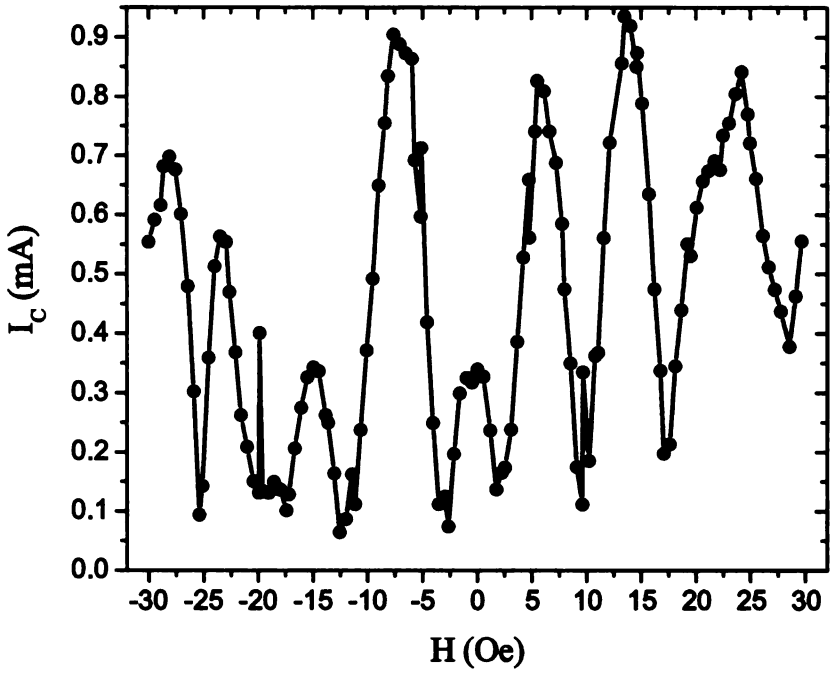

Figure 6.18: Critical current vs. applied magnetic field obtained for Nb/Cu/Co/Cu(0.8)/Co/Cu/Nb circular Josephson junctions. The total thickness of the Co layers is 4 nm. The pillar diameter is 24 μm.

the current density in the junction is not uniform; hence we cannot determine the maximum critical current in such a junction. As a result, we didn't pursue junctions with Co/Cu(0.8)/Co interlayers further.

Chapter 7

Long Range Triplet Component LRTC

The main thrust for this project was the search for the Long Range Spin Triplet Correlations -LRTC- in SFS Josephson junctions, in which the two spins align parallel to each other.These correlations can penetrate deep into the ferromagnet, and decay on the same length scale as that of spin singlet in a normal metal. They are predicted to appear in SF systems in the presence of certain magnetic inhomogeneities at the superconductor ferromagnet interface. In chapter 6, we presented our early data on SFS Josephson junctions containing a single Co layer as the ferromagnet, and S[SAF]S Josephson junctions, with SAF being Co/Ru(0.6)/Co. In both systems no sign of the triplet correlations was observed. In this chapter, we discuss new systems that may produce these elusive spin correlations. In section 7.1, we present data for SF$'$[SAF]F$'S$ with F$'$ being the weak ferromagnetic alloy $Cu_{0.48}Ni_{0.52}$. Also data with F$'$ being either Co platelets or CuPt are presented. In section 7.2 we discuss the sources of magnetic inhomogeneity in our samples, followed by theoretical treatment in section 7.3.

7.1 Josephson junctions of the form SF′[SAF]F′S

In the hunt for the spin triplet correlations in ferromagnetic Josephson junctions, we in Birge's group used two approaches; one approach carried out by Trupti Khaire was to use a weak ferromagnetic alloy, e.g PdNi [85], and the other approach was carried out by me, where I used the strong ferromagnet Co, with the Co layer being split into two layers separated by a thin non-magnetic metal-SAF- [64].In both approaches the thickness of the ferromagnetic barrier was systematically increased from thin to thick. For thin layers of the ferromagnetic layer, the short-range spin singlet component of the supercurrent is dominant until a critical thickness is reached where the long-range spin triplet component of the supercurrent should take over and dominate. Unfortunately both approaches didn't show any sign of the triplet correlations, probably due to the short spin diffusion length in PdNi- about 2.8 nm- [86], and due to the insufficient amount of magnetic inhomogeneity in the SAF system [83].

Now to collect all the pieces and finish the puzzle, one can think of the process of detection of spin triplet correlations in SFS Josephson junctions as two processes. First, spin triplet correlations need to be generated at the SF interfaces. Second, the generated spin triplet correlations are subsequently propagated through the F-layer. This can be achieved by fabricating samples of the form SF′[SAF]F′S with F′ being ferromagnetic material with magnetic inhomogeneity chosen to optimize the generation of spin triplet correlations at the SF′ interfaces, like PdNi [85] or CuNi [33], and where SAF is a synthetic antiferromagnet with little spin memory loss (large spin diffusion length) [64]. A non-magnetic layer (Cu in this case) is inserted between the F′ and Co layers in order to isolate the F′ and Co layers magnetically, so that the magnetization of the F′ is not exchange coupled to that of the Co layers. Also we showed in chapter 6 that the addition of the thin Cu buffer layers changes the growth characteristics of the Co layers and re-

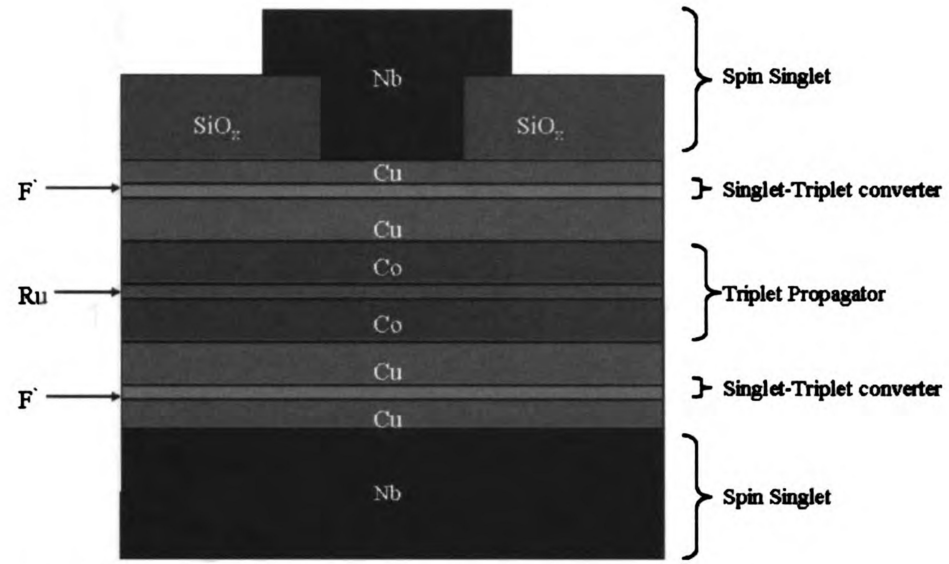

Figure 7.1: Schematic diagram of SNF′N[SAF]NF′NS Josephson junction cross section.

sulted in larger I_C of the Josephson junctions. Our new Josephson junctions then have the structure SNF′N[SAF]NF′NS as shown in Figure 7.1. For the F′ layer we used the weak ferromagnetic alloy $Cu_{0.48}Ni_{52}$ with Curie temperature T_{Curie} = 50 K. And for SAF, we used Co/Ro(0.6)/Co. The structure of the new junctions is Nb(150)/Cu(5)/F′/Cu(10)/SAF/Cu(10)/F′/Cu(5)/Nb(25)/Au(15)/Nb(200)/Au(15). To see if the added F′ layers can enhance the supercurrent of our Josephson junctions, we chose one thickness for the Co layer(total D_{Co} = 20 nm), and varied the thickness of the F′ layers. We chose a very thick Co, because from our previous findings [64], we found that the singlet supercurrent is suppressed by over 4 orders of magnitude when changing the total Co thickness from 2 to 23 nm, so any enhancement in the critical current at this thickness can be seen as a strong evidence for its spin-triplet nature. Figure 7.2 shows the d_{CuNi} thickness dependence of the critical current I_c times the normal state resistance R_N with the D_{Co} fixed at 20 nm. As is clear from the figure, for Josephson junctions without the CuNi layers, the product I_cR_N is

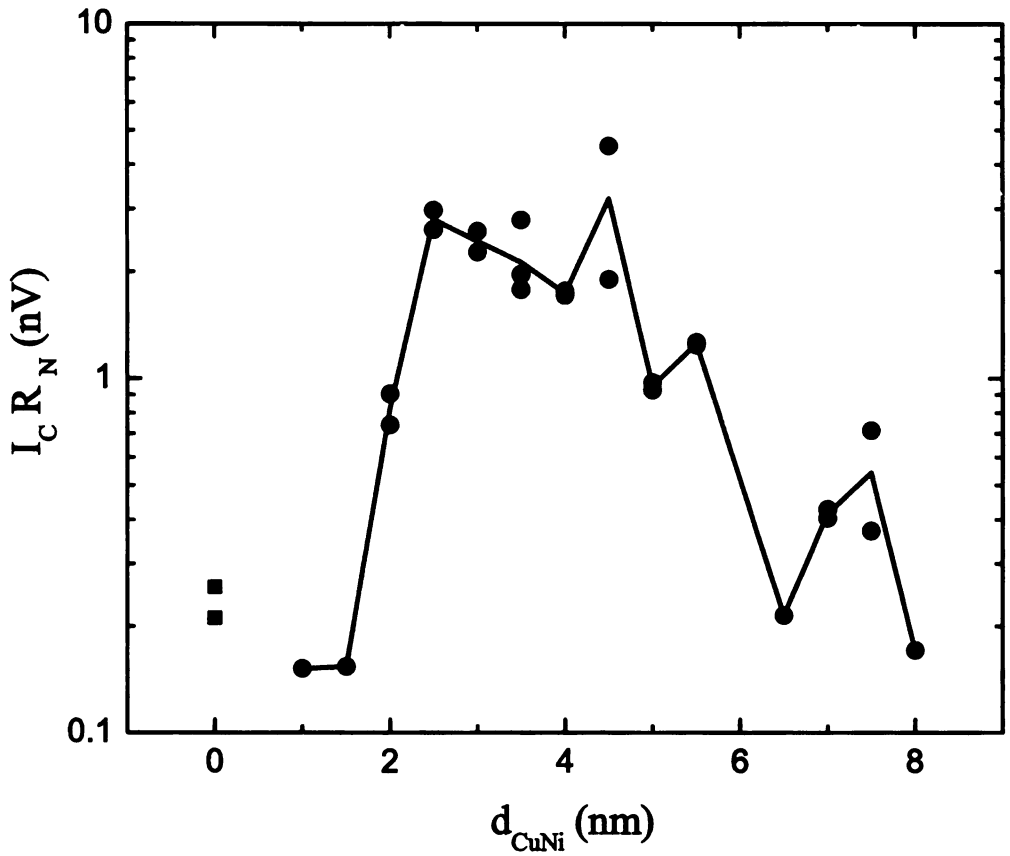

Figure 7.2: I_c R_N product as a function of d_{CuNi} for a series of Josephson junctions with fixed D_{Co} = 20 nm. Line drawn through average of data points. (The two squares at d_{CuNi} = 0 are taken from Ref. [64].)

very small, but starts increasing gradually with adding the CuNi layers, reaching a maximum value for $d_{CuNi} = 2 - 4nm$. Further increasing the thickness of the CuNi layers decreases the I_cR_N product. We attribute the enhancement in the I_cR_N product to the spin-triplet correlations being generated and propagated in our Josephson junctions. Destruction of the spin-triplet correlations due to the spin memory loss in the bulk of the CuNi layers may explain the decrease in I_cR_N at large d_{CuNi} values. The spin memory loss in CuNi is very short- about 1.4 nm [33]. It is obvious now that a thin layer of CuNi is enough to generate spin-triplet correlations, but a thick layer kills them. To observe the dependence of the critical current on Co thick-

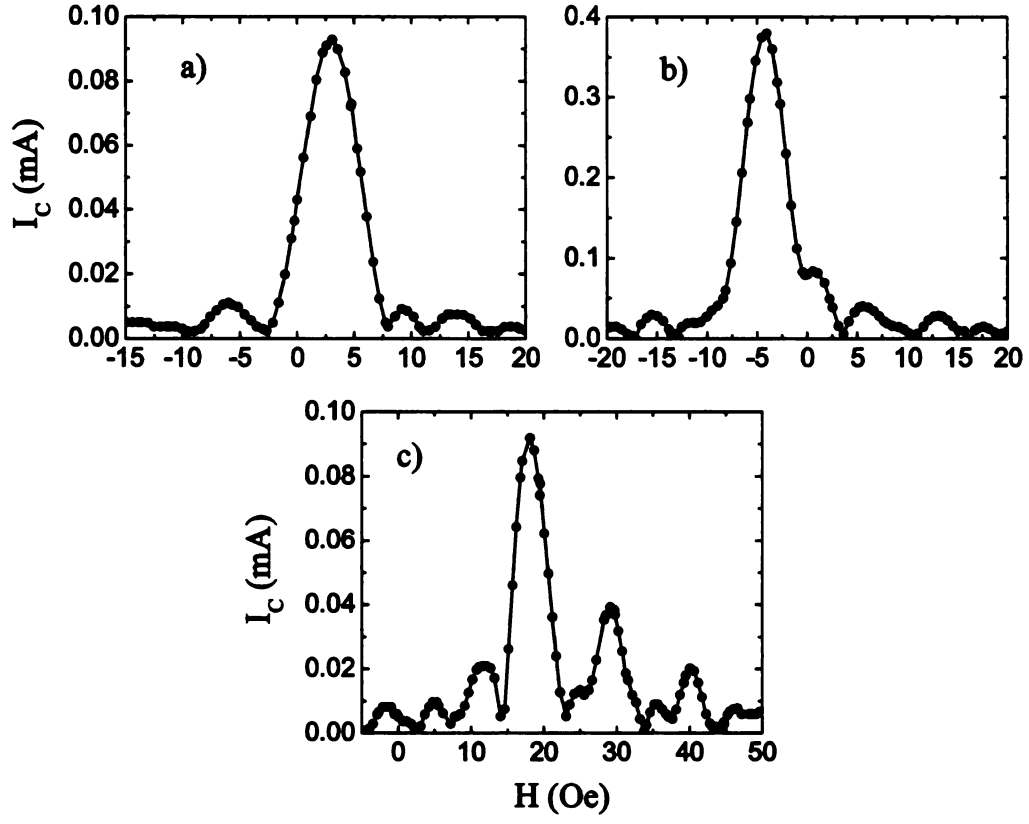

Figure 7.3: Critical current (I_c) vs. applied magnetic field (H) for a 20 μm diameter Josephson junctions with d_{CuNi} = 3 nm, measured at T = 4.2 K for different total thickness of the Co layers: a) 14 nm, b) 26 nm, c) 38 nm. (The lines are guides to the eye.)

ness, we fabricated a new set of samples of the form SNF′N[SAF]NF′NS, with fixed CuNi layer thickness, d_{CuNi} = 3 nm. Figure 7.3 shows Fraunhofer patterns for three junctions with total thickness varying from 14 to 38 nm for a 20 μm pillar diameter Josephson junctions. The first two patterns are almost ideal Airy patterns, while the third one is very good. The central maximum is shifted from H = 0 by about 18 Oe; this could be a result of the large thickness of the two Co layers on either side of the Ru spacer, in which the coupling is not as strong as in thinner samples, so some flux has been trapped in the junction that leads to this shift. Even with this shift, we still have a very clear central peak that gives us a reliable measurement of the maximum critical current. Figure 7.4 shows the product of critical current and normal state resistance, I_cR_N, vs. total cobalt thickness, $D_{Co} \equiv 2d_{Co}$, for a series of junctions with fixed CuNi layer thickness, d_{CuNi} = 3 nm. This is the main result of the whole thesis. There are two distinct data sets. The first data set represented by circles is for Josephson junctions containing a thin layer of CuNi, d_{CuNi} = 3 nm on both sides of the junctions. The second data set represented by triangles is for Josephson junctions without the CuNi layers [64], which were discussed in chapter 6. While I_cR_N for junctions not containing the CuNi layers decays very fast over the entire Co thickness range D_{Co}, with a decay constant of 2.34 ± 0.08 nm [64], there is hardly any decay in the data for samples containing CuNi for $D_{Co} > 11$ nm. This long-range behavior of Josephson coupling is a trade mark signature of spin-triplet correlations being generated and propagated through these Josephson junctions.

7.2 Possible sources for Magnetic inhomogeneity in our Josephson junctions

Now that the spin triplet supercurrent has been observed in our Josephson junctions, the immediate question one can ask is about the source(s) of magnetic inhomogeneity

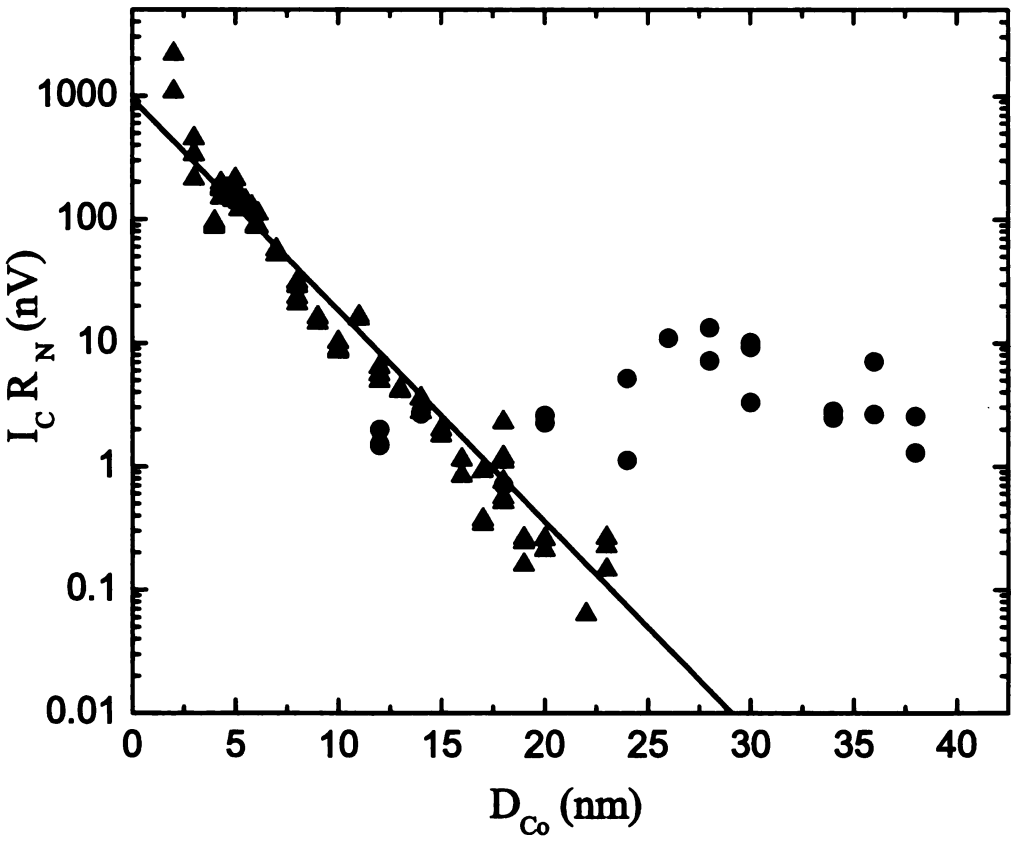

Figure 7.4: I_cR_N product as a function of total Co thickness,$D_{Co} = 2d_{Co}$. Circles represent junctions with CuNi and $d_{CuNi} = 3$ nm, whereas triangles represent junctions with no CuNi layers (taken from Ref. [64]).

in these Josephson junctions. We can think of two scenarios for the origin of magnetic inhomogeneity in our Josephson junctions that showed the long range triplet behavior.

1. Since samples without the F′ layers didn't show any sign of spin triplet correlations, then it is logical to say that the added F′ layers are the source for spin triplet generation. In this scenario F′ layers have an intrinsic magnetic inhomogeneity in the form of multiple domains with non-collinear magnetization so all that the Cooper pairs need is just to penetrate the F′ layers before they encounter non-collinear magnetization between adjacent domains (near a domain wall) so spin singlet-triplet conversion may occur. This is shown schematically in Figure 7.5. Domain size combined with out-of-plane magnetocrystalline anisotropy in F′ layers are likely to be the deciding factors in this scenario. Competition between out-of-plane magnetocrystalline anisotropy and the in-plane shape anisotropy of thin films can lead to stripe domains with canted magnetization [87] and thus enhances non-collinear magnetization in neighboring domains. CuNi had been shown to have out-of-plane magnetocrystalline anisotropy [88]. Recently, the domain size in $Cu_{0.47}Ni_{53}$ has been measured to be about 100 nm [89].

2. F′ layers magnetizations are non-collinear with the nearest Co-layer magnetization. In this scenario, the Cooper pairs need to penetrate both F′ and the nearest Co layer to experience non-collinear magnetization and generate the long range triplet correlations. If this is true, then probably any ferromagnetic material, either strong or weak alloy could work in place of the F′ layers, as long as the F′ layers and the Co-layer are not magnetically coupled (the F′ layer magnetization itself could even be perfectly homogeneous). This is shown schematically in Figure 7.6. Using strong ferromagnetic materials for the F′ layers may resulted in distorted Fraunhofer patterns [64], while weak ferromagnetic

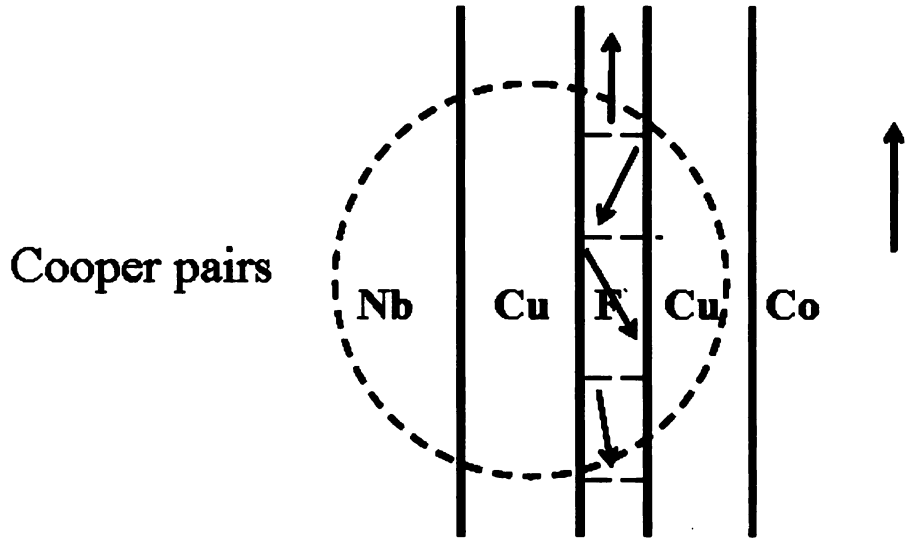

Figure 7.5: First possible source of Magnetic inhomogeneity in our Josephson junctions.

alloys, like PdNi [85] or CuNi (see Figure 7.3) produced Josephson junctions with excellent Fraunhofer patterns.

Now if we consider the length scales in our systems, then the second scenario appears to be more plausible. The domain size in CuNi alloys was measured to be around 100 nm [89], while the superconducting coherence length of the Cooper pairs in our sputtered Nb films ξ_S is 15 nm. From these numbers, it is obvious that a small number of the Cooper pairs is likely to experience non-collinear magnetization at the F$'$ layer domain walls before entering the nearest Co-layer. In the second scenario, all that the Cooper pairs need is to penetrate the 10 nm of Cu that separate the F$'$ layer and the nearest Co-layer to experience non-collinear magnetization. The Cooper pair decay length in nonmagnetic materials (Cu in our case) is very long: using our measured Cu resistivity of 5 nΩm and the Einstein relation gives $\xi_N = 116$nm for Cu at $T = 4.2$K. To verify this conclusion in the group, a visiting student Caroline Klose [92] used the strong ferromagnet elemental Ni as the F$'$ layer. Thin Ni films have an

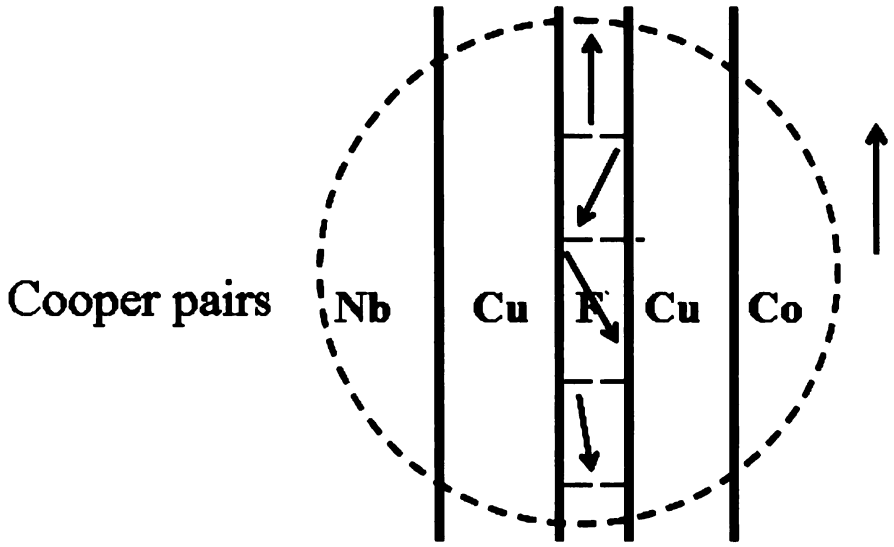

Figure 7.6: Second possible source of Magnetic inhomogeneity in our Josephson junctions.

in-plane shape anisotropy, and the domain size is much larger than that of CuNi, so neighboring domains in the Ni layer are not likely to support enough non-collinear magnetization at the right length scale to convert spin-singlet pairs into spin-triplet pairs, so any enhancement of the critical current should be attributed to the non-collinearity of magnetization between the Ni and the nearest Co-layer. A very thin layer of Ni (d_{Ni} = 1.5nm) increases I_cR_N by a factor of 300 relative to samples with no F' layer as shown in Figure 7.7. This enhancement in I_cR_N strongly supports the conclusion that the second scenario is the origin of non-collinear magnetization in these Josephson junctions. Another candidate we tried for the X-layer was Co-platelets, which are ultra thin layers of Co embedded in a Cu matrix. The resulting Co platelets are ferromagnetic at low temperature with random magnetization directions (needed to generate the triplet) as shown in Figure 7.8. Sample structure is as follows: Nb/Cu/$[Co(x)/Cu]_n$ /SAF/$[Cu/Co(x)]_n$ /Cu/Nb. With n = 1, 2 and x = 0.3, 0.4, and 0.5 nm. Figure 7.9 shows an example of the high quality Fraunhofer patterns

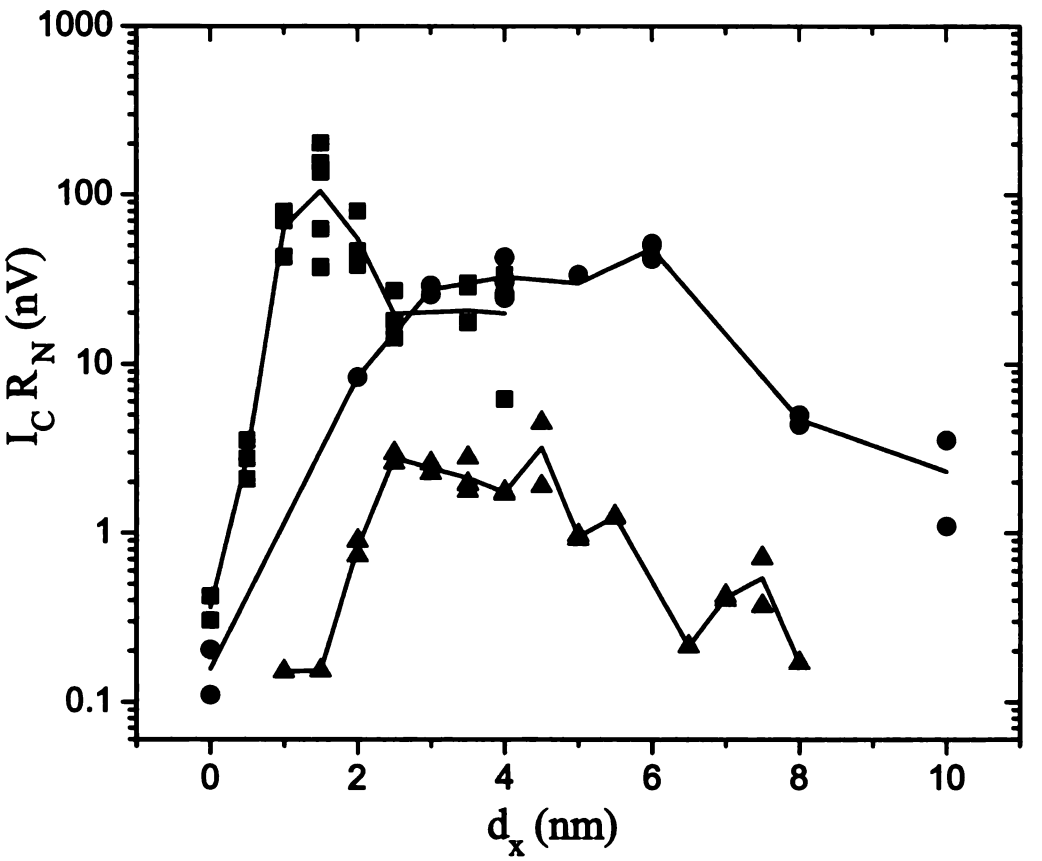

Figure 7.7: Product of critical current times normal-state resistance vs. thickness of X layer for three different sets of Josephson junctions. Black squares have X = Ni, red circles have X = PdNi, and blue triangles have X = CuNi. The solid lines are guides to the eye, and pass through the mean value of the multiple data points at each value of d_X, [92].

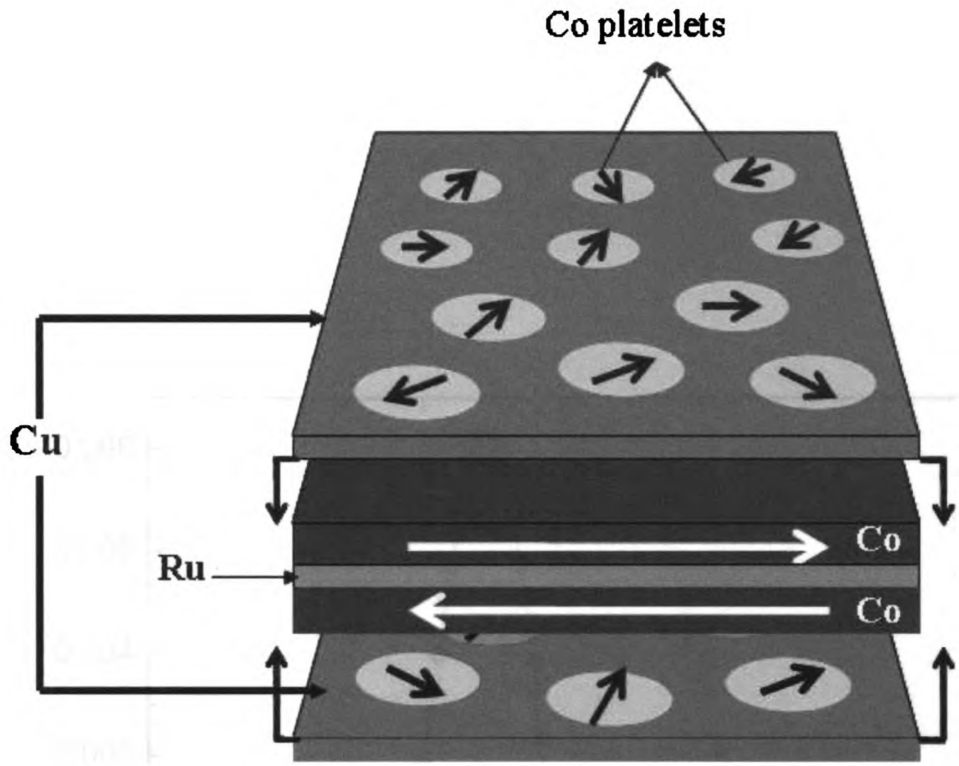

Figure 7.8: 3-D view of Co-platelets embedded in a Cu matrix.

obtained for n = 2, and x = 0.5 nm. Figure 7.10 shows the product of critical current times normal-state resistance vs. thickness of Co-platelets layer for n =1 and 2, and three thicknesses of Josephson junctions. Also included is a datum point for a junction that has no Co-Platelets (from [64]). It is clear from Figure 7.10 that we have some enhancement, but the data are scattered, and we couldn't tell what thickness of the platelets, and what repeat (n) gives the best results. It seems more experiments are needed. Aside from the presence of noncollinear magnetization, theory suggests that any spin-active interface between a superconductor and a ferromagnet can produce spin-triplet correlations [43]. We have tried using X = $Cu_{0.94}Pt_{0.06}$, an alloy with strong spin-orbit scattering. We picked a certain D_{Co} = 16 nm and measured the critical current for different d_{CuPt} as shown in Figure 7.11. It seems

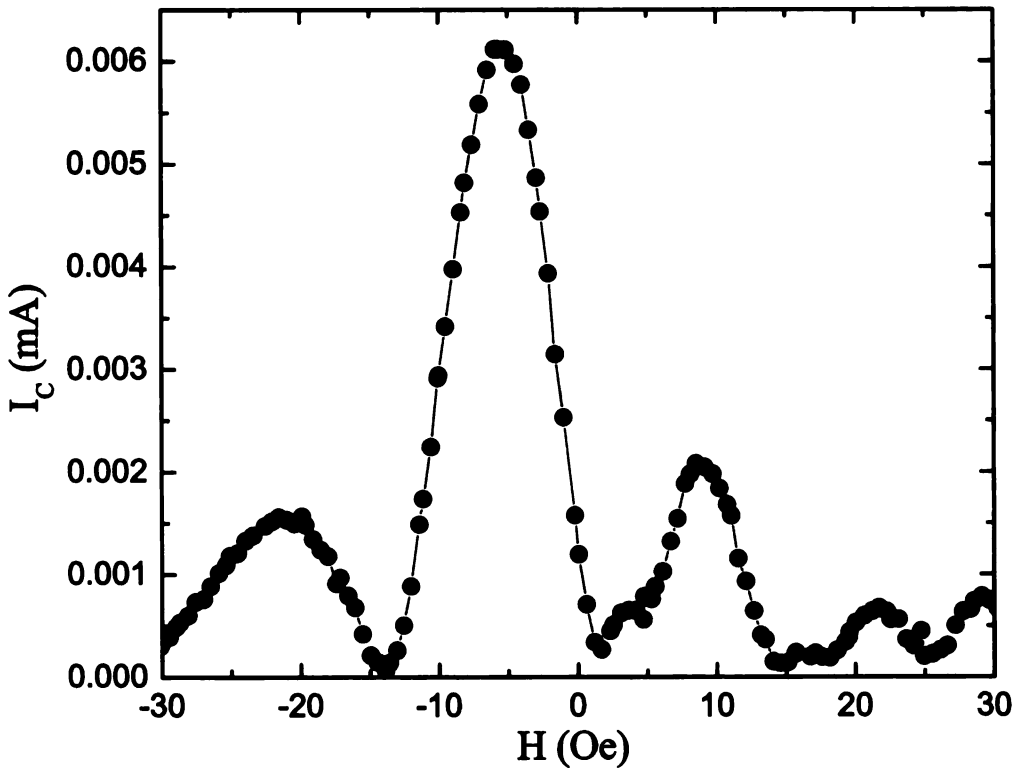

Figure 7.9: Fraunhoffer diffraction pattern for n = 2, and x = 0.5 nm.

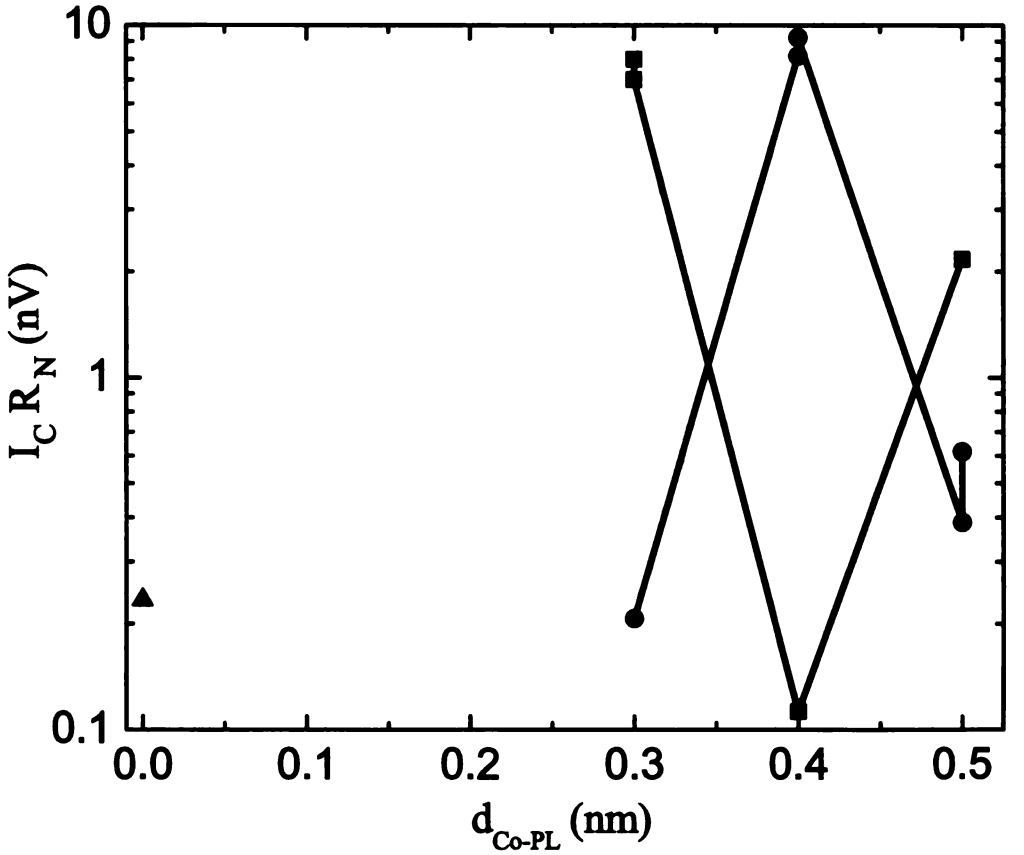

Figure 7.10: Product of critical current times normal-state resistance vs. thickness of the Co-platelets layer. Squares have n = 1, circles have n = 2, and triangles have no Co-platelets (from [64]).

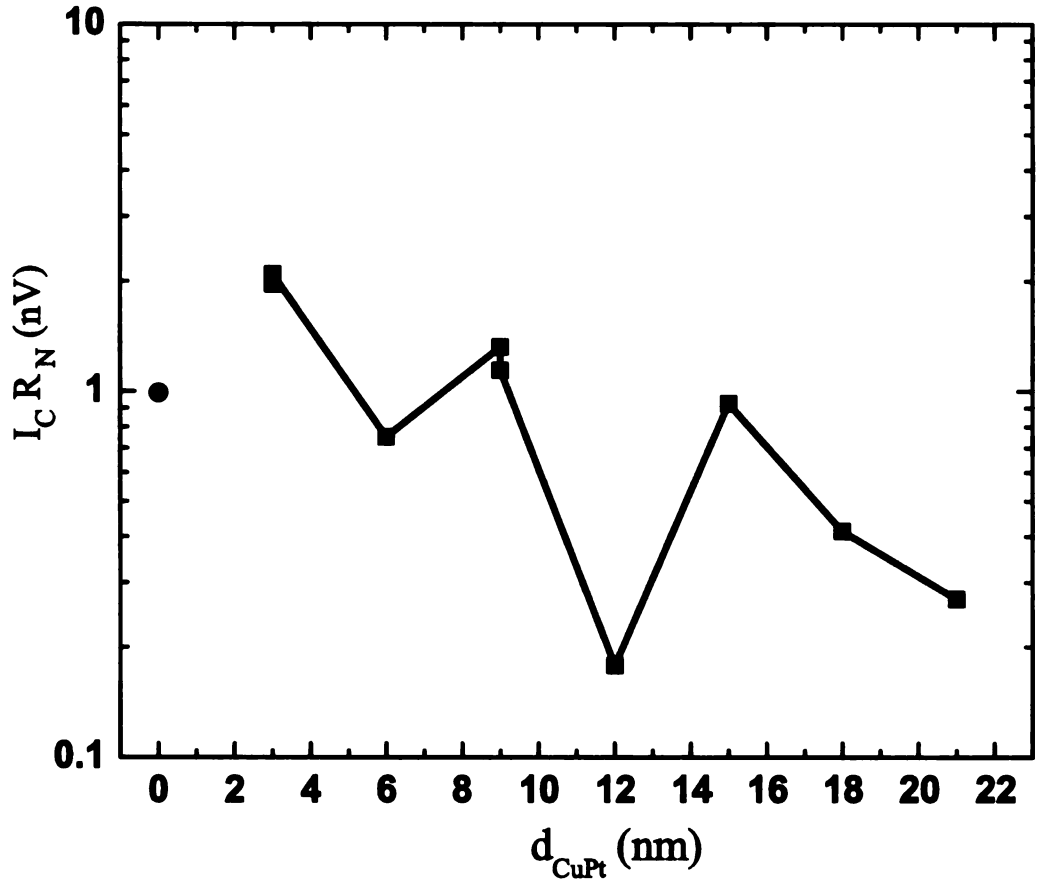

Figure 7.11: Product of critical current times normal-state resistance vs. d_{CuPt} for fixed D_{Co} = 16 nm. Squares for samples have CuPt, and the circle datum point has only Cu (from [64]) for comparison.

that at d_{CuPt} = 3 nm there is enhancement in the critical current compared to samples without the CuPt. So we decided to make more samples with different Co thicknesses, but fixed d_{CuPt} = 3 nm. Our data show very little, if any, signature of the triplet as shown in Figure 7.12 which shows the product of critical current times normal-state resistance vs. total thickness of the Co-layer.

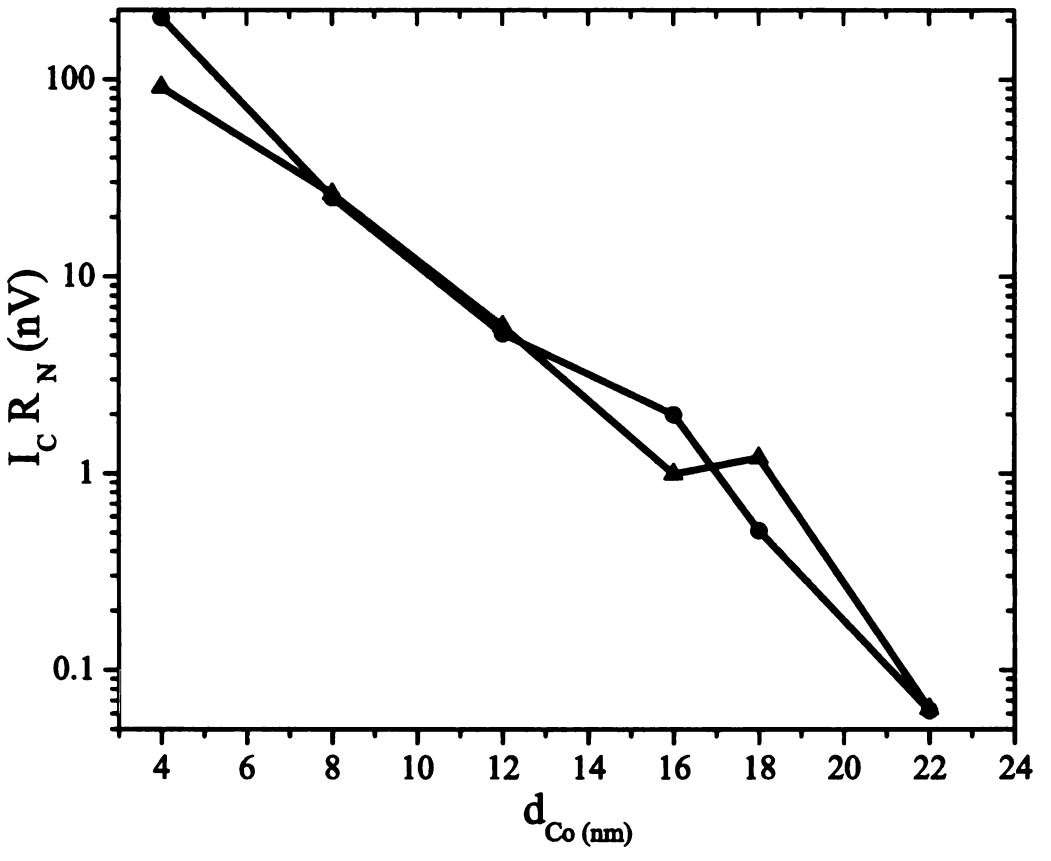

Figure 7.12: Product of critical current times normal-state resistance vs. thickness of the d_{Co} for two different sets of Josephson junctions. Circles have CuPt (d_{CuPt} = 3 nm), and triangles have only Cu (from [64]).

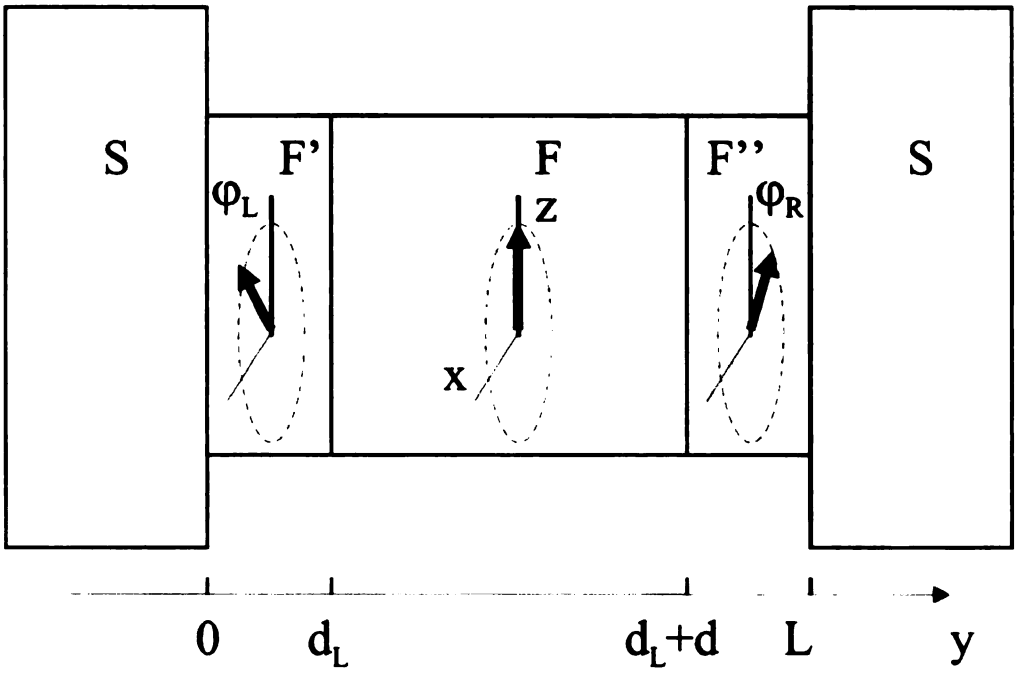

Figure 7.13: Geometry of SF′FF″S Josephson junctions studied by [90].

7.3 Theory of SNF′N[SAF]NF′NS Josephson junctions.

Josephson junctions of the form SF′FF″S have been theoretically studied by Houzet and Buzdin [90] as shown in Figure 7.13.

The role that both F′ and F″ layers play in inducing the long range triplet current in the Houzet-Buzdin structure is shown in Figure 7.14. The critical current is negligibly small for very thin F′ and F″ layers, but starts increasing gradually with increasing thickness of the F′ and F″ layers, reaching a maximum value over a small interval of the F′ and F″ layers thickness: (0.5 - 2.5) ξ_F. Further increasing the thickness of the F′ and F″ layers decreases the critical current. This is consistent with our results (see Figure 7.2), so our SNF′N[SAF]NF′NS Josephson junctions can be viewed as a realization of the Houzet-Buzdin structure, with our Josephson junctions

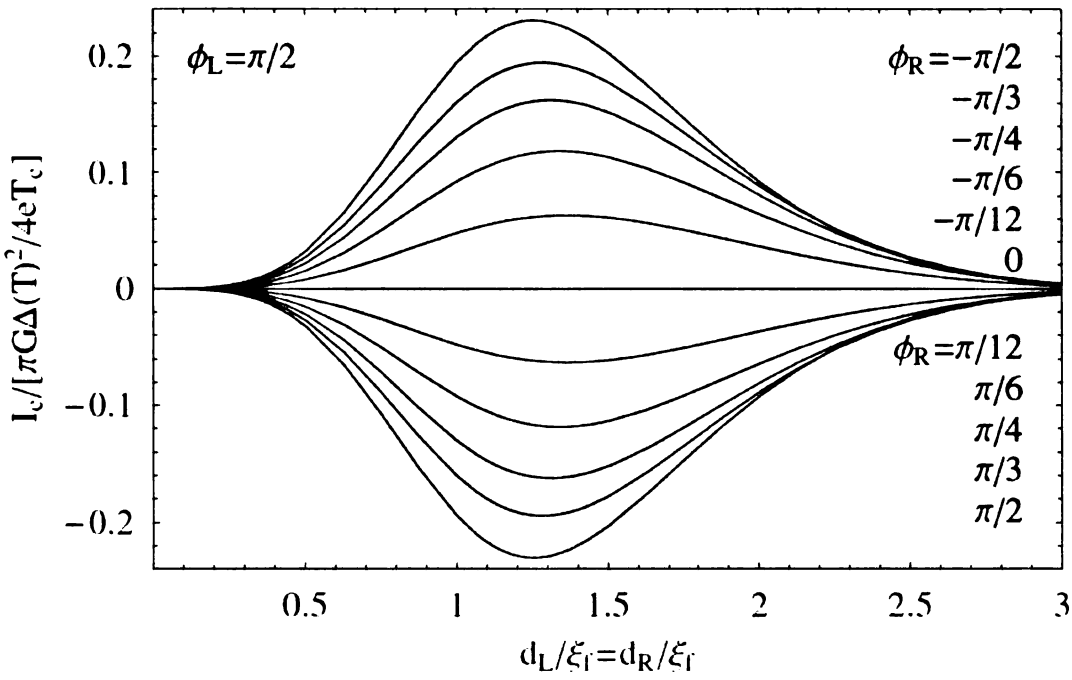

Figure 7.14: Critical current induced by long range triplet proximity effect in SF′FF″S Josephson junctions studied by [90].

having two extra elements. First, a non-magnetic layer (Cu in this case) is inserted between the F′ and Co layers in order to isolate the F′ and Co layers magnetically, and second the middle F-layer is a SAF layer with the two F-layers coupled antiparallel to each other.

There have been a large number of theoretical papers on Josephson junctions with ferromagnetic barriers. All of these papers have treated the ferromagnetic layers as if they have ideal magnetic structures, which is not the case of real life experiments, in which the magnitude of the measured long-range spin-triplet supercurrent is strongly dependent on the detailed structure of the ferromagnetic layers. This makes it difficult to compare our data quantitatively with the experiment. Domain structure depends very much on the nature of the ferromagnet; strong ferromagnets consist of well-defined magnetic domains [83], whereas weakly ferroamgnetic alloys have magnetizations that may fluctuate on short length scales without forming domains [91].

Recently the domain size of $Cu_{0.47}Ni_{0.53}$ has been measured to be about 100 nm [89]. A more realistic and helpful approach to compare data and theory is that of the decay lengths of the spin-singlet and spin-triplet components of the supercurrent. In the dirty limit, where the mean free path, l_e is the shortest length scale, the spin-singlet component of the supercurrent decays on the length scale $\xi_F = \sqrt{\frac{\hbar D_F}{E_{ex}}}$, where D_F is the electron diffusion constant, and E_{ex} is exchange energy of the ferromagnetic material. Whereas the spin-triplet component of the supercurrent decays over a much longer length scale given by the smaller of the normal metal coherence length, $\xi_N = \sqrt{\frac{\hbar D}{2\pi k_B T}}$, or the spin diffusion length, $l_{SF} = \sqrt{D_F \tau_{SF}}$, where τ_{SF} is the mean time between spin orbit or spin flip scattering events. Josephson's junctions containing Co, however, are in the intermediate limit, where l_e is larger than ξ_F but shorter than ξ_S, the superconducting coherence length, and the spin-singlet supercurrent decays over l_e. In samples without the CuNi layers, the spin-singlet critical current decays over the length scale 2.4 $\pm$ 0.08 nm [64] which is in agreement with previous measurements [34]. However the addition of the CuNi layer next to the Nb, resulted in a large enhancement of the critical current (see Figure 7.4) which is a very strong evidence for its triplet nature. One important thing to notice, however, is that the new data have a large sample to sample fluctuation, and they didn't show any discernible decay over the studied range of Co thicknesses. So we were not able to measure the spin-triplet supercurrent decay length for our junctions.

After we published our paper [93], Volkov and Efetov have analyzed our sample geometry [94]. This paper assumes a sample geometry of the form S/F/F/F/S, but with the central F-layer split into two domains with parallel or antiparallel orientations of magnetization. They also assume different exchange energies for central and outer F-layers. In addition, the central F-layer is considered to be magnetically homogeneous, whereas the outer F-layers are assumed to be magnetically inhomogeneous. The qualitative dependence of the triplet current on the outer F-layer thickness is

similar to that of [90], which supports our findings.

Before I conclude this chapter, it is important to say that the spin-triplet pair correlations observed in this study and discussed in [36] are quite different from those believed to occur naturally in materials such as Sr2RuO4 [98]. The Cooper pairs responsible for the LRTC effect presented in this thesis are believed [39, 40] to be a result of unusual s-wave triplet pairing mechanism that is odd under time reversal, or odd in frequency. Nevertheless, the observation of enhanced supercurrent in itself does not provide a conclusive evidence of this unusual symmetry of the pair correlations. More experiments need to be done to affirm the symmetry of the observed long-range pair correlations.

Chapter 8

Conclusions and future look

8.1 Overview

The long term objective of the experiments carried out in the framework of this thesis was to study Long Range Triplet Correlations 'LRTC' in Co-based Josephson junctions. This type of spin triplet pairing has been predicted by Bergeret et al. [36] given that some sort of magnetic inhomogeneity is present at the SF interface. In the case of homogenous magnetization, only spin-singlet and short-range triplet correlations are present. In the dirty limit, the critical current as a function of the ferromagnetic layer oscillates and decays over the length scale $\xi_F^{Singlet} = \sqrt{\frac{\hbar D}{E_{ex}}}$. As a result of large exchange energies, $\xi_F^{Singlet}$ is only of the order a few nm. If the system has some sort of magnetic inhomogenieties, LRTC can be induced, and penetrate much deeper in the ferromagnetic layer over the length scale $\xi_F^{Triplet}$, which is of the order of the normal metal coherence length, ξ_N. In the dirty limit it is given by $\xi_F^{Triplet} = \sqrt{\frac{\hbar D}{2\pi KT}}$.

8.2 Summary of Results

8.2.1 Early data: no LRTC!!

Successful observation of the LRTC required us to have a reliable fabrication process. This is why I spent the first couple of months trying to optimize the parameters of the image reversal process. Once I mastered the fabrication process, I started making and measuring my samples. The first set of samples had a single Co layer sandwiched between two Nb electrodes. The results were frustrating because the Fraunhofer diffraction patterns were so distorted. That is because Co like any other ferromagnetic material is divided into domains with each domain having its own magnetization, and the overall magnetization from the domains distorted the Fraunhofer pattern. To overcome this problem, we should find some way to eliminate the flux trapped in the junction. To do that, we split the single Co-layer into two layers separated by a thin nonmagnetic spacer to form what is called Synthetic Antiferromagnet 'SAF'. For the SAF, we have chosen Co/Ru/Co, with a Ru thickness of 0.6 nm. At this thickness, the Ru couples the two Co layers antiferromagnetically, in which every domain in one Co layer has a corresponding domain in the other Co layer with its magnetization coupled antiparallel. As a result, the total intrinsic magnetic flux in the junction is almost exactly zero, and the junctions exhibit nearly ideal Fraunhofer patterns as a function of applied field. Although getting ideal or close to ideal Fraunhofer patterns was very exciting, the overall data showed only a rapid decay of the I_c with d_{Co} with no sign of the LRTC. We thought of many reasons for this. One of them, there could be a large spin memory loss at the Co/Ru interface (later GMR measurements proved otherwise). Another reason could be lack of magnetic inhomogeneities at the SF interface (or at least not enough magnetic inhomogenieties). Another member of our group, Trupti Khaire, was working on a similar project, with the weak ferromagnetic alloy, PdNi, but her data showed no sign of LRTC as well, possibly because PdNi has

a very short spin memory length.

8.2.2 Good news: LRTC is there

At this point, we thought of dividing the process of observation of the LRTC into two parts: generation and propagation. For the generation of the triplet at the SF interface, we placed a thin ferromagnetic X layer next to the Nb electrode. For the propagation, we used the SAF configuration consisting of Co/Ru/Co which has large spin diffusion length. Our sample stacking is: Nb/Cu/X/Cu/Co/Ru/Co/Cu/X/Cu/Nb. A thin layer of CuNi in place of the X-layers showed a large enhancement in the critical current compared to samples without the X-layers. That was a very strong evidence of the triplet nature of the new data. Similar results were obtained by Trupti using PdNi. An important question was regarding the origin of noncollinear magnetization responsible for the generation of the LRTC. Since samples with no X layers show no sign of spin-triplet current, we thought of the X-layers as the triplet generators. In this scenario, neighboring domains in the X layer have noncollinear magnetization and Cooper pairs entering the X layer near a domain wall will go singlet to triplet conversion. Another source of the noncollinearity could be between the X-layer and the Co-layer next to it, the magnetization of the X-layer itself could be homogeneous. Length scale considerations favor the second scenario. The coherence length of our sputtered Nb is $\xi_S = 15$ nm, while the spin-singlet decay length in PdNi is of order $\xi_F = 8$ nm [85]. Domain size of CuNi was measured to be about 100 nm [89] quite a bit longer than ξ_S for Nb or ξ_F for PdNi. Hence only a small fraction of the Cooper pairs entering the F-layer are likely to experience noncollinear magnetization at X-layer domain walls. In the second scenario, all that the Cooper pairs need to do is cross the 10 nm of Cu separating the X-layer from the nearest Co layer to experience noncollinear magnetization. So to support this conclusion experimentally, a visiting undergraduate student, Caroline Klose, fabricated and measured samples with Ni as

the X-layer. The domain size of Ni is larger than that of PdNi or CuNi, and M vs. H measurements showed that it has in plane magnetization. A very thin layer of Ni was used to generate the triplet. The enhancement in the critical current was even larger than that of PdNi. This picture is fully consistent with the second scenario. Shortly after we published our paper [93], several other papers were published. Robinson *et al.* [95]) studied SFS Josephson junctions similar to ours, but with Ho as the F' layer, and observed similar behavior. Anwar *et al.* [96] reported a new study of S/F/S junctions with CrO_2, following up on the earlier work of Klapwijk's group [49]. Their experiments confirm the observation of triplet correlations in CrO_2 based Josephson junctions. However, the authors of this paper also indicate a low success of their junctions, attributing it to the complicated nature of CrO_2 that is sensitive to the growth conditions. Wang *et al.* [69] reported an observation of proximity induced superconductivity in single-crystal Co nanowires as long as 600 nm. Those authors did not intentionally introduce non-collinear magnetization into their samples, but suggested that it appeared accidentally as a result of the process of fabricating electrical contacts to the Co nanowires. A similar evidence for triplet superconductivity in Josephson junctions with ferromagnetic Cu_2MnAl-Heusler barriers was also reported recently by [97].

8.3 Future work

Currently we have two members in the group working on the triplet project. Recall in the work I presented here, we used the vertical geometry to make our samples which required us to use the synthetic antiferromagnet configuration in order to reduce the flux trapped in the junction. Instead, William Martinez is working on making the triplet samples using a lateral geometry, where he will use a thin narrow Co wire in order to reduce flux. One can therefore expect to see an ideal Fraunhofer pattern

for this type of sample even for longer Co lengths. Kurt Boden, another member of the group is working on measuring the density of states (DOS) of the samples with triplet correlations, using tunneling spectroscopy.

BIBLIOGRAPHY

[1] Michael Tinkham, *Introduction to superconductivity*, McGraw-Hill (1995).

[2] D.R. Tilley and J.Tilley, *Superfluidity and superconductivity*, 3rd ed. Bristol, (1996).

[3] D. Jiles, *Introduction to Magnetism and Magnetic Materials*, 2nd. Chapman and Hall, London, (1998).

[4] R. O'Handley, *Modern magnetic materials: principles and applications*, Wiley, (2000).

[5] H. Kamerlingh-Onnes, Comm. Phys. Lab. Univ. Leiden, **122** and **124**, (1911).

[6] G. Bednorz and K.A. Müller, Z. Phys. B **64**, 189 (1986).

[7] W. Meissner and R. Ochsenfeld, Naturwissenschaften **21**, 787 (1933).

[8] C. Garter and H. Casimir, Phys. Z. **35**, 963 (1934); Z. Techn. Phys. **15**, 539 (1934).

[9] H. London and F. London, Proc. Roy. Sos. (London) A**149**, 71 (1935), Physica **2**, 341 (1935).

[10] J. Bardeen, L. Cooper, and J. Schrieffer, Phys. Rev. **108**, 1175 (1957).

[11] N. Ashcroft and N. Mermin *Solid State Physics*, (Brooks/Cole, Cengage Learning, Belmont, CA, USA, 1976)

[12] A. Abrikosov, Zh. Eksp. Teor. Fiz. **32**, 1442 (1957).

[13] A. Abrikosov, Sov. Phys. JETP **5**, 1174 (1957).

[14] A. Abrikosov, *Fundamentals of the Theory of Metals*, (North Holland, Amsterdam, 1988).

[15] R. Soohoo, *Magnetic Thin Films*, (1st ed. Harper and Row, New York, 1965).

[16] P. Weiss, J. Phys. **6**, 661 (1907).

[17] C. Kittel, Rev. Mod. Phys. **21**, 541 (1949).

[18] www.ndt-ed.org

[19] B. Josephson, Phys. Lett. **1**, 251 (1962).

[20] B. Josephson, Rev. Mod. Phys. **46**, 251 (1974).

[21] P. Anderson, Phys. Rev. Lett. **10**, 230 (1963).

[22] R. Feynman, *The Feynmans Lectures on Physics-Volume III*, (Addison-Wesley, 1965).

[23] J. Clarke and alex I. Braginski, *SQUID Handbook: Fundamentals and Technology of SQUIDs and SQUID Systems (Vol. 1)* (Wiley-VCH Verlag GmbH and Co. KGaA, Weinheim, Germany, 2004).

[24] A. Barone and G. Paterno, *Physics and Applications of the Josephson Effect*, (John Wiley and Sons, Inc. 1982).

[25] L. P. Lévy, *Magnetism and Superconductivity*, (Springer-Verlag, Berlin 2000).

[26] J. Rowell, Phys. Lett. **11**, 200 (1963).

[27] E.A. Demler, G.B. Arnold, and M.R. Beasley, Phys. Rev. B **55**, 15174 (1997).

[28] P.G. de Gennes, Rev. Mod. Phys. **36**, 225 (1964).

[29] I. Kulik, JETP Lett. **2** 84 (1965).

[30] L. Bulaevskii, V. Kuzii, and A. Sobyanin, JETP Lett. **25**, 290 (1977).

[31] A. Buzdin , JETP Lett. **35**, 178 (1982).

[32] V. Ryazanov, V. Oboznov, A. Rusanov, A. Veretennikov, A. Golubov, and J. Aarts, Phys. Rev. Lett. **86**, 2427 (2001).

[33] V. Oboznov, V. Bol'ginov, A. Feofanov, V. Ryazanov, and A. Buzdin, Phys. Rev. Lett. **96**, 197003 (2006).

[34] J. Robinson, S. Piano, G. Burnell, C. Bell and M. Blamire, Phys. Rev. Lett. **97**, 177003 (2006).

[35] V. Berezinskii, JETP Lett. **20** 287, 1974.

[36] F.S. Bergeret, A.F. Volkov, and K.B. Efetov, Phys. Rev. Lett. **86**, 4096 (2001).

[37] A.F. Volkov, F.S. Bergeret, and K.B. Efetov, Phys. Rev. Lett. **90**, 117006 (2003).

[38] F.S. Bergeret, A.F. Volkov, and K.B. Efetov, Phys. Rev. B **68**(6) 064513 (2003).

[39] A. Kadigrobov, R.I. Shekhter, and M. Jonson, Europhys. Lett. **54**(3), 394 (2001).

[40] F.S. Bergeret, A.F. Volkov, K.B. Efetov, Rev. Mod. Phys. **77**, 1321 (2005).

[41] T. Champel, and M. Eschrig, Phys. Rev. B **72(5)**, 054523 (2005).

[42] T. Champel, T. Lofwander, and M. Eschrig, Phys. Rev. Lett. **100**, 077003 (2008).

[43] M. Eschrig, J. Kopu, J. C. Cuevas, and G. Schon, Phys. Rev. Lett. **90**, 137003 (2003).

[44] Matthias Eschrig, Tomas Löfwander, Nature Physic **4**, 138 (2008).

[45] T. Kontos, M. Aprili, J. Lesueur, and X. Grison, Phys. Rev. Lett. **86(2)**, 304 (2001).

[46] M. Giroud, H. Courtois, K. Hasselbach, D. Mailly, and B. Pannetier, Phys. Rev. B **58**, R11872 (1998).

[47] M. Lawrence, and N. Giordano, J. Phys. : Condens. Matter **8**, 563 (1996) and J. Phys.: Condens. Matter **11**, 1089 (1999).

[48] V. Petrashov, I. Sosnin, I. Cox, A. Parsons, and C. Troadec, Phys. Rev. Lett. **83**, 3281 (1999).

[49] R.S. Keizer, S.T.B. Goennenwein, T.M. Klapwijk, G. Xiao, and A. Gupta, Nature (London) **439**, 825 (2006).

[50] I. Sosnin, H. Cho, V.T. Petrashov, and A.F. Volkov, Phys. Rev. Lett. **96**, 157002 (2006).

[51] D. Edmunds, W. Pratt, and J. Rowlands, Rev. of Sci. Instr. **51**, 1516 (1980).

[52] K. Eid, Ph.D. thesis, Michigan State University, USA, 2002.

[53] I. Moraru, Ph.D. thesis, Michigan State University, USA, 2006.

[54] A. Sharma, Ph.D. thesis, Michigan State University, USA, 2008.

[55] J. Robinson, S. Piano, G. Burnell, C. Bell, and M. G. Blamire, Phys. Rev. B **76**, 094522 (2007).

[56] C. Sürgers, T. Hoss, C. Schönenberger, C. Strunk, J. Magn. Magn. Mat., 240, 598 (2002).

[57] P. Grünberg, R. Schreiber, and Y. Pang, Phys. Rev. B **57**, 2442 (1986).

[58] M. Baibich, J. Broto, A. Fert, F. N. V. Dau, and F. Petroff, Phys. Rev. Lett. **61**, 1988 (1988).

[59] G. Binasch, P. Grünberg, F. Saurenbach, and W. Zinn, Phys. Rev. B **39**, 4828 (1989).

[60] S. Parkin, N. More, and K.P. Roche, Phys. Rev. Lett. **64**, 2304 (1990).

[61] S. Parkin, Phys. Rev. Lett. **67**, 3598 (1991).

[62] Y. Yafet, Phys. Rev. B **36**, 3948 (1987).

[63] S. Parkin, R. Bhadra and K. P. Roche, Phys. Rev. Lett. **66**, 2152 (1991).

[64] M. Khasawneh, W. Pratt, and N. Birge, Phys. Rev. B **80**, 020506(R) (2009).

[65] L. Liebermann, D. Fredkin, and H. B. Shore, Phys. Rev. Lett. **22**, 539 (1969).

[66] L. Liebermann, J. Clinton , D. Edwards and J. Mathon, Phys. Rev. Lett. **25**, 232 (1970).

[67] C. England, W. Bennet, and C. Falco, J. Appl. Phys. **84**, 5757 (1988).

[68] K. Rahmouni, S. Zoll, N. Persat, D. Stoeffler and A. Dinia, Computational Materials Science, **10**, 269, 1998.

[69] W. Wang, Y. Dai, T. Wang, J. Li, X, He and B. Liu, Appl. Phys. Lett. **94**, 131903, 2009.

[70] A. Dinia, J. Bailly, K. Ounadjela and D. Stoeffler, Sloid State Communications, **96**, 549, 1995.

[71] S. Zoll, A. Dinia, J. Meny, G. Pan, A. Michel, L. El Chahal, V. Bohnes and P. Painssod, Phys. Rev. Lett., **57**, 4824, 1998.

[72] K. Bal, H. Berg, D. Deck and T. Rasing, J. Appl. Phys., **90**, 5228, 2001.

[73] J. Robinson, Z. Barber and M. G. Blamire, Appl. Phys. Lett. **95**, 192502 (2009).

[74] Y. Obi, M. Ikebe, T. Kubo and H. Jujimori, Physica C, **317**, 149, 1999.

[75] Š. Pick, I. Turek and H. Dreyssé, Solid State Communications, **124**, 21, 2002.

[76] S. Chikazumi, *Physics of Ferromagnetism*, (Oxford University Press, England 1997).

[77] Ya. M. Blanter and F.W.J. Hekking, Phys. Rev. B **69**, 024525 (2004).

[78] Z. Pajović, M. Boović, Z. Radović, J. Cayssol and A. Buzdin, Phys. Rev. B **74**, 184509 (2006).

[79] O. Kashuba, Y.M. Blanter, V.I. Falko, Phys. Rev. B **75**, 132502 (2007).

[80] B. Crouzy, S. Tollis, and D.A. Ivanov, Phys. Rev. B **75**, 054503 (2007).

[81] F.S. Bergeret, A.F. Volkov, and K.B. Efetov, Phys. Rev. Lett. **68**, 064513 (2001).

[82] A. Buzdin, B. Bujicic and M. Kupriyanov, Sov. Phys. JETP **74**, 124 (1992).

[83] J.A. Borchers, J. Dura, J. Unguris, D. Tulchinsky, M. Kelley, C. Majkrzak, S. Hsu, R. Loloee, W.Pratt, Jr. and J. Bass Phys. Rev. Lett. **82**, 2796 (1999).

[84] K. Eid, D. Portner, J. Borchers, R. Loloee, M. Al-Haj Darwish, M. Tsoi, R. Slaterl, K. ÒDonovan, H. Kurt, W. Pratt, Jr. and J. Bass, Phys. Rev. B **65**, 054424 (2002).

[85] T. Khaire, W.P. Pratt, Jr., and N.O. Birge, Phys. Rev. B **79**, 094523 (2009).

[86] H. Arham, T. Khaire, R. Loloee, W. Pratt, Jr. and N. Birge, Phys. Rev. B **80**, 174515 (2009).

[87] T. Koikeda, K. Suzuki, and S. Chikazumi, Appl. Phys. Lett. **4**, 160 (1964).

[88] C. Bell, G. Burnell, C. W. Leung, E. J. Tarte, D.-J. Kang, and M. G. Blamire, Appl. Phys. Lett. **84** 1153 (2004).

[89] I. Veshchunov, V. Oboznov, A. Rossolenko, A.Prokofiev and L. Vinnikov, JETP Lett. **88**, 11 (2008).

[90] M. Houzet and A.I. Buzdin, Phys. Rev. B **76**, 060504(R) (2007).

[91] H. Sellier, C. Baraduc, F. Lefloch and R. Calemczuk , Phys. Rev. B **68**, 054531 (2003).

[92] M. Khasawneh, T. Khaire, C. Klose, W. Pratt, Jr. and N. Birge, to appear in Superconductor Science and Technology.

[93] T. Khaire, M. Khasawneh, W. Pratt, Jr. and N. Birge, Phys. Rev. Lett. **104**, 137002 (2010).

[94] A. Volkov and K. Efetov, Phys. Rev. B **81**, 144522 (2010).

[95] J. Robinson, J. Witt and M. Blamire, Nature Physics (6), 329 (2010).

[96] M. Anwar, F. Czeschka, M. Hesselberth, M. Porcu, and J. Aarts, Phys. Rev. B **82**, 100501 (2010).

[97] D. Sprungmann, K. Westerholt, H. Zabel, M. Weides, and H. Kohlstedt, Phys. Rev. B **82**, 060505 (2010).

[98] K. Nelson, Z. Mao, Y. Maeno and Y. Liu, Science **306** 1151 (2004).